TOWARDS NON-INVASIVE BLOOD CELL COUNTING AND ANALYSIS WITH OBLIQUE BACK-ILLUMINATION CAPILLAROSCOPY

by
Gregory N. McKay

A dissertation submitted to The Johns Hopkins University in conformity with the requirements for the degree of Doctor of Philosophy

Baltimore, Maryland
APRIL, 2022

Abstract

Blood is indispensable in human life. Proper perfusion supplies nutrients and oxygen, removes waste, facilitates immune responses, and transports vital signaling molecules to nearly every tissue of the human body. Laboratory-based analysis of blood is a critical component of modern clinical care, providing medical staff with crucial information about health and disease. Among these diagnostic and analytic tests, the complete blood count (CBC) is the most common. The CBC, like most other blood tests, is invasive. It requires phlebotomy and transportation to complex and expensive laboratory equipment for analysis. Often, when disease is suspected, a blood smear is also ordered, where blood is deposited as monolayer on a glass slide and further analyzed by a hematologist using microscopy. These two tests provide the cornerstone for the diagnosis of hematologic disorders such as anemia, leukemia, sickle cell disease, myeloproliferative disorders, and thrombocytopenia. The CBC and blood smear are precise and effective tools that have been developed over centuries, however their invasive nature and reliance on complex and expensive equipment poses problems for certain vulnerable patient populations. The immunosuppressed are at risk of nosocomial infection, neonates are at risk of iatrogenic anemia, and many patients in remote and low-resource settings do not have access to necessary laboratory equipment. Thus, a device capable of providing non-invasive blood cell counting and analysis would fill an unmet clinical need for a diverse group of patients. Such a device would need to probe blood cells flowing through capillaries and other blood vessels *in vivo*, ideally in a label-free manner for safest use in humans. The work presented in this dissertation provides the foundation for such a technology, a combined phase and absorption contrast microscopy technique called oblique

back-illumination capillaroscopy. This technique enables non-invasive, label-free imaging of individual blood cells flowing through human capillaries with simple, relatively low-cost equipment. Combined with deep learning based computer vision algorithms, oblique back-illumination capillaroscopy promises a new chapter of hematologic analysis and biomarker discovery.

Thesis Readers

Dr. Nicholas J. Durr, Ph.D. (Primary Advisor)
Assistant Professor
Department Biomedical Engineering
Johns Hopkins University

Dr. Joseph Webster Stayman, Ph.D., M.S.
Associate Professor
Department Biomedical Engineering
Johns Hopkins University

Dr. Xingde Li, Ph.D.
Professor
Department Biomedical Engineering
Johns Hopkins University

Dr. Luis Andres Garza, M.D., Ph.D.
Professor
Department of Dermatology
Johns Hopkins University

Dr. Mark A. Foster, Ph.D.
Professor
Department of Electrical and Computer Engineering
Johns Hopkins University

To my parents, my professors, my pit bulls,

and my partner Caroline.

Acknowledgements

Throughout my graduate studies and the writing of this dissertation I have received immeasurable support.

First to thank the people who got me here. My parents, my first guides on this planet. You inspired me to pursue science and healthcare and supported me to stay in school as long as I have. Your investment, sacrifice, dedication, and endless love are something special I am so fortunate to have been surrounded by. An expression of gratitude cannot reciprocate everything you've given me. Thank you, from the bottom of my heart. My brother, my biggest role model and best friend from my earliest years. How lucky I am to have you as an example. Thank you to my teachers K-12 including David Andreoni, Donna Colace, Franciscus Hoek, Mary Morin, Patricia Parella, Alfred Petrarca, Donna Pereira, Meredith Poulten. Your enthusiasm for education and teaching left a lasting impression on my developing mind in its most formative years. Thank you to my many college professors and mentors, including Migeul Alonso, Alfred Clark Jr., Julie Bentley, Andrew Berger, Thomas G. Brown, James Farrar, James R. Fienup, Alison J. Frontier, Handy Gelbard, Lewis J. Rothberg, and James M. Zavislan. You challenged me, inspired me, supported me, and created an environment that kept me engaged and excited about science and academia.

To those who admitted me to the Johns Hopkins Medical Scientist Training Program, you have changed my life. Thank you Robert F. Siliciano, Glenn J. Treisman, David Shortle, and the other committee members who granted me this opportunity. Thank you the MSTP director, Andrea Cox, whose work as a physician scientist is inspirational and whose calm, open, and inviting demeanor are a source of immeasurable support. Thank you to the MSTP

administrative staff, Sharon Welling, Martha Buntin, and Bernadine Harper, for their tireless work making the program run smoothly throughout my time here. Your endless personal and professional support have created an invaluable and steady sense of family throughout the years.

Thank you to my medical school professors and advisors, whose guidance and teaching prior to my PhD facilitated my research, deepened my understanding of my project, and inspired me to pursue translational research. Stephen Sozio, Luis Garza, Marc Halushka, Alison Moliterno, and Lydia Pecker, your passion for medicine and research continue to guide me in my career.

Thank you to my mentor, Nicholas J. Durr, for your unwavering support for the past five years. You have dedicated countless hours to my education and development and have provided me with the exact PhD experience I dreamed of. You have been everything a mentor should be every day of my graduate school experience - consistent, reliable, creative, understanding, demanding (yet reasonable), motivational, inspiring, and supportive. You are an incredible role model and advisor, and in these years I have sought only to be more like you both professionally and personally. Thank you for being a continuous source of inspiration to pursue a career in biomedical optics.

To the collaborators Alison Moliterno, Lydia Pecker, Sophie Lanzkron, Ophelia Rogers, Donna Williams, your enthusiasm for this project, lending of reagents, brainstorming, and guidance have been and will be essential to its success. Thank you for your generosity and time.

To all of my lab mates, friends, and peers, in medical school, graduate school, and throughout Baltimore, your enduring support and kindness has been a great source of strength and happiness.

To my thesis committee, Nicholas J. Durr, Xingde Li, Web Stayman, Luis Garza, and Mark Foster, thank you for your mentorship, your guidance throughout the years, and for

your help completing this dissertation on time.

To my pit bulls, Sushi, Ollie, and Jolene for doing nothing, yet being everything. Your constant happiness and excitement to greet me at the end of my longest days are a light that guide me home.

Thank you Caroline, my partner, who has been there for me from the first day of my PhD to my last. You've seen me up close through all the ups and downs, supporting and encouraging me along the way. I couldn't have done it without you. I love you.

Contents

List of Figures

Chapter 1

Introduction

The function and composition of human blood

The circulation of blood through the body is essential for human life. At its most basic level, blood, through the pulmonary and cardiovascular systems, provides the oxygen and nutrients required for cellular function and metabolism to nearly every tissue in the body [63]. Without this critical function, hypoxic brain injury and death occur in mere minutes [64]. Though this crucial function alone would warrant its existence, blood performs a remarkable number of other vital tasks. Blood facilitates an immune response to counter lethal pathogens, it provides thrombosis to minimize hemorrhage during injury, it facilitates nutrient uptake and transportation from the gastrointestinal tract, it provides a transportation system for endocrine and signaling molecules, it removes waste from tissue and transports it for excretion, and plays a crucial role in regulating body temperature. This list is far from exhaustive. Blood accomplishes these many feats through its remarkably complex composition and its circulation to and interaction with every major organ system in the body. A useful framework for understanding the composition of blood is to divide it into two parts: blood cells, and blood plasma [65]. Different types of blood cells are incredibly diverse in morphology, function, and concentration. Blood plasma is a protein, lipid, salt, and sugar rich aqueous buffer that provides the basis for effective circulation, nutrient delivery, and chemical signaling.

A brief history on the discovery of blood cells

While whole blood had been studied through phlebotomy and examination by eye since ancient times, the existence of blood cells was only discovered in the 17th century by Jan Swammerdam using the compound microscope (Figure 1-1(a)) [1, 66]. Until the mid-19th century, the red blood cell, or "red corpuscle" as it was called, was the only known blood cell. The discovery of the leukocyte, or "colorless corpuscle" was made independently and near simultaneously by Gabriel Andral and William Addison while studying disease involving inflammation (Figure 1-1(b)) [2, 66, 67]. Amazingly, the granularity of some white blood cells and even the process of cellular lysis and degranulation was appreciated by Addison at this stage [2, 68]. Neutrophils were first described by Max Johann Sigismund Schultze in 1865, who also identified three other crucial types of white blood cells: the eosinophil, the lymphocyte, and the monocyte [69]. In 1878 and 1879, Paul Ehrlich, a chemist and pioneer of cellular labeling with dyes discovered both the mast cell and the basophil [70–72]. As advances in microscopy and medicine progressed throughout the 19th century, it became clear that another small, yet important cellular blood component was present *in vivo*. Giulio Bizzozero, building upon work by Schultze [69] and Hayem [73], discovered platelets and described their role in hemostasis in the 1880's [74–77]. These discoveries provided the foundation upon which the complete blood cell count is still based.

The turn of the 20th century was met with a rapid expansion in our understanding of blood cell biology [78]. Alexander Maximow described the concept of hematopoiesis and introduced the term "stem cells" to describe the common origin of blood cells [79, 80]. Macrophages were discovered throughout the body independently by different scientists in the turn of the century, many of which still bear their name (Kupffer cells, Langerhans cells, etc.) [78, 81]. Their common origin as circulating monocytes and common function as phagocytotic cells was not fully established until the mid- and late- 1900's [78, 82, 83]. Phagocytosis was a key area of study for the classification of white blood cells and the understanding of the immune system (Figure 1-2) [84]. It was in fact the main focus of Elie Metchnikoff,

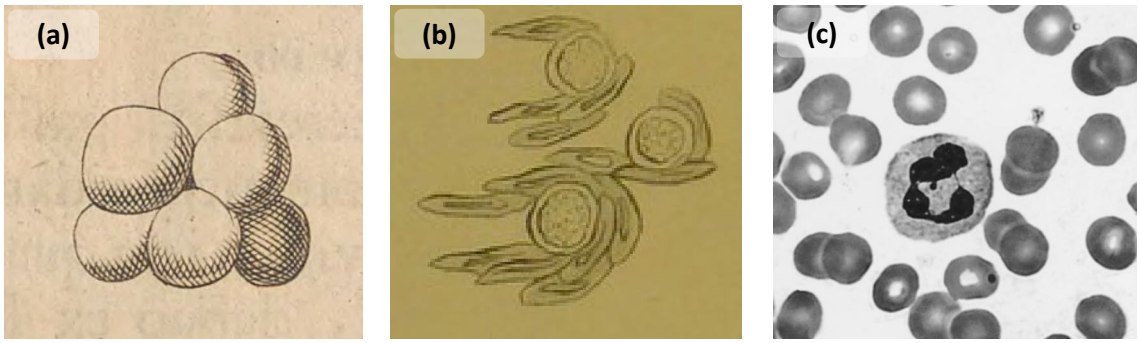

Figure 1-1. (a) The first depiction of red blood cells [1], (b) the first depiction of leukocytes [2], and (c) modern peripheral blood smear image [3].

considered the father of innate and cellular immunity [78, 84]. Despite these incredible advances, progress in the field was tumultuous and far from straightforward. In fact, a cellular focus of immunology came into decline in the 1900's as progress in antibody-based analysis of serum outpaced tools available for cellular analysis [78, 85]. Over the decades, many cell types were discovered and subsequently abandoned for more generalized descriptions [78, 86]. For example, clasmatocytes, polyblasts, adventitia cells, rhagiocrine cells, among others were only recently classified under a common mononuclear phagocyte system [87]. The role of lymphocytes as antibody producers, their further distinction into T- and B-subtypes, and their relationship to plasma cells was not understood until the mid-1900's [88–91]. While many pillars of blood cell classification seem now set in stone, it is likely that the development of new tools for cellular analysis will yield greater insight and still refined classification.

Hematopoiesis and current perspectives of blood cells

The classification of red blood cells, neutrophils, lymphocytes, monocytes, eosinophils, basophils, and platelets, and their common origin provides the foundation for our understanding of the cellular composition and analysis of blood. Each of these cells develop initially from hematopoietic stem cells (lineage-/Sca1+/c-kit+, or LSK), which reside in trabeculae of adult bone (Figure 1-3) [4, 5]. LSKs are a general, self-renewing class of cells that through chemical signaling differentiate into common lymphoid progenitors (CLP) and common myeloid

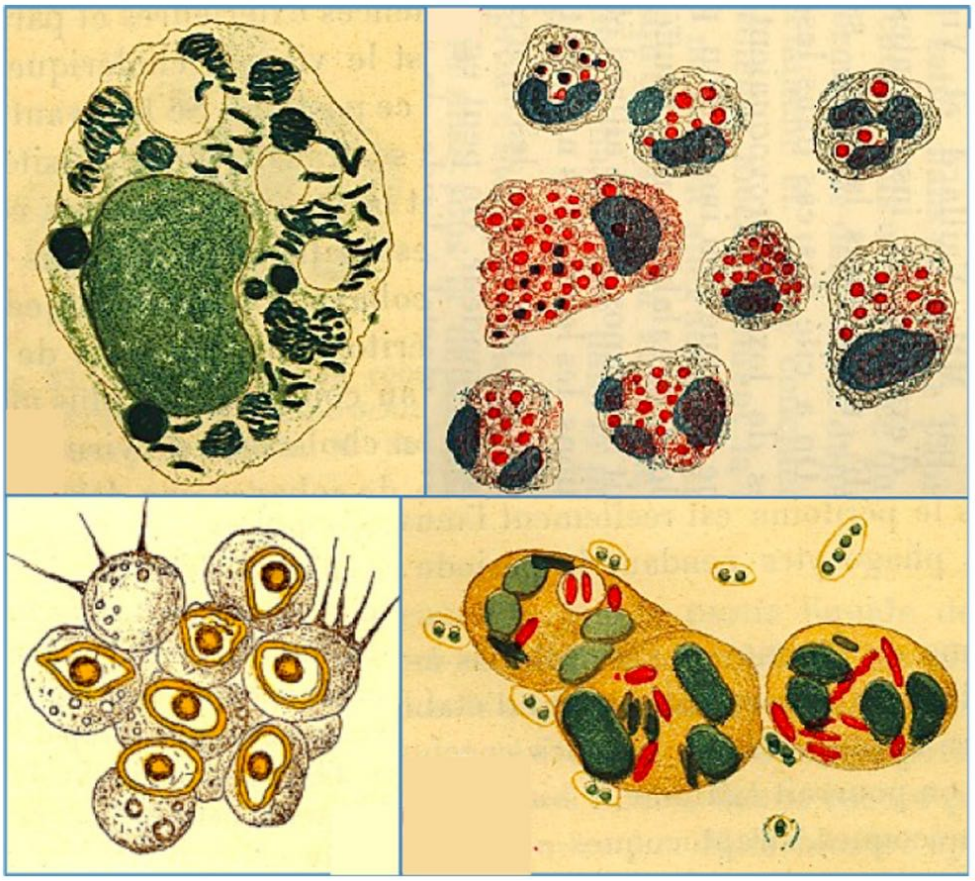

Figure 1-2. Early drawings of phagocytosis [3].

progenitors (CMP). Further differentiation gives rise to each of the blood cell components, with lymphocytes and natural killer cells developing from the CLP lineage, and erythrocytes, monocytes, granulocytes, and megakaryocytes developing from the CMP pathway [5, 92]. Many of these cells continue their differentiation, either locally, or upon arrival to a different tissue within the body. Megakaryocytes slough off platelets into the blood stream, monocytes mature into macrophages in peripheral tissue, and lymphocytes mature into their T- and B-cell sub-types in the thymus, and spleen and lymph nodes, respectively [5, 92, 93]. Amazingly, LSKs create approximately 2 million new red blood cells per second in the steady state [94], and approximately only 100 LSKs are required for the multi-lineage repopulation of irradiated hosts, highlighting their remarkable self-renewing capability [5].

In their normal state, each of the classes of blood cells plays a distinct role in maintaining

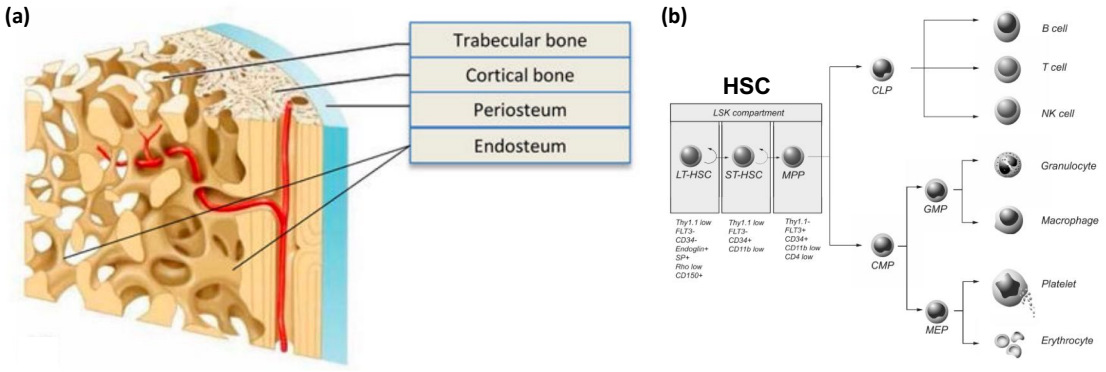

Figure 1-3. (a) Hematopoietic stem cells (HSCs) reside in the vascular-rich trabecular meshwork of bone in adults [4], (b) Blood cells develop from a common stem cell origin through complex molecular pathways [5].

health. Red blood cells (RBCs), characterized by their bi-concave, disk-like morphology, are the most abundant blood cell type (Figure 1-4(a)) [6]. RBCs are highly deformable due to their specialized shape, cytoskeleton, and membrane composition, allowing them to traverse small, winding capillaries throughout the body [95]. They are devoid of nearly all sub-cellular features, such as a nucleus and mitochondria, that characterize typical cells (Figure 1-4(b)), and instead are packed full of a protein called hemoglobin [7, 8, 96]. Hemoglobin is a tetrameric protein containing four iron-bound heme molecules that each bind oxygen and deliver it to peripheral tissue (Figure 1-4(c)) [8]. Importantly, hemoglobin efficiently absorbs visible light in the blue-green wavelengths, shown in Figure 1-4(d), which gives rise to reddish hue of human blood. This phenomena plays a key role the absorption-based contrast utilized in capillaroscopy. Red blood cells are typically 6.9 to 9.3 μm in diameter and 2.4 to 3.7 μm in thickness [97]. Their concentration in whole blood is typically 4-5e6 cells/μL [98]

Platelets are the next most abundant blood cell type, and are released as fragments of megakaryocytes from the bone marrow into circulation [99, 100]. They are usually an order of magnitude lower in concentration than red blood cells, with a typical concentration range of 1.5-4e5 cells/μL [98]. Platelets are small and discoid in shape, approximately 2.5 μm across, nucleus-free, and granular in nature with a highly organized cytoskeleton (Figure 1-5) [99]. They are best known for their coordinated role in clot formation and hemostasis in

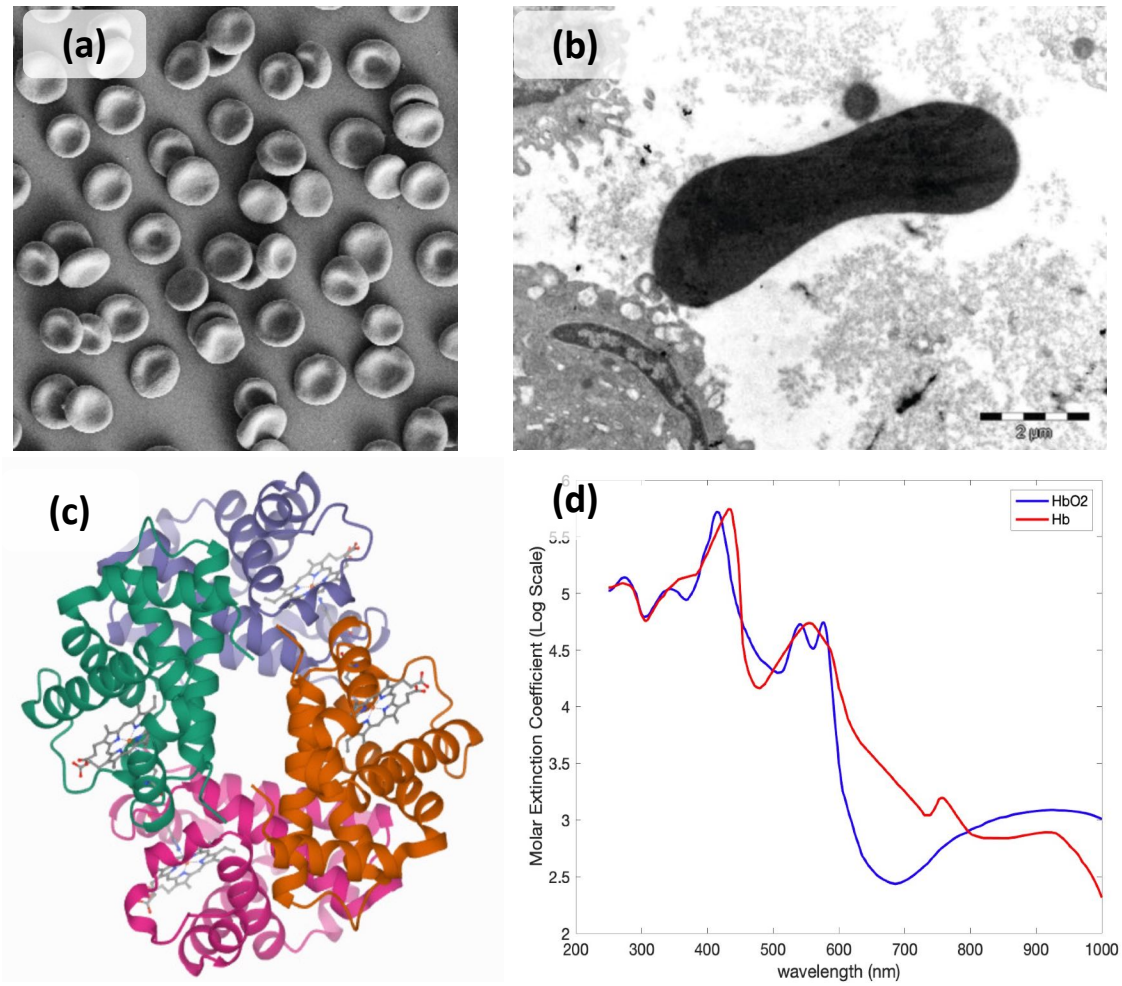

Figure 1-4. (a) Scanning electron micrograph of intact red blood cells [6], (b) transmission electron micrograph of a red blood cell highlighting its homogenous contents [7], (c) the molecular structure of hemoglobin [8], and (d) its absorption spectrum in visible wavelengths [9]

response to the presence of thrombin produced via cellular injury and the coagulation cascade [101–104]. Upon activation, they undergo morphological changes which include degranulation and a reorganization of their cytoskeleton to create cellular projections [99, 105, 106]. The size and granularity of platelets are their two most defining cellular features. There are two major granule types in platelets: (1) α-granules, which contain hundreds of soluble and membrane-bound proteins (including von Willebrand and fibrinogen) are 200-500 nm in diameter and numerous (50-80 per platelet) [99, 107]. (2) δ-granules are typically 150 nm in diameter, numbering 3-8 per platelet, and contain calcium, serotonin, nucleotides, and pyrophosphates [99, 107, 108]. Degranulation of these contents is essential in a variety of

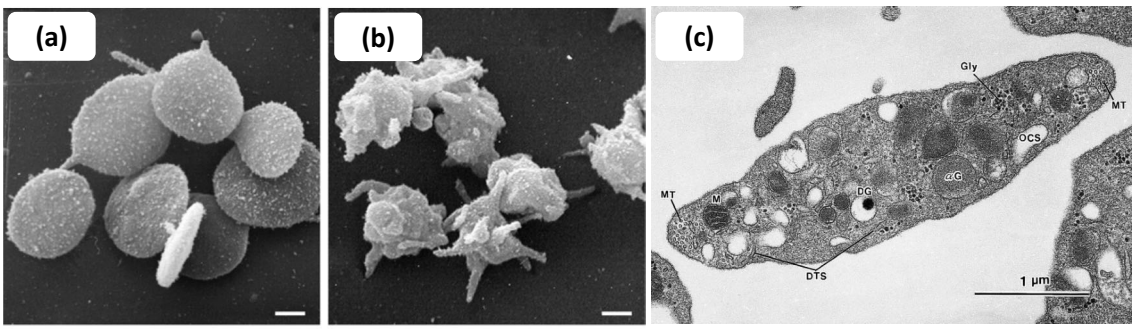

Figure 1-5. (a) Scanning electron micrograph inactivated platelets, and (b) activated platelets [10] (1 μm scale bars), (c) transmission electron micrograph cross section of a platelet showing α-granules (αG), δ-granules (DG), mitochondria (M), glycogen particles (Gly), microtubules (MT), open canalicular system (OCS), and dense tubular system (DTS) [11].

physiological processes including coagulation, angiogenesis, inflammation, and tissue repair.

In a healthy individual, neutrophils are typically the most abundant white blood cell and the next most common blood component with a concentration range of 2-7e3 cells/μL [98]. Despite being 1000-fold lower in concentration than RBCs, they account for the greatest portion of hematopoiesis, due to their relatively short lifespan in circulation (half-life $<$ 1 day) [109]. Neutrophils are slightly larger and more spherical than red blood cells, with a diameter of 7-15 μm in circulation (Figure 1-6) [110, 111]. They are phagocytic, bactericidal and fungicidal cells that play a crucial role in the primary immune response [109, 110, 112]. They are characterized by their multi-lobed, segmented nuclei and a cytoplasm filled with three major types of secretory, pro-inflammatory granules [110]. Azurophilic (or primary) granules are rich in myeloperoxidase, elastase, proteinase, and cathepsin [109, 110] and mediate antimicrobial activity through both oxidative and non-oxidative means. Specific (or secondary) granules contain NADPH oxidase, alkaline phosphatase, collagenase, and lactoferrin, and outnumber the azurophilic granules approximately 2-3:1 in mature neutrophils [109, 113]. Tertiary granules contain gelatinase, arginase, and lysozyme and are essential for extravasation of the neutrophil through the endothelium [109]. The granules of neutrophils are heterogenous in size and shape, ranging 0.1-1 μm in diameter [13, 114, 115].

The next most common white blood cell type is the lymphocyte, which is typically at a

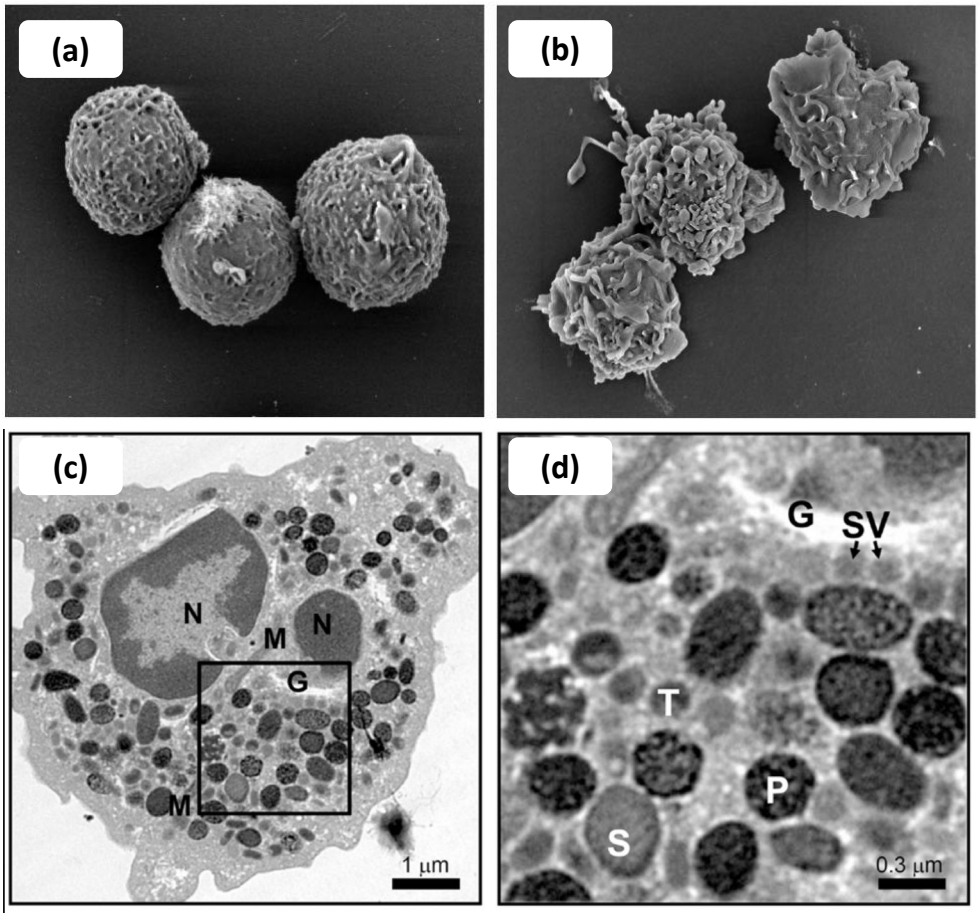

Figure 1-6. (a) Sanning electron micrographs of quiescent, and (b) activated neutrophils [12]. (c)-(d) Transmission electron micrographs cross section of a neutrophil showing lobed nuclei (N), golgi complex (G), mitochondria (M), primary granules (P), secondary granules (S), and tertiary granules (T) [13].

concentration of 1-3e3 cells/μL in whole blood [98]. Lymphocytes are relatively small white blood cells, 7-10 μm in diameter, with no granules and a nucleus that often encompasses most of the total cell volume (Figure 1-7) [111, 116]. There are three major different types of lymphocytes: T cells, B cells, and innate lymphoid cells (ILCs), which include natural killer (NK) cells [116, 117]. T cells are the most abundant in whole blood, comprising approximately 80 % of the lymphocytes in circulation [116]. Though relatively rare compared to other lymphocytes in healthy individuals, there exists an additional class of lymphocyte, the large granular lymphocyte (LGL), which can be either T-cell or NK-cell in origin [116]. These cells are variable in size 10-12 μm normally, but can be enlarged $\geq$ 14 μm in cases of leukemia.

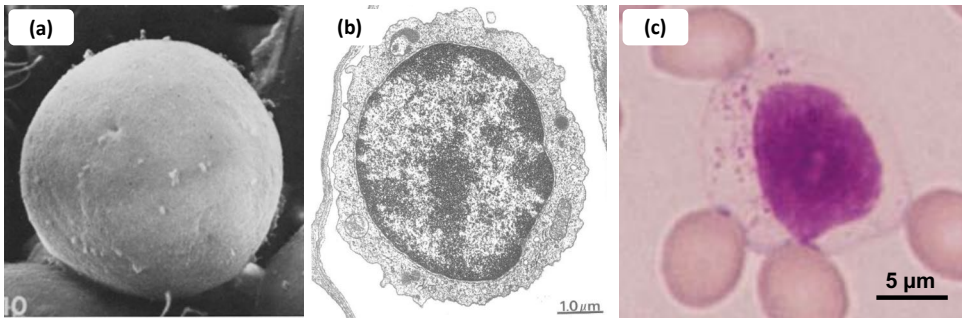

Figure 1-7. (a) Scanning electron micrograph of a lymphocyte [14], (b) transmission electron micrograph cross section of a lymphocyte showing single large nuclei and scant cytoplasm [15], (c) a large granular lymphocytes in a peripheral blood smear [16].

Additionally, though their nuclei is still globular, their cytoplasm is significantly enlarged and they contain granules, which are atypical findings for most lymphocytes [16, 118, 119]. Lymphocytes play a diverse and critical role in the immune response, facilitating a specific immune response to antigens produced by pathogens through direct cell killing and antibody production, creating memory of molecular signals that facilitates a more robust immune response upon secondary exposure, and regulating the immune response to keep it in check [116, 120, 121].

Monocytes are the third most abundant leukocyte in circulation at a concentration of 200-800 cells/μL [98]. They are on average the largest leukocyte, with a diameter of 12-20 μm, and are characterized by a large, often bi-lobed nucleus (Figure 1-8) [111]. They often have ruffled edges, which can grow to impressive projections when the cell is activated in an immune response. Monocytes are diverse in their form an function, but their primary role is to extravasate from blood vessels into peripheral tissue and mature into phagocytic macrophages and antigen presenting dendritic cells [122–124].

Eosinophils, like neutrophils, are a class of granulocyte, and are the second least abundant cell of a standard complete blood count in circulation. Their concentration is typically only 30-450 cells/μL [98]. These cells are characterized by numerous, large granules in their cytoplasm that efficiently absorb the reddish dye eosin, and ultimately gave rise to their name [125]. Eosinophils are similar in size to neutrophils, with a diameter of 9-15 μm, and typically

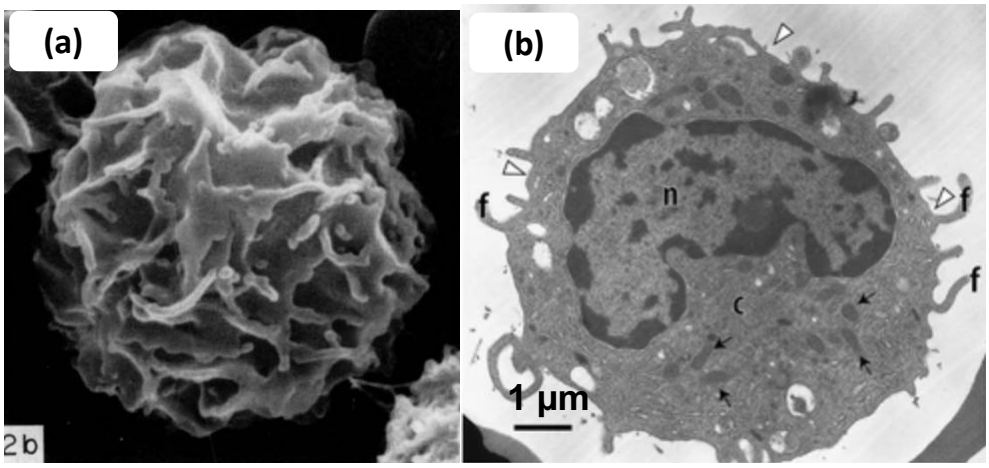

Figure 1-8. (a) Scanning electron micrograph of a monocyte showing ruffled membrane edges [17], (b) transmission electron micrograph cross section of a monocyte showing characteristic large cell with bilobed nucleus and abundant cytoplasm largely devoid of granules [18].

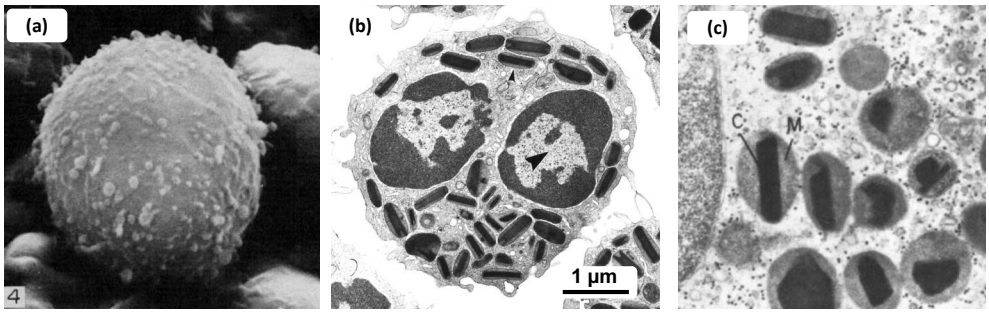

Figure 1-9. (a) Scanning electron micrograph of an eosinophil [19], (b) transmission electron micrograph cross section of an eosinophil showing its bi-lobed nucleus and abundant, crystalloid-containing dense granules [20], (c) enlarged eosinophil granules showing a matrix outer layer (m) surrounding a crystalline core (c) [20].

have a bi-lobed nucleus (Figure 1-9) [111, 125]. Despite their relative rarity, eosinophils play a crucial role in asthma and the immune response to parasitic disease [125–127]. Eosinophil granules are classified into two types: primary and secondary (or specific). Primary granules contain Charcot-Leyden crystal and secondary granules contain a tri-laminary membrane that surrounds an electron-dense crystalline core [20, 125, 128]. Though their outer appearance and size can be indistinguishable from neutrophils, eosinophil granules with their crystalline core are characteristically different (Figure 1-9(c) vs. Figure 1-6(d)).

Of the seven routine blood cells classified in a conventional complete blood count, the basophil is typically the least abundant with a concentration range of 10-80 cells/μL [98].

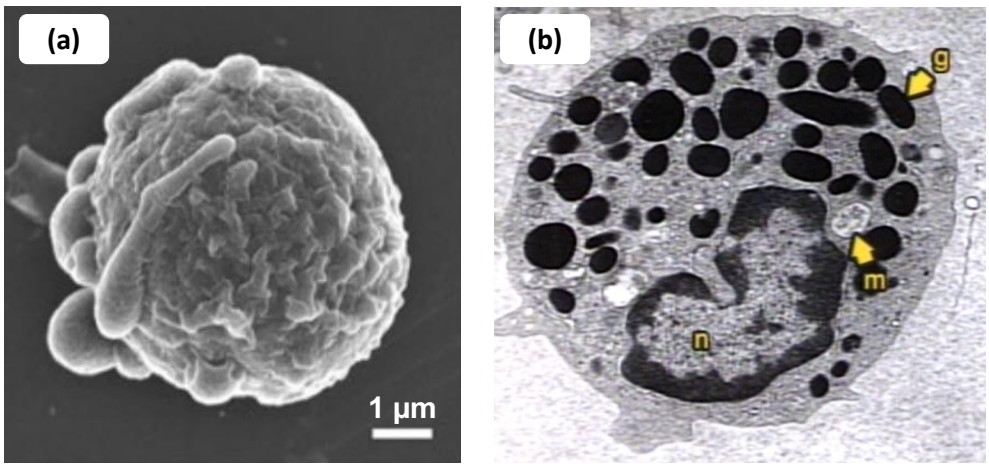

Figure 1-10. (a) Scanning electron micrograph of an basophil [21], (b) transmission electron micrograph cross section of an basophil showing its bi-lobed nucleus and abundant, histamine-containing dense granules [22].

Basophils are typically 10-16 μm in diameter in humans, and are characterized by a bi-lobed nucleus and numerous large granules that stain blue in conventional hematoxylin and eosin preparation [111, 129]. The most distinct granules of a basophil are large, relatively homogenous and dispersed throughout their cytoplasm [129]. These granules contain most of the histamine in the body and have interspersed Charcot-Leyden crystal [130–132]. Basophils are critical in coordinating the allergic response and fighting multicellular parasites [133, 134]. Figure 1-10 shows the fine details of a basophil and its granules through electron microscopy.

Together, these seven cell types, red blood cells, neutrophils, monocytes, lymphocytes, basophils, and eosinophils represent the major classes of cells identified on a complete blood count. While other cells can exist in circulation in health and disease, the ubiquity of these cells and their role in common clinical disorders make them a reasonable starting point for investigating non-invasive blood cell imaging. However, before doing so, it is important to have a general understanding of blood plasma, the medium in which these blood cells exist.

Blood plasma

Blood plasma is an extracellular milieu that is precisely titrated to keep blood cells in circulation stable throughout the body. In a healthy individual, approximately 55-65 % of

whole blood is blood plasma by volume, where as the remaining volume is comprised of the blood cells themselves [98]. Though blood plasma is an aqueous solution that is up to 95 % water, it is full of a complex and rich number of proteins, lipids, carbohydrates, salts, amino acids, inorganic compounds, metabolites, and other small molecules [135, 136]. The importance of blood plasma is equal to that of the blood cells it surrounds. It provides a medium for oxygen and carbon dioxide transportation to peripheral tissues and to the lungs to enable respiration, it transports nutrients in the form of amino acids, carbohydrates, lipids, and lipoproteins to enable cellular metabolism, it contains clotting factors such as fibrinogen that are essential to hemostasis, it brings nitrogenous and other waste compounds to the kidneys for excretion, it circulates our vitamins, our cholesterol, and our hormones [135]. This list is far from exhaustive, and a complete list of compounds and their concentrations is outside the scope of this work. Unfortunately, the molecules and compounds of blood plasma are mostly too small to be visualized with conventional microscopy techniques due to diffraction limitations and their weak scattering of light. Of note, however, chylomicrons, the largest lipoproteins in blood plasma could be resolved as their 200-600 nm diameter is around the diffraction limit of conventional microscopy [137]. Lastly, while most of the constituents of blood plasma will be indiscernible using the optical techniques described in this thesis, the composition of blood plasma plays a critical role in whole blood viscosity, that can ultimately change the rheology of blood flow [136].

Blood analysis

Clinical blood analyis is a cornerstone of modern healthcare as the study of blood provides critical insight into health and disease. There are numerous types of blood tests, including:

- Blood gas is measured often through arterial draw to test pH, oxygen, and carbon dioxide content and provide insight into respiratory function [138].
- A comprehensive metabolic panel assesses the concentrations of a wide array of blood

plasma constituents including blood urea nitrogen and creatinine to test kidney function, alkaline phosphatase, alanine transaminase, aspartate aminotransferase, and bilirubin, to test liver function, total protein and serum albumin, and a few other critical compounds such as sodium, glucose, calcium, potassium, chloride, and carbon dioxide [139].

- Coagulation studies, including activated partial thromboplastin time, prothrombin time, assays for specific coagulation factors, and fibrin D-dimer, each probe different etiologies of bleeding and clotting disorders [140–143]
- Blood culture to test for bacteremia [115].
- Blood cardiac enzyme testing to investigate myocardial injury [144]
- A complete blood count (CBC) with differential to determine the concentration of various blood cells in solution [3, 145, 146]
- A blood smear to further investigate abnormalities in blood cell composition [3, 147, 148]

Though each of these tests are crucial for patient care, the most relevant to this thesis are the complete blood count and the blood smear as they both probe the cellular composition of blood, which is directly observable with the microscopy technique presented here.

The complete blood count

The invention of the microscope and its application to imaging blood provided the early foundation of blood cell counting [149]. In the 19th century, around the same time different types of white blood cells were being discovered, it became apparent that their relative abundance was variable [70–72, 149]. Early medical scientists suspected that measuring the concentration of blood cell types could yield fruitful insight into health and disease, and they accomplished the first cell counting experiments manually with early cell counting chambers (the hemacytometer) [149]. Though insightful, it was clear that manual counting of blood cells was too time intensive to be an effective clinical tool. Through the turn of

the century and into the 1900's, manual counting gave way to new, high-throughput cell counting technologies based on flow cytometry and measurement of cellular impedance and light scattering [149–151]. While the exact origin of this technique is difficult to label due to its success requiring the combination of numerous new and old technologies, credit is often given to Andrew Moldovan, who was the first to measure cells sequentially flowing in suspension through a glass capillary tube in 1934 [150–153]. In the decades since this experiment, advances in electronics, fluidics, and sensors have enabled flow cytometric blood cell analysis with incredible precision and throughput [149–151].

Modern cell counters typically still rely on three general principles: (1) measurement of electrical impedance, (2) measurement of light scattering, and (3) measurement of fluorescent molecule binding (Figure 1-11). The first principle, relying on electrical impedance, is based on the concept that cells are generally weak electrical conductors as compared to background blood plasma or buffer. Cells passing through an electrical field will provide a decrease in current between two electrodes that is proportional to the cells size. This was first discovered and investigated by Wallace Coulter in the 1940's, and the phenomena still bears his name as the "Coulter effect" [149, 154]. The second principle based on light scattering, makes use of the dependence of the directionality of scattered light on cellular size and granular content [149, 155]. Generally, larger particles (those larger than the wavelength of light) tend to scatter light in the forward direction, while smaller particles approaching the wavelength of light (and sub-wavelength) scatter proportionally more light in the side direction [156–159]. In the case of blood cells, whose diameter is roughly 5-15 μm, and using visible wavelengths 0.4-0.7 μm, light tends to forward scatter. This is the case in cells such as lymphocytes, whose large, spherical nucleus and scant cytoplasm scatter light primarily forward. Contrasting this are granulocytes, whose cytoplasm are punctated with numerous sub-cellular granules approximately 0.1-1 μm in diameter that efficiently scatter light in the side direction (Figure 1-11(c)) [156–159]. The third principal technique in flow cytometry is the use of cellular fluorescent labeling. By adding numerous, exogenous fluorescent dyes to the *ex vivo* blood,

sub-populations of blood cells can be marked and detected with high specificity [149–151, 160]. This technique can be used to enable cell sorting and distinguish between populations of blood cells that exhibit similar impedance or scattering profiles, such as sub-types of granulocytes, or to distinguish immature granulocytes from mature granulocytes [149, 150].

The Hemalog-D by Technicon was the first commercial flow cytometric differential counter, and gave rise to the clinical establishment of the white blood cell differential [151]. Today, it is common for hematologic analyzers to use 5-11 distinct fluorescent channels, and some research analyzers use multiplexing to distinguish up to 40 different types of immune cells [149, 151]. Modern hematologic analyzers can measure dozens of cellular properties at 100,000-200,000 cells per second, an astounding feat when compared to manual cell counting of the early 20th century [149, 151]. Most commonly, a clinical hematologic analyzer provides a CBC that includes red blood cell concentration ([RBC], cells/µL), platelet concentration, and a 5-part white blood cell differential (neutrophils, lymphocytes, monocytes, eosinophils, and basophils). Whole blood is further analyzed to determine its hemoglobin concentration (Hgb,g/dL) and hematocrit value (Hct, %, the blood cell volume fraction of whole blood), and from these, other metrics about red blood cells are computed, including the mean corpuscular volume (MCV), mean corpuscular hemoglobin (MCH), and the mean corpuscular hemoglobin concentration (MCHC) according to equations (1.1)-(1.3) below. Other metrics are often also reported, such as the red cell distribution width, the immature granulocyte percentage, and the mean platelet volume. Each of these metrics can provide valuable clinical information, and it is no surprise that the complete blood count has become one of the most common laboratory tests ordered [149, 161].

$$MCV = Hct * 10/[RBC] \tag{1.1}$$

$$MCH = Hb * 10/[RBC] \tag{1.2}$$

$$MCHC = Hb/(Hct/100) \tag{1.3}$$

Despite their tremendous success, conventional hematologic analyzers have a few major drawbacks. They are large, heavy, benchtop systems that require supporting laboratory staff and equipment to perform their duties. These constraints make the development of an accurate, portable, and inexpensive complete blood counter for low-resource settings still an active area of research. Interestingly, to meet this demand, there is a resurging interested in image-based cell counting, driven by their potential for portable systems, simpler sample preparation, and advances in sensor and image processing algorithms [149, 162]. Further, direct imaging of blood cells yields access to cellular morphological information unavailable with conventional hematologic analyzers. The limitations of imaging-based cell counters are largely in throughput, as field-of-view and magnification tradeoff make the classification of rare white blood cells increasingly difficult without complex slide scanning techniques [149]. Recently, the application of holographic lens free imaging to blood cells has shown tremendous promise to large volume imaging [163–165]. However, both of these techniques require *ex vivo* blood, which is typically achieved invasively though a blood draw or finger stick. This inevitably may alter cell properties such as cell markers and morphology, prevents the study of inter-cellular interactions in their native environment, and can exacerbate iatrogenic infection in the immunosuppressed and anemia in neonates [31, 146, 146, 149, 166, 167]. Efforts towards in vivo blood cell counting are an active area of research and the main focus of this thesis.

The blood smear

If an abnormality in the blood is clinically suspected or identified with the CBC, a blood smear should be evaluated next [148]. In this test, whole blood is spread into a monolayer on a glass slide and stained using the Wright-Giemsa protocol [168]. The smear is then evaluated using brightfield microscopy by a hematologist, either through direct viewing or

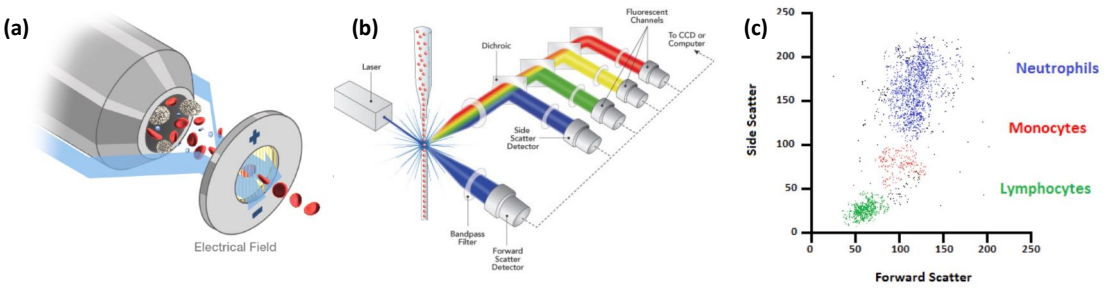

Figure 1-11. (a) Schematic of the use of electrical impedance in complete blood counting [23], (b) schematic of combined light scattering and fluorescent labeling for blood cell analysis [24], (c) examples of forward- to side- scatter ratio that can distinguish white blood cell sub-populations [25].

digital acquisition and display of a whole slide scan [3, 162]. Sometimes, if the sample is flagged by the automatic hematologic analyzer, a manual leukocyte count is performed at this stage to ensure an adequate white blood cell differential despite potential abnormalities. The combination of these two tests, the CBC and the blood smear provides the concentration and morphological features of blood cells, and are the basis for evaluating a clinical hematology case [169].

Figure 1-12 shows the seven major components of a complete blood count after being stained and imaged. Note that the absorption-based contrast imparted by the eosin and methylene blue of the Wright-Giemsa stain provide excellent contrast to red blood cells, white blood cells, nuclei, and granules. While red blood cells, platelets, and white blood cells can be distinguished by their size and presence/absence of a nucleus, sub-cellular features are required to distinguish between white blood cells. For example, a neutrophil's multilobed nuclear shape and small, weakly staining granules distinguish it from the other granulocytes [26]. The resolution of similar morphological features with a label-free approach is significantly more challenging, but critical to establishing an accurate white blood cell differential.

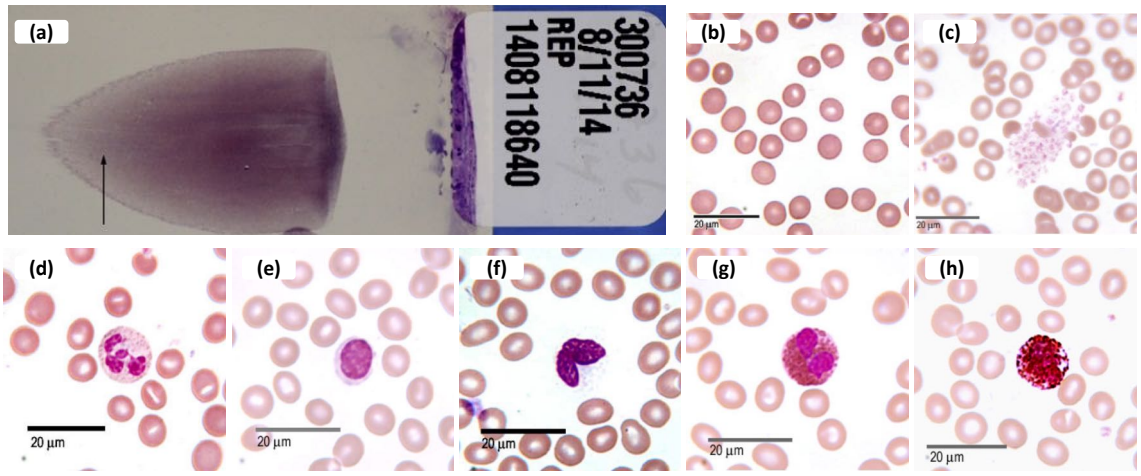

Figure 1-12. (a) A peripheral blood smear showing a feathered spread and monolayer (arrow) [26], (b) red blood cells, (c) platelets, (d) a neutrophil, (e) a lymphocyte, (f) a monocyte, (g) an eosinophil, and (h) a basophil [27].

Non-invasive blood cell imaging

Over centuries, *ex vivo* blood cell counting and analysis has evolved from the discovery of blood cells to efficient flow-based automated analysis of cells with impedance, scattering, fluorescent, and digital whole slide scanning microscopy. These advances are astounding and have yielded clinical tests that are fundamental in modern healthcare. While impressive advances are still underway in this field, for example full 3D cell imaging flow cytometry using optical tomography [170] or the ever increasing number of fluorescent channels and measured cellular parameters, a new avenue for blood cell analysis based on *in vivo* imaging is gaining traction.

The development of *in vivo* blood cell imaging, counting, and analysis is appealing for its ability to provide clinical data without phlebotomy or laboratory processing, enabling real-time and near-continuous measurements of trending blood cell parameters, enabling the evaluation of blood cells in their native environment, and perhaps even sampling larger volumes of blood for the detection of rare cells [149]. This technology could enable screening of hematologic disorders in low-resource settings without access to conventional lab equipment, reduction of blood draw and nosocomial infection in immunocompromised patients, and

reduction of iatrogenic anemia in newborns. Analogous to *ex vivo* blood cell analysis in the early- and mid- 1900's, this is a nascent field with both numerous obstacles to overcome and tremendous potential. There are currently several different types of imaging modalities under study for non-invasive blood cell imaging. The simplest and most relevant to this work is capillaroscopy, which is explored next.

An overview of conventional capillaroscopy

Due to its simplicity, safety, compact nature, and ability to resolve human vasculature in a label-free manner, capillaroscopy has emerged as a promising tool in non-invasive blood cell imaging. Capillaroscopy is a simple form of intravital microscopy where tissue is illuminated with visible light, and absorption by hemoglobin within red blood cells generates contrast to background tissue (Figures 1-4 and 1-13). For white light illumination, vasculature appears darker and redder, as hemoglobin absorbs blue and green wavelengths efficiently. Background tissue, without other pigment such as melanin, will appear bright, allowing blood vessels to be easily visible. Capillaroscopy generates contrast to vasculature in a label-free manner, meaning there is no need for exogenous dyes or fluorophores to be injected into the subject.

Capillaroscopy was first documented in 1663 when Kolhaus studied the vasculature surrounding the fingernail with a early microscope. [30, 171]. Over the course of hundreds of years, improved research in nailfold capillaroscopy methods were coupled with discoveries of its relevance to clinical practice [30]. An early prototype capillaroscope is shown in Figure 1-13(a), with an artistic sketch of nailfold capillaries from around this same time period in (b). Studies of rheumatic disease with capillaroscopy have shown characteristic changes in microvascular size and morphology. It also plays a critical role in determining the cause of Raynaud's phenomenon, diagnosing microvascular issues and predicting finger ulceration from scleroderma and systemic sclerosis, and predicting response to therapy in dermatomyositis [29, 36, 172, 173]. Despite its long history, capillaroscopy-based clinical research is still underway in studying diseases such as diabetes, where microvascular injury is

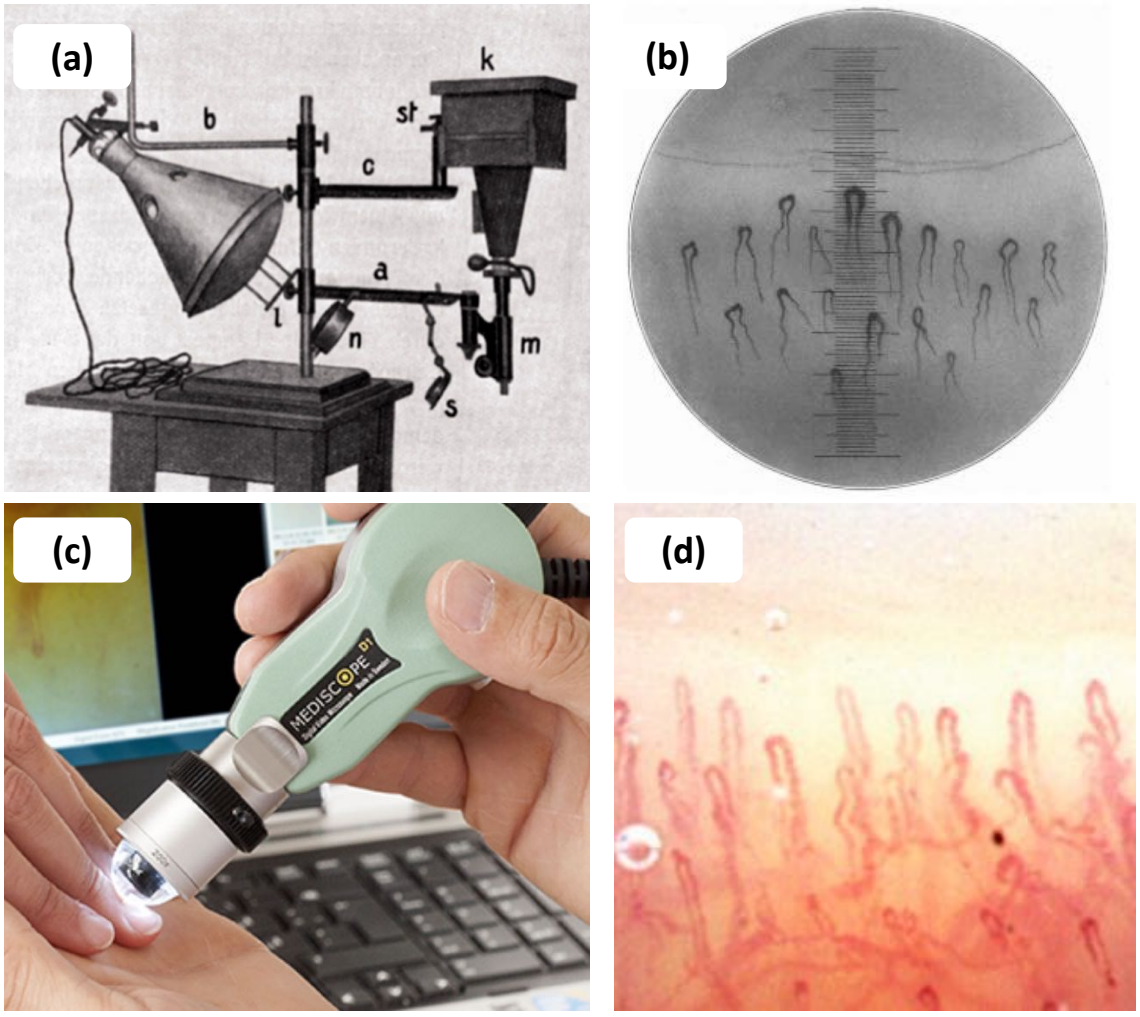

Figure 1-13. (a) A capillaroscope prototype of the early 1900's, (b) drawings of nailfold capillaries acquired at a similar historical time. (c) A modern clinical capillaroscope, and (d) an image acquired of nailfold capillaries with a modern capillaroscope [28–30].

common, and even seemingly unrelated disease such as schizophrenia [174, 175]. Commercially available capillaroscopes (Figure 1-13(c)-(d)) now offer physicians a clear and easy window into microvascular function.

A typical capillaroscope optical system is shown in Figure 1-14. A capillary bed is flood-illuminated with green or blue incoherent illumination. Back-scattered light passes through the infinity corrected microscope objective, and is imaged onto a 2D CMOS sensor with a tube lens. A conventional capillaroscope requires no moving parts, no scanning system, no structured illumination, and its speed is thus dependent only on the sensor frame

rate. Its simplistic design enables it to be readily miniaturized through any number of portable microscopy techniques. With rapid and continuous improvement of optical imaging components, light sources, high speed sensors, and deep learning-based computer vision algorithms, capillaroscopy is undergoing a renaissance in the 21st century [36, 176]. These new technologies show promise that extends beyond the assessment of capillary morphology to enable non-invasive blood cell counting and analysis. For example, high speed imaging of nailfold capillaries has recently shown the ability to non-invasively identify patients who are severely neutropenic by quantifying the frequency of optical absorption gaps (OAGs), the gaps between red blood cells (Figures Figure 1-14 and 1-15) [31–33]. However, though the OAG frequency does correlate with neutropenic status, the exact composition of OAGs cannot be determined using conventional capillaroscopy. Without a more sensitive technique, it is impossible to fully distinguish white blood cells from blood plasma, or to further sub-classify white blood cell type. While there are many ways this could be done, the work in this thesis will focus on the use of phase contrast microscopy to resolve optical absorption gaps.

Despite the impressive advances made in nailfold capillaroscopy and its application towards non-invasive blood counting in the last decade or so, the field faces some fundamental limitations due to nailfold capillary anatomy highlighted in Figure 1-16. First, nailfold capillaries are typically 150-400 μm deep [34]. Thus multiple scattering significantly degrades any attempt of structured illumination imaging techniques. Second, melanin, concentrated in the epidermis superficial to the capillaries, absorbs efficiently at the same wavelengths as hemoglobin and thus degrades contrast to red blood cells. Techniques such as those shown in Figure 1-15 for non-invasive neutropenia screening only work in individuals with Fitzpatrick skin phototype $\leq$ IV [31–33]. These constraints motivate an anatomical survey to find superficial capillary beds beneath minimal melanin, to create a non-invasive blood cell imaging device that provides the highest resolution possible and works regardless of skin type.

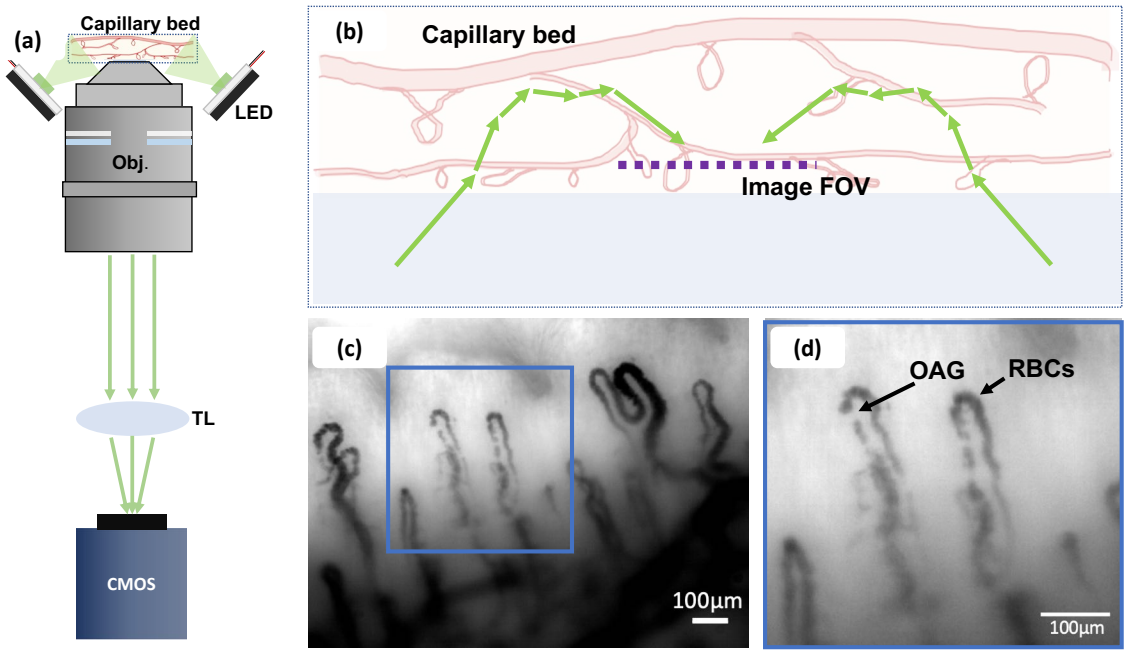

Figure 1-14. (a) Schematic of a typical capillaroscope where green light from an LED flood-illuminates a capillary bed (b), and back-scattered light is collected by a microscope objective. A tube lens (TL) is typically used to image the collimated light from the infinity corrected objective onto a 2D CMOS sensor. (c)-(d) An example monochrome image and enlarged region of interest captured with a similar system to (a) showing red blood cell shadows (RBCs) and bright an optical absorption gap (OAG) between RBCs.

The anatomy of the skin, superficial vasculature, and blood flow

Two major obstacles to *in vivo* blood cell imaging are: (1) the combined anatomy of human skin and vasculature, and (2) the ability to resolve cellular features with a label-free approach. Unlike both conventional flow cytometry and peripheral blood smears where blood cells are analyzed in an optically transparent medium (glass), *in vivo* blood cell imaging requires viewing blood cells surrounded by bulk human tissue, an opaque, turbid medium. Further, both of these *ex vivo* techniques make direct use of transmission-based analysis, where the light source and sensor are placed on opposite sides of the sample, which enables access to forward-scattered light that contains critical cellular structural detail [177, 178].

A schematic of typical skin and superficial vasculature anatomy is shown in Figure 1-17. Most of the skin in the human body consists of three layers: an avascular epidermis whose keratinocytes mature from the stratum basale into the enucleated stratum corneum and

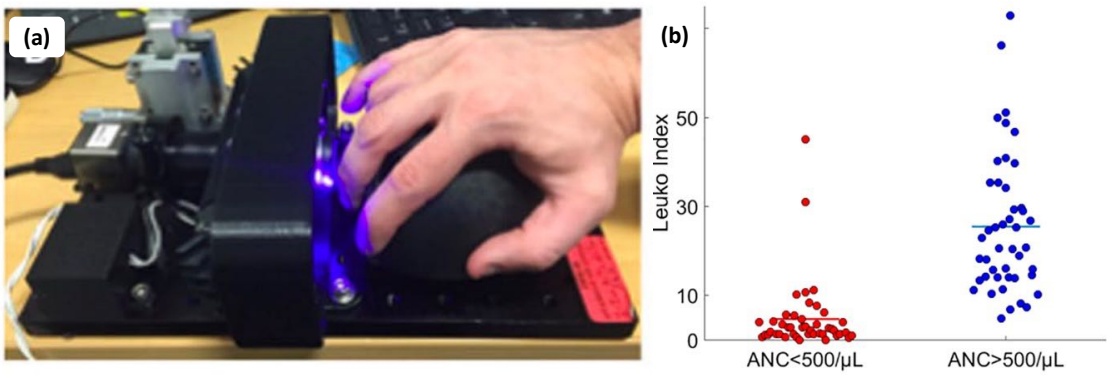

Figure 1-15. (a) A modern high-speed capillaroscope that is capable of (b) distinguishing neutropenic subjects with absolute neutrophil count (ANC) $< 500/\mu$L and normal controls. [31–33]

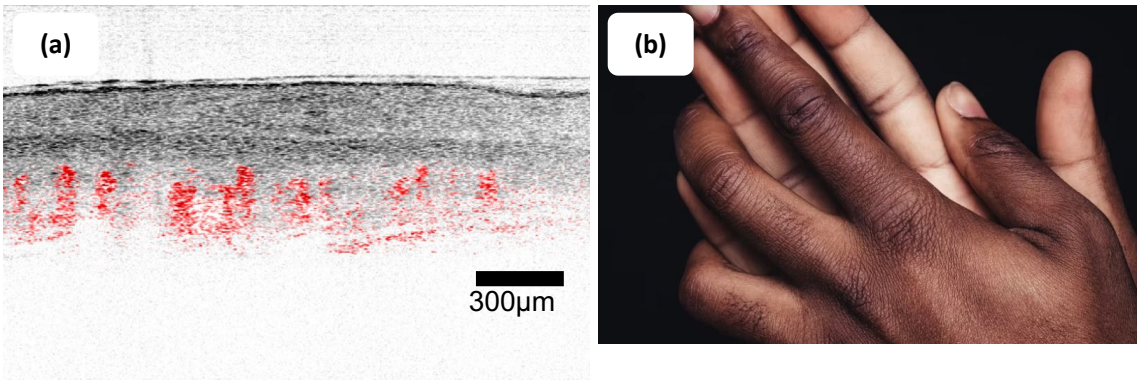

Figure 1-16. (a) A doppler OCT cross section of nailfold capillaries confirming their depth stated in literature is typically 150-400 μm [34]. (b) Melanin, which absorbs the visible light generating contrast to RBCs in capillaroscopy, is concentrated in the epidermis of peripheral skin such as the nailfold.

eventually slough off, a deeper dermis that contains nerves, arteries, and veins, and the hypodermis, the deepest layer rich in adipose tissue [35, 36, 179]. The vasculature in this region is also separated into three layers: the largest vessels of the subcutaneous plexus give rise to the reticular plexus in the dermis, which further branches into the papillary plexus giving rise to the terminal arterioles, capillary loops, and post-capillary venules [35, 36, 179]. Generally speaking, the more superficial the vasculature, the smaller its diameter becomes. Vessels < 300 μm in diameter are generally classified as microvasculature, which are the most relevant type of vasculature for the imaging modalities under study here. Arterioles of the superficial papillary plexus are 10-100 μm in diameter, innervated, and surrounded by

smooth muscle to enable vasoconstriction and vasodilation [35, 36, 179, 180]. They typically run parallel the tissue surface, with smaller branches diverging perpendicularly upward to create the capillary loops (Figure 1-17(c)-(d)). Capillaries are the smallest form of vessel in the body and are responsible for the majority of the oxygen transfer from red blood cells to peripheral tissue [181]. They are typically only 5-8 μm in diameter forcing blood cells to pass single file through their characteristic loops [180]. Capillaries empty into the post-capillary venule, vessels 10-200 μm in diameter again surrounded by smooth muscle.

It is critical to also discuss capillary distribution, morphology, and blood flow as additional parameters when considering *in vivo* blood cell imaging. The optimization of single-file blood flow without clotting through fluidic chambers for automated hematologic analysis was a critical step in their success. Blood cells flow at approximately 10 m/s in flow cytometers, enabling their high throughput measurement [149]. However, *in vivo* blood cell velocity can vary immensely depending on blood vessel size. For example, in the largest vessels such as the aorta, blood is pumped at velocities close to 1m/s [182]. However, as vasculature branches into smaller and smaller vessels with increasing net cross-sectional area, blood velocity drops down to 100-1000 μm/s at the capillary level [149, 183–185]. Additionally, blood cells do not pass single-file through vasculature, except at the smallest of vessel size, the capillary. Human capillary density also varies significantly across the body. In peripheral skin, capillaries are anywhere from 16-65 capillaries per mm^2, whereas in muscle the capillary density is nearly two orders of magnitude greater [36, 186].

Capillaries of the skin loop within the dermal papillae, a small fold in the dermal-epidermal junction that provides the most superficial access to vasculature in peripheral skin [35, 36, 179, 180]. Due to the close proximity of the capillary to the dermal-epidermal junction in this region, the epidermal thickness provides a useful approximation of capillary depth. However, human skin is incredibly diverse in its composition and microanatomy even when considering different anatomical locations across a healthy patient. The epidermal thickness typically ranges from 60 - 600 μm, a huge range when considering optical imaging modalities

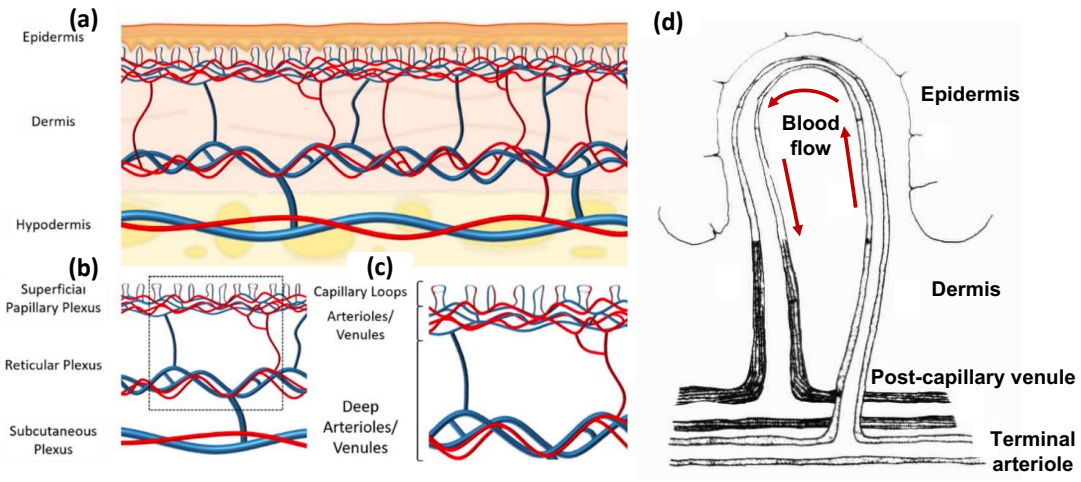

Figure 1-17. (a) The skin consists of three layers, the avascular epidermis, the vascular dermis full of connective tissue, and the underlying lipid-rich hypodermis. (b) Deeper layers of vasculature such as the subcutaneous plexus give rise to the reticular plexus and superficial papillary plexus in the dermis. (c) The most superficial vasculature consists of arterioles and venules giving rise to capillary loops within dermal papillae. (d) Drawing of a capillary loop within a dermal papillae, typically the most superficial form of microvasculature in the human body. [35, 36]

due to the opacity of biological tissue [36, 187, 188]. Measurements of optical properties of human skin are equally diverse, which is unsurprising given the impressive complexity of epidermal microscopic structure, variability of each layer's thickness throughout the body, and difference in melanin concentration. Generally speaking, a reduced scattering coefficient of $\mu_s' = 1 - 2mm^{-1}$ is reasonable for visible wavelengths, and the absorption coefficient is $\mu_a = 0.01 - 1mm^{-1}$ [189–192]. Thus, the range of epidermal thicknesses throughout the body means that the even the most superficial capillaries in the body can range between 0.5 - 12 mean free paths deep. Further, many optical imaging modalities using visible wavelengths, such as capillaroscopy used here, fail to resolve even superficial capillaries of individuals with darker skin tones due to melanin distributed in the epidermis, superficial to the capillaries.

The appropriate choice of anatomical location for human vascular imaging is paramount for its success and thus a critical part of this thesis. An area of the body that minimizes melanin and maximizes capillary superficiality would provide the clearest images of blood cells across the most diverse group of individuals. With careful study, it is clear that the

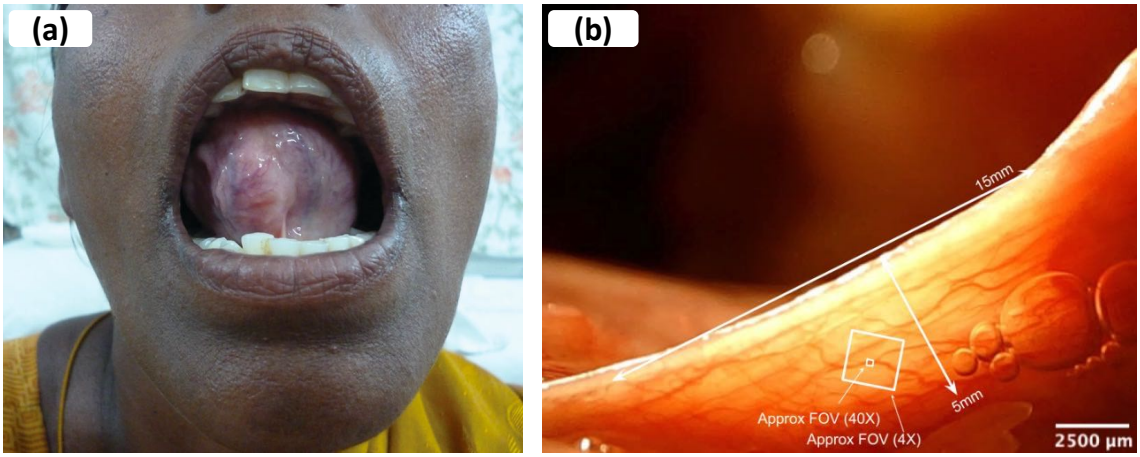

Figure 1-18. (a) Individuals with darker peripheral skin tones have lower melanin in their oral mucosa [37, 38], (b) the oral mucosa offers a rich bed of superficial capillaries.

oral mucosa offers an exciting opportunity. Even in individuals with darker skin tones, the oral mucosa is typically nearly devoid of melanin (Figure 1-18(a)) [37, 38]. Further, the epithelium of the oral mucosa is known to be thin and non-keratinized in many areas [193]. Previous imaging studies have shown that oral mucosa capillaries are often < 100 μm deep, with capillary loops documented as superficial as 50 μm from the tissue surface in areas such as the floor of the mouth [193–195]. Due to these critical advantages, oral mucosa capillary imaging offers a unique opportunity for resolving blood cells *in vivo*.

Phase contrast microscopy

Phase contrast imaging was first understood in the 1930's by Frits Zernike as a method of resolving transparent particles [196, 197]. While working with diffraction gratings, Zernike realized that the addition of an adequate reference beam overlayed on the wavefront of a weakly scattering phase object could greatly enhance its contrast. Zernike was awarded the Nobel Prize for his invention in 1953, and in hindsight, he humbly states about himself: "On looking back to this event, I am impressed by the great limitations of the human mind. How quick we are to learn - that is, to imitate what others have done or thought before - and how slow to understand - that is, to see the deeper connection. Slowest of all, however,

are we in inventing new connections or even in applying old ideas in a new field." Since its invention, phase contrast imaging has become ubiquitous in biological research. While certain techniques such as differential interference contrast and phase contrast microscopy are mature and readily available, phase contrast imaging is still a remarkably active area of research with new techniques in qualitative and quantitative phase imaging and optical tomography rapidly emerging [42, 46, 178, 198–200].

Phase contrast overview

Phase contrast is powerful in biological research due to its ability to image weakly scattering objects in a label-free manner. Optical phase is easiest to understand when considering the difference in optical path length portions of the same coherent, monochromatic planar wavefront can experience (Figure 1-19(a)). Optical phase (ϕ, (1.4)) quantifies the wavefront delay when a portion of a wavefront experiences an optical path length difference (OPD, (1.5)). Here λ is the wavelength, n is the index of refraction, and d is a physical distance. The goal of phase contrast imaging is to convert differences in ϕ into differences in the intensity recorded on a sensor ($I(x, y)$).

$$\phi = (2\pi/\lambda)OPD \tag{1.4}$$

$$OPD = (n_1 - n_0)d \tag{1.5}$$

Importantly, biological tissue is full of microscopic structures and compartments that have differences in index of refraction that can be exploited to generate contrast (Figure 1-19(b)). For example, while blood plasma has an index of refraction of around 1.35, the phospholipid bilayer that constitutes the plasma membranes has an index of around 1.4. Granules within white blood cells, along with mitochondria, have indices even higher than this [39–41]. Each of these structures also has a physical length. While the exact values of index of refraction

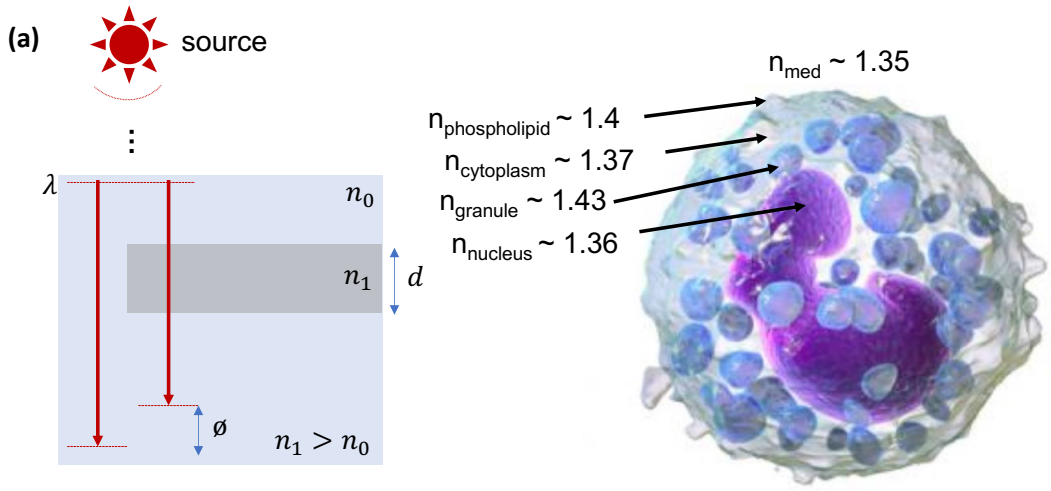

Figure 1-19. (a) Schematic showing a phase delay (ϕ) of a monochromatic, planar wavefront as a portion of it passes through a different index of refraction (n) over a physical distance (d). (b) Biological structures such as cells are full of intracellular components with difference in index of refraction. [39–41]

and physical dimensions change between cells, light experiences a complex array of optical path length difference when traversing even a single cell.

Phase contrast techniques

There are numerous optical methods that convert object phase differences to intensity differences in the resulting image (Figure 1-20). For example, in differential interference contrast (DIC) microscopy, an incident linearly polarized wavefront is sheared into orthogonal polarization states that are later recombined after passing through the object. The sheared wavefronts that pass through edges in the object experience a relative phase difference, and pass through an analyzer as elliptical polarization, while locations in the object with phase uniformity are attenuated by the same analyzer [43]. In conventional phase contrast microscopy (PCM), the sample is illuminated with radially symmetric, high angle oblique illumination that allows the separation of the reference beam from diffracted light, which occurs at all collection angles after interaction with the object. A phase delay imparted selectively to one these two wavefronts converts phase information into absorption-like contrast through interference [44]. A commercial microscope can be readily adapted to either of these

two techniques, making them some of the most common phase contrast imaging modalities.

Another, simpler form of phase contrast imaging called Differential Phase Contrast (DPC) was demonstrated in the 1980's and is still a source of inspiration for microscopy research today [42, 45]. In this technique, asymmetric illumination is used to create net oblique illumination across a sample (Figure 1-20(c)). Refraction by curved phase objects in the sample causes some light to refract towards the aperture of the system and appear brighter, while other portion to refract away from the entrance pupil and appear darker. By acquiring two, diametrically opposed illumination profiles (I_T and I_B), one can subtract and normalize the two images to produce a phase-only I_{DPC} image ((1.6)). Phase contrast generated using DPC-like illumination is the foundation of the microscopy technique investigated in this thesis.

$$I_{DPC} = \frac{I_T - I_B}{I_T + I_B} \tag{1.6}$$

Oblique back-illumination microscopy

Though the phase contrast techniques discussed previously are critical in biomedical research, they all work in transmission mode, where the light source and detector are on opposite sides of the object under study. For *in vivo* blood cell imaging, this poses a problem, as blood vessels are typically contained within a turbid, semi-infinite bulk medium that prevents transmission mode microscopy. In 2012, a new form of phase contrast microscopy called oblique back-illumination microscopy (OBM) was introduced that directly addressed this limitation [46]. OBM generates phase contrast using a similar approach to DPC, however instead of oblique transmission-mode illumination, OBM utilizes laterally offset epi-mode illumination that creates an oblique, virtual point source in tissue through multiple scattering (Figure 1-21). In OBM, an LED is coupled into a fiber source that is placed in contact with tissue at a lateral offset to the optical axis of the imaging system (Figure 1-21(a)). Through multiple scattering, some of the light will pass through the front focal plane of the microscope

objective, and, due to the initial lateral offset of the fiber source, the light has a net oblique angle (Figure 1-21(b)). The oblique illumination generates phase contrast in the image through the same mechanism as differential phase contrast imaging, where curved phase objects will refract light either towards or away from the aperture of the imaging system and thus convert changes in phase directly to changes in intensity (Figure 1-21(c)). Through the use of two, diametrically opposed fiber sources that are triggered sequentially, two images (I_L and I_R Figure 1-21(d)-(e)) can be acquired, which are directly analogous to I_B and I_T of DPC [42]. By adding and subtracting these two images, absorption-only (Figure 1-21(f)) and phase-only (Figure 1-21(g)) images can be acquired.

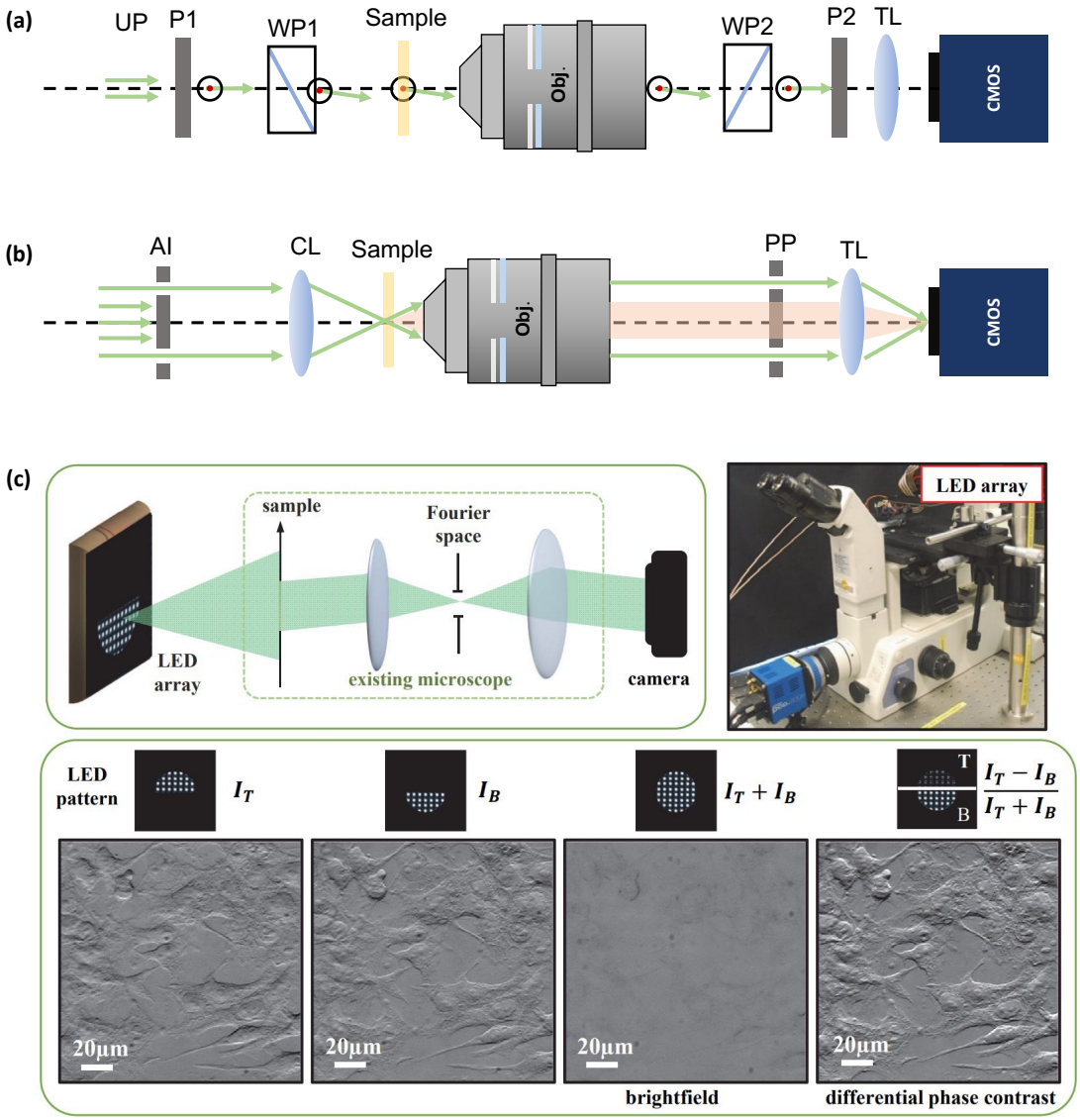

Figure 1-20. Conventional methods of phase contrast. (a) Schematic of differential interference contrast (DIC) microscopy. Unpolarized light (UP) passes through a linear polarizer (P1) at 45°. A Wollaston Prism (WP) shears the two orthogonal polarization states prior to passing through a sample. A second Wollaston prism recombined the sheared wavefronts after passing through the microscope objective. An analyzer (P2) blocks light that undergoes no phase delay between two sheared wavefronts, while edges of the object that do create relative phase differences pass as elliptically polarized light. (b) Phase contrast microscopy (PCM) utilizes an annular aperture (AA) and a condensing lens (CL) to illuminate a sample with circularly symmetric high angle light. Diffracted light from the sample (orange) emerges at all angles and a relative phase delay between the incident and diffracted fields is imparted by a phase plate (PP) after the objective. (c) Differential phase contrast utilizes diametrically opposed, sequentailly acquired oblique illumination (DPC). Refraction by phase objects in the sample bend light towards or away from the optical system converting phase differences into brightness [42–45].

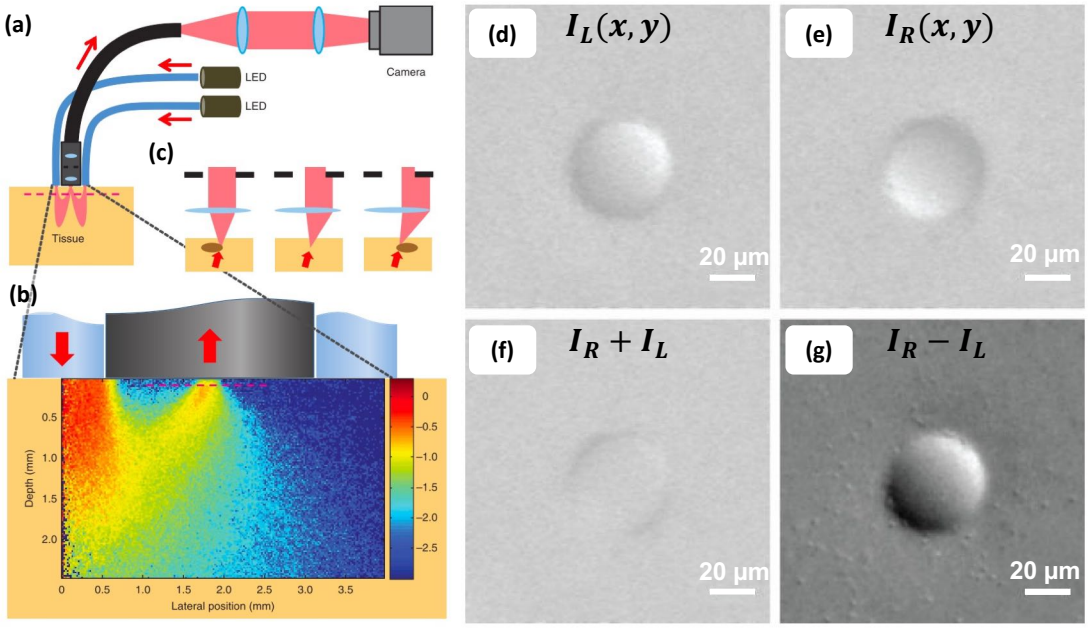

Figure 1-21. (a) Schematic of oblique back-illumination microscopy, (b) Monte Carlo simulation showing laterally offset epi-mode illumination from a fiber source producing net oblique back-scattered light through the imaging focal plane, (c) light refracted by phase objects will either bend towards the aperture of the system or away producing brighter and darker regions in the image dependent on phase [46].

In the last decade, numerous advances in OBM have been made. Simultaneous acquisition of the two diametrically opposed sources was shown with high frame rates using spectrally distinct sources, Wollaston prisms, and spectral filters [49]. Multifocus high-speed volumetric scanning was demonstrated with a z-splitter prism [201]. Quantitative oblique back-illumination microscopy has been demonstrated with four sources, sequential illumination, and inversion of the scattering process with a 3D optical transfer model [47, 178]. A mathematical model of OBM is required for inversion and recovery of quantitative phase information, and though this thesis only deals with qualitative phase contrast, it is instructive to outline regardless because the same principles of image formation apply.

A thin object, $o(\boldsymbol{x})$, can be described by a distribution of absorption and phase information via equation (1.7).

$$o(\boldsymbol{x}) = 1 - \mu(\boldsymbol{x}) + i\phi(\boldsymbol{x}) \tag{1.7}$$

Here $\boldsymbol{x}$ is a 2D spatial vector. The object is modified with an illumination profile with angular distribution of $E(\boldsymbol{u})$, creating a combined illumination and object electric field ($\psi_0(\boldsymbol{x})$), according to equation (1.8).

$$\psi_0(\boldsymbol{x}) = \mathcal{F}^{-1}\{E(\boldsymbol{u})\}o(\boldsymbol{x}) \tag{1.8}$$

The electric field can be propagated to the rear focal plane of the imaging objective ($\psi_1(\boldsymbol{f})$) where it is modified by the system pupil function, $P(\boldsymbol{f})$, according to equation (1.9).

$$\psi_1(\boldsymbol{f}) = P(\boldsymbol{f})\mathcal{F}\{\mathcal{F}^{-1}\{E(\boldsymbol{u})\}o(\boldsymbol{x})\} \tag{1.9}$$

And finally, through another 2D Fourier transform accomplished by the tube lens, the electric field is propagated to the imaging sensor $\psi_2(\boldsymbol{r})$, where its modulus square is detected as the image intensity ($I(\boldsymbol{r})$, equation (1.10)).

$$I(\boldsymbol{r}) = |\mathcal{F}\{P(\boldsymbol{f})\mathcal{F}\{\mathcal{F}^{-1}\{E(\boldsymbol{u})\}o(\boldsymbol{x})\}\}|^2 \tag{1.10}$$

With equation (1.10) in mind, it is clear that the illumination ($E(\boldsymbol{u})$) plays a critical role in the final observed image intensity $I(\boldsymbol{r})$. To further understand how illumination plays a role in the imaging system, the optical transfer function can be derived for the differential phase contrast approach in OBM. Note that these derivations can be found in more detail in references [47, 178]. First, equation (1.10) can be expanded into integral form as equation (1.11).

$$I(\boldsymbol{r}) = \Big| \iiint E(\boldsymbol{u})o(\boldsymbol{x})P(\boldsymbol{f})e^{-i2\pi \boldsymbol{u}\cdot\boldsymbol{x}}e^{i2\pi \boldsymbol{x}\cdot\boldsymbol{f}}e^{i2\pi \boldsymbol{f}\cdot\boldsymbol{r}}d^2\boldsymbol{u}d^2\boldsymbol{x}d^2\boldsymbol{f}\Big|^2 \tag{1.11}$$

Note that for an incoherent source like that used in OBM, $E(\boldsymbol{u})E^*(\boldsymbol{u}) = E^2(\boldsymbol{u})\delta(\boldsymbol{u}-\boldsymbol{u'})$, and $S(\boldsymbol{u}) = |E(\boldsymbol{u})|^2$, which can be substituted into (1.11) to produce equation (1.12).

$$I(\boldsymbol{r}) = \int S(\boldsymbol{u})\Big| \iint P(\boldsymbol{f})o(\boldsymbol{x})e^{i2\pi(\boldsymbol{f}-\boldsymbol{u})\cdot\boldsymbol{x}+\boldsymbol{f}\cdot\boldsymbol{r}}d^2\boldsymbol{x}d^2\boldsymbol{f}\Big|^2 d^2\boldsymbol{u} \tag{1.12}$$

Next, the Fourier transform of the object $\mathcal{F}(o(\boldsymbol{x})) = O(\boldsymbol{m})$ can be substituted into equation (1.12) along with a variable substitution $\boldsymbol{m} = \boldsymbol{f} - \boldsymbol{u}$ to reveal equation (1.13).

$$I(\boldsymbol{r}) = \int S(\boldsymbol{u})\Big| \iint P(\boldsymbol{m}+\boldsymbol{u})O(\boldsymbol{m})e^{i2\pi(\boldsymbol{m}+\boldsymbol{u})\cdot\boldsymbol{r}}d^2\boldsymbol{m}\Big|^2 d^2\boldsymbol{u} \tag{1.13}$$

Adding a new variable of integration $\boldsymbol{n}$ to accompany a substitution with the identity $|\int f(m)dm|^2 = \iint f(m)f^*(n)dmdn$, equation (1.14) arises.

$$I(\boldsymbol{r}) = \iint O(\boldsymbol{m})O^*(\boldsymbol{n})\Big[\int S(\boldsymbol{u})P(\boldsymbol{m}+\boldsymbol{u})P^*(\boldsymbol{n}+\boldsymbol{u})d^2\boldsymbol{u}\Big]e^{i2\pi(\boldsymbol{m}-\boldsymbol{n})\cdot\boldsymbol{r}}d^2\boldsymbol{m}d^2\boldsymbol{n} \tag{1.14}$$

Considering another variable substitution $\boldsymbol{q} = \boldsymbol{m} - \boldsymbol{n}$, which represents the Fourier space at the image plane, equation (1.14) can be reduced to equation (1.15).

$$I(\boldsymbol{r}) = \iint O(\boldsymbol{m})O^*(\boldsymbol{m}-\boldsymbol{q})C(\boldsymbol{m},\boldsymbol{m}-\boldsymbol{q})e^{i2\pi\boldsymbol{q}\cdot\boldsymbol{r}}d^2\boldsymbol{m}d^2\boldsymbol{r} \tag{1.15}$$

Where C represents the transfer function of the system,

$$C(\boldsymbol{m},\boldsymbol{n}) = \int S(\boldsymbol{u})P(\boldsymbol{m}+\boldsymbol{u})P^*(\boldsymbol{n}+\boldsymbol{u})d^2\boldsymbol{u} \tag{1.16}$$

Equation (1.15) can be expressed in Fourier image space as equation (1.17).

$$\tilde{I}(\boldsymbol{q}) = \int O(\boldsymbol{m})O^*(\boldsymbol{m}-\boldsymbol{q})C(\boldsymbol{m},\boldsymbol{m}-\boldsymbol{q})d^2\boldsymbol{m} \tag{1.17}$$

The object in Fourier space $O(\boldsymbol{m})$ can be approximated as a weakly scattering object that reduces to:

$$O(\boldsymbol{m})O^*(\boldsymbol{n}) \simeq \delta(\boldsymbol{m})\delta(\boldsymbol{n}) - [M(\boldsymbol{m})\delta(\boldsymbol{n}) + M^*(\boldsymbol{n})\delta(\boldsymbol{m})] + i[\Phi(\boldsymbol{m})\delta(\boldsymbol{n}) - \Phi^*(\boldsymbol{n})\delta(\boldsymbol{m})] \tag{1.18}$$

The approximation in equation (1.18) can be substituted into equation (1.17), and along with application of the sifting theorem to the delta functions, equation (1.19) results.

$$\tilde{I}(\boldsymbol{q}) = \delta(\boldsymbol{q})C(0,-\boldsymbol{q}) - [M(\boldsymbol{q})C(\boldsymbol{q},0) + M^*(-\boldsymbol{q})C(0,-\boldsymbol{q})] + i[\Phi(\boldsymbol{q})C(\boldsymbol{q},0) - \Phi^*(\boldsymbol{q})C(0,-\boldsymbol{q})] \tag{1.19}$$

Note that given equations (1.16) and (1.19), if $S(\boldsymbol{u})$ is even in both dimensions, $C(\boldsymbol{q},0) = C(0,-\boldsymbol{q})$, and if $S(\boldsymbol{u})$ is even in one dimension and odd in the other $C(\boldsymbol{q},0) = -C(0,-\boldsymbol{q})$. Further, considering the net even illumination produced by linear addition of two images produced by diametrically opposed illumination, and the net odd illumination produced by subtraction of images produced by diametrically opposed illuminations, it is possible to define two new system transfer functions for OBM.

$$C_\Delta(\boldsymbol{q}) = \int [S(\boldsymbol{u}) - S(\boldsymbol{u'})]P(\boldsymbol{u}+\boldsymbol{q})P^*(\boldsymbol{u})d^2\boldsymbol{u} \tag{1.20}$$

$$C_{\Sigma}(\boldsymbol{q}) = \int [S(\boldsymbol{u}) + S(\boldsymbol{u'})] P(\boldsymbol{u}+\boldsymbol{q}) P^{*}(\boldsymbol{u}) d^{2}\boldsymbol{u} \tag{1.21}$$

In equations (1.20) and (1.21), u' represents the coordinates at the back focal plane of the objective, inverted along the shear direction $u = [-u_1, u_2]$. Substituting the sum and difference transfer equations (1.20) and (1.21) into the image formation equation in Fourier space (1.19), two new equations emerge that describe the sum and difference image formation achieved with two diametrically opposed illuminations.

$$\tilde{I_{\Delta}}(\boldsymbol{q}) = C_{\Delta}(\boldsymbol{q})\delta(\boldsymbol{q}) - C_{\Delta}(\boldsymbol{q})[M(\boldsymbol{q}) - M^{*}(-\boldsymbol{q})] + i \cdot C_{\Delta}(\boldsymbol{q})[\Phi(\boldsymbol{q}) + \Phi^{*}(-\boldsymbol{q})] \tag{1.22}$$

$$\tilde{I_{\Sigma}}(\boldsymbol{q}) = C_{\Sigma}(\boldsymbol{q})\delta(\boldsymbol{q}) - C_{\Sigma}(\boldsymbol{q})[M(\boldsymbol{q}) + M^{*}(-\boldsymbol{q})] + i \cdot C_{\Sigma}(\boldsymbol{q})[\Phi(\boldsymbol{q}) - \Phi^{*}(-\boldsymbol{q})] \tag{1.23}$$

Using the assumption that the phase and absorption components ($\phi(\boldsymbol{r})$ and $\mu(\boldsymbol{r})$) are real-valued, and thus $\Phi(\boldsymbol{q}) = \Phi^{*}(-\boldsymbol{q})$ and $M(\boldsymbol{q}) = M^{*}(-\boldsymbol{q})$, and applying the inverse Fourier transform to equations (1.22) and (1.23) in order to retrieve the image in spatial coordinates, equations (1.22) and (1.23) simplify to:

$$I_{\Delta}(\boldsymbol{r}) = 2ic_{\delta}(\boldsymbol{r})\phi(\boldsymbol{r}) \tag{1.24}$$

$$I_{\Sigma}(\boldsymbol{r}) = 2C(0,0) - 2c_{\sigma}(\boldsymbol{r})\mu(\boldsymbol{r}) \tag{1.25}$$

Here $C(0,0)$ represents $\int S(\boldsymbol{u})P(\boldsymbol{u})P^{*}(\boldsymbol{u})d^{2}\boldsymbol{u}$, the DC background term, and c_{δ} and c_{σ} represent the system point spread funtion with difference and summation of the two diametrically opposed illuminations, respectively. Lastly, in order to normalize the above phase-only terms to correspond with the DPC intensity equation (1.6), $I_{\Delta}(\boldsymbol{r})$ is divided by $2C(0,0)$ to give equation (1.26)

$$I_{DPC}(\boldsymbol{r}) = \frac{ic_{\delta}(\boldsymbol{r})\phi(\boldsymbol{r})}{C(0,0)} \tag{1.26}$$

Lastly $I_{DPC}(\boldsymbol{r})$ can be written as a convolution with the DPC point spread function $C_{DPC}(\boldsymbol{r})$ as:

$$I_{DPC}(\boldsymbol{r}) = C_{DPC}(\boldsymbol{r}) * \phi(\boldsymbol{r}) \tag{1.27}$$

Where the DPC transfer function is:

$$C_{DPC}(\boldsymbol{r}) = \frac{-i\int[S(\boldsymbol{u}) - S(\boldsymbol{u'})]P(\boldsymbol{u}+\boldsymbol{q})P^{*}(\boldsymbol{u})d^{2}\boldsymbol{u}}{\int[S(\boldsymbol{u})]P(\boldsymbol{u})P^{*}(\boldsymbol{u})d^{2}\boldsymbol{u}} \tag{1.28}$$

Note that C_{DPC} described in equation (1.25) represents the combined optical system transfer function for OBM after images with two diametrically opposed illuminations (odd in one axis, even in the other) are subtracted from one another. It is visualized in Figure 1-22(e). Interestingly, subtraction of the two images eliminates the DC term as well as the absorption term (provided both illuminations are spectrally close), shown in (1.25), which yields a form of optical sectioning. Lastly, it is helpul to consider that equation (1.14) is the same mathematical description of image formation in a transmission microscope with incoherent illumination [47, 202, 203]. Though OBM utlilizes epi-mode illumination, the multiply scattered light passes back through the objective focal plane as if it came from within the tissue. Thus, OBM enables measurement of the forward scattered field without necessitating transmission illumination. This represents an important distinction between OBM and other non-phase contrast imaging techniques such as reflectance and spectrally-encoded confocal microscopy [195, 204–208] that can resolve blood cells *in vivo*. These other imaging modalities sample back-scattered light from tissue, which contains information primarily about the smallest of sub-cellular structures, and misses important forward-scattered information like bulk cellular morphology and nuclear shape that have weak changes in refractive index [47, 177, 178].

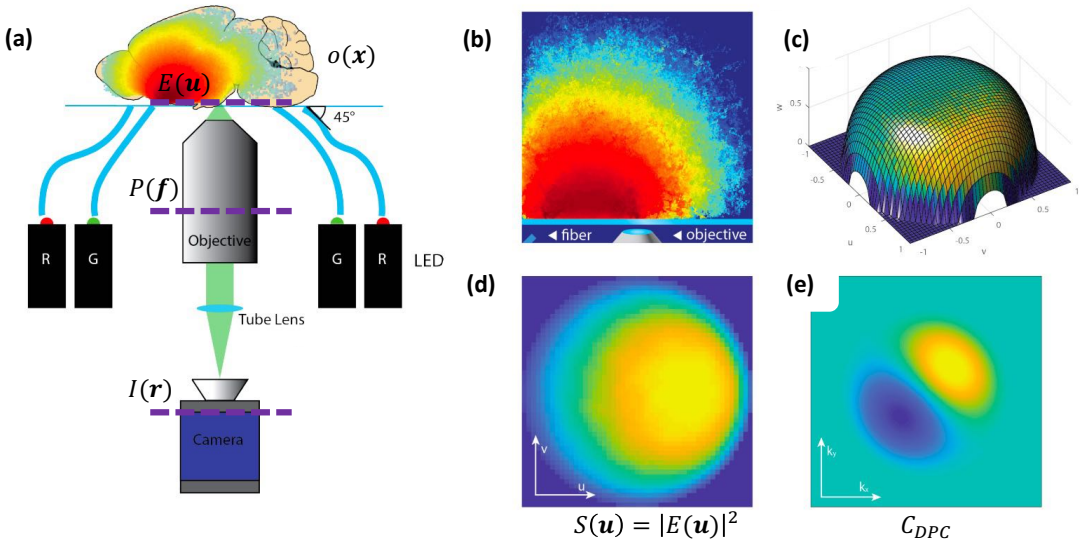

Figure 1-22. (a) Four-source OBM system schematic showing the object $o(\boldsymbol{x})$, the illumination $E(\boldsymbol{u})$, the pupil function $P(\boldsymbol{f})$, and the resulting image $I(\boldsymbol{r})$. (b)-(d) Monte Carlo simulations showing net oblique illumination in spatial and angular space. (e) Resulting OBM transfer function after subtraction of diametrically opposed illumination [47].

The ability of OBM to detect forward scattered light and phase information in bulk tissue makes it a promising technology for *in vivo* blood cell imaging. However, it has fundamental and important limitations that must be considered. First, OBM phase contrast is degraded by multiple scattering, and the technique can can only produce phase contrast in regions of tissue approximately one mean free path in depth. Data supporting this is shown in Figure 1-23. In skin imaging, phase contrast degraded rapidly by a depth of 80 μm. Thus, OBM will only work for *in vivo* blood cell imaging in the superficial capillaries of the oral mucosa, but not those in the nailfold. Second, the use of external fiber sources in OBM creates limitations. Their physical size and necessary housing generate a larger form-factor than if only the microscope objective needed to be in contact with the sample. This is especially problematic when high NA, high magnification objectives are required, which typically have a larger housing. Any additional bulk is prohibitive since the technique must be adapted to imaging deep recesses of the oral mucosa like the floor of the mouth, the inner lip, or the ventral tongue to reach superficial capillaries. Finally, the seminal paper in OBM shows that

the obliquity of the light tends to increase the smaller the source-detector separation becomes (Figure 1-24). However, for a given imaging objective size, there is a fundamental limit on how close the fiber can be placed to the optic axis due to steric hindrance. For example, a standard microscope objective may have 9 mm wide diameter at its frontmost optical element. The minimum achievable source-detector separation in this case is approximately 5 mm (assuming 1 mm diameter fiber Figure 1-24(c)), which according to simulations in Figure 1-24 is not nearly achieving an optimal source obliquity. A method that obviates the external fiber sources but still enables an offset illumination could reduce the source-detector separation into a critical range where source obliquity is maximized $\simeq 250$ μm according to Figure 1-24(a).

Given the limitation on the minimum achievable δx with a high power objective, and the external fiber illumination used in oblique back-illumination microscopy, an alternative geometry is desirable. If there were a way to illuminate the sample with a focused area of light offset from the optic axis only a few hundred microns while still in epi-illumination, optimized source-detector separation could be achieved without reducing the system numerical aperture. Importantly, a clue as to how to achieve this comes from fundamental microscopy illumination principles [50]. Most brightfield microscopes operate with Kohler illumination (Figure 1-22(a)), where the physical illumination source is defocused from the sample under study via the illumination optics. This creates uniform illumination across the field of view, where the structural details of the physical source are non-conjugate with the sample under study. This illumination approach is typically preferable. On older, less refined illumination technique, called critical illumination (Figure 1-22(b)) instead creates an illumination geometry where the source is conjugate to the sample plane. This can create non-uniform illumination, as the finite source with its own structural details are imaged on top of the object. While this can create artifacts that are often undesirable, the use of critical illumination is at the heart of the microscopy technique presented in the following chapters. Importantly, when the source is conjugate with the sample, lateral spatial offsets of the source generate conjugate

displacements of the image of the source in object space. Thus, physical displacement of the source with critical illumination can produce the source-detector separation necessary of oblique back-illumination.

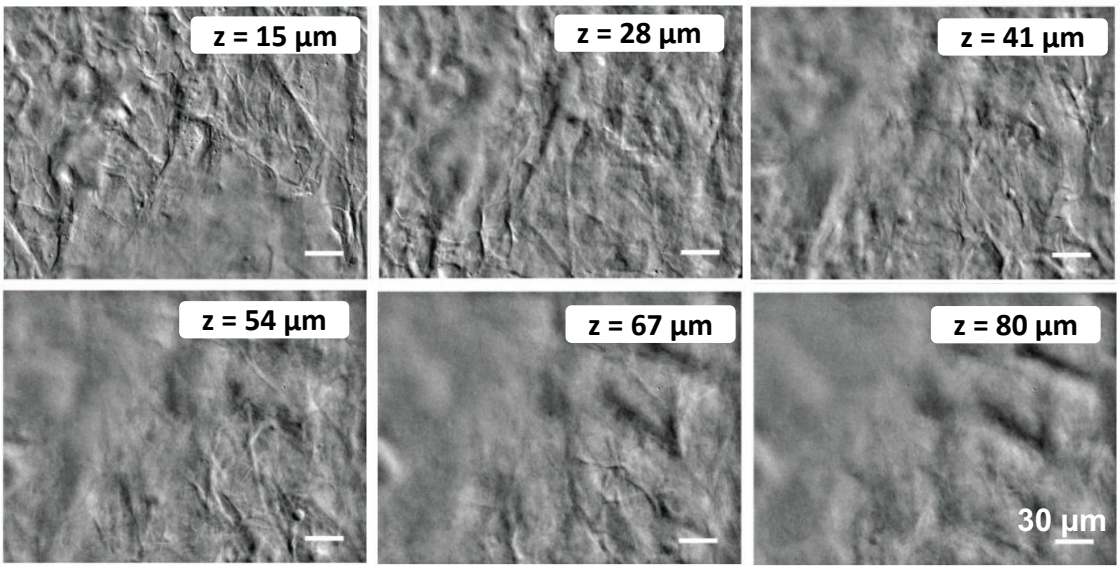

Figure 1-23. OBM phase contrast degrades with tissue depth (z) [48].

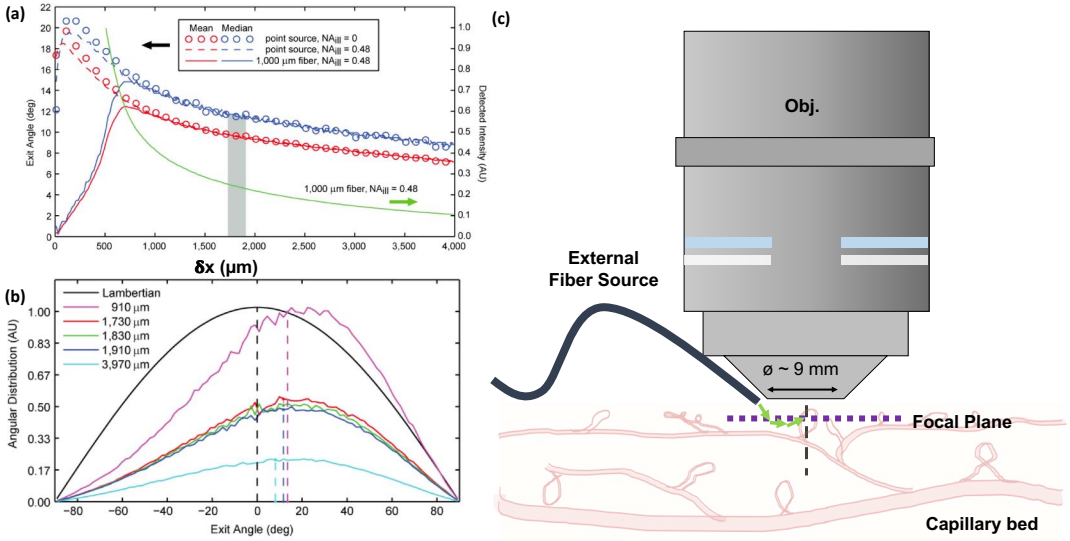

Figure 1-24. (a) Exit angle vs. fiber probe separation, and (b) angular distribution vs. exit angle together demonstrate increased obliquity with decreased source-detector separation (δx) [49]. (c) Schematic showing how the use of an external fiber source with a high power microscope objective limits the minimum source-detector separation due to steric hindrance.

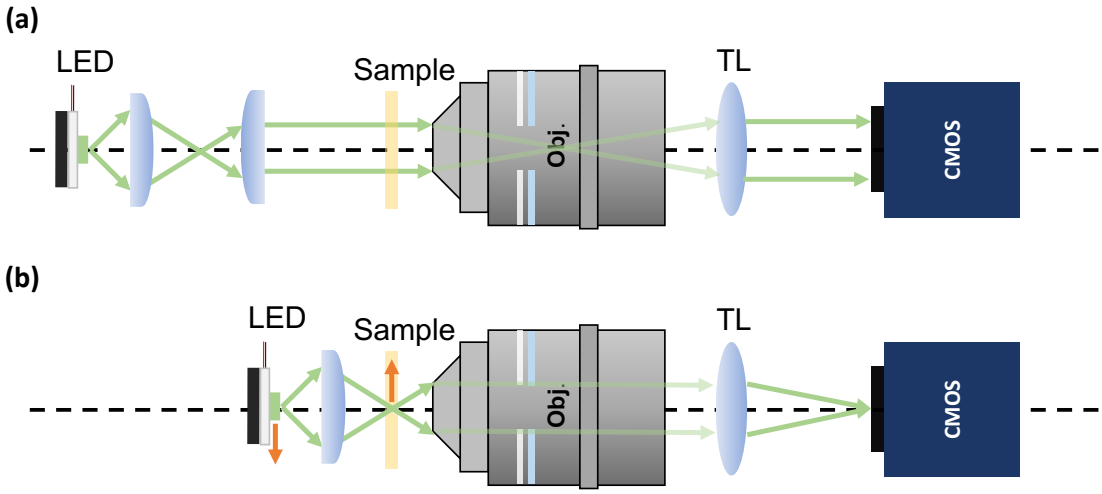

Figure 1-25. (a) Kohler illumination uses a defocused source at the specimen plane, conjugating the illumination source with the back focal plane of the objective to enable uniform illumination and avoid imparting structural details of the source onto the object. (b) Critical illumination creates a conjugate plane between the illumination source and the sample, creating non-uniform illumination. Note that because the source and sample are conjugate, a lateral offset of the physical source yields a lateral offset of the source in object-space (orange arrow) [50].

Chapter 2

Oblique back-illumination capillaroscopy for epi-illumination combined phase and absorption contrast.

Introduction

Oblique back-illumination microscopy (OBM) is a promising form of phase contrast microscopy for resolving transparent objects such as platelets and white blood cells *in vivo* in humans in a label-free manner. A phase contrast technique such as this should enable the resolution of red and white blood cells in bulk tissue, which would enabling distinguishing between cellular and acellular optical absorption gaps, yielding improved non-invasive measurements of neutropenia. Further, if the technique has sensitivity to sub-cellular components such as nuclei and granules, it may also enable a non-invasive complete blood cell count with white blood cell differential. However, as noted in the introduction, the obliquity of light, which generates phase contrast in OBM, is limited by the large source-detector axis separations necessitated by the external fiber sources used in OBM (Figure 1-24). This limitation is addressed here, by a new form of imaging called oblique back-illumination capillaroscopy (OBC). OBC generates combined phase and absorption contrast to blood cells in epi-mode similar to OBM, but enables closer source-detector axis separation by obviating the external fiber sources previously

used. Instead, OBC generates phase contrast through an LED source being critically imaged and de-magnified directly through the imaging objective. The conjugate relationship between LED source and objective focal plane enables a source-detector offset through simple lateral translation of the LED illumination or the imaging sensor. The offset, critically imaged source produces oblique, back-scattered light passing through the focal plane analogous to the illumination in OBM. Importantly, because the LED is being imaged through the objective, small source-detector separations can be achieved on the order of hundreds of microns, rather than the millimeter source-detector separations achievable with external fiber sources of OBM. Note, according to simulations plotted in Figure 1-24, the highest obliquity light is achieved when the source-detector separation is in the range achievable with OBC, but not with OBM. This simple yet fundamental difference has profound implications on the image quality achieved when compared to its predecessor. This chapter will outline and explain a single-source, benchtop OBC system that achieves phase contrast in phantom data. It will then introduce a dual-source OBC system that uses diametrically opposed, spectrally distinct LED sources that are separately by a dichroic mirror and simultaneously imaged onto two synchronized sensors. Both of the two systems are capable of the high speed imaging required for future *in vivo* blood cell imaging.

Materials and Methods

Optical System: single-source OBC

Figure 2-1 shows a schematic of the OBC optical system. In this setup, an LED (Superbright 1W XLamp LED, 88 lm, 527 nm), is placed at the rear focal plane of an $f = 20mm$ collimating lens (CL, Thorlabs ACL2520U-A). This lens collimates the light and enables a reverse pass through the infinity corrected microscope objective (Nikon 1.15 NA APO LWD WI λS). Optionally, a pinhole (PH, Thorlabs, SM1D12 $\phi = 0.8$ - 12 mm) can be placed at the emitting surface of the LED control the spatial coherence of the illumination. The microscope objective in combination with the collimating lens creates an image of the LED in the capillary bed,

which creates a critical illumination geometry where the emitting source and sample are conjugate. Together, the collimating lens and the microscope objective can be thought of as a 4F system with the LED and capillary bed at conjugate planes. When light from the critically imaged LED hits tissue, it undergoes multiple scattering dependent on the optical properties of the tissue. Analogous to Monte Carlo simulations in OBM (Figures 1-21 and 1-22), laterally offset epi-illumination will produce oblique back-scattered light through the focal plane. This back-scattered light is collected by a forward pass through the microscope objective, and relayed through an $f = 200mm$ tube lens (Thorlabs AC254-200-A-ML) by a 50:50 non-polarizing beamsplitter (Thorlabs (CCM1-BS013) to create an image on the sCMOS (pco.edge sCMOS 5.5). The microscope objective and the tube lens operate as a second 4F system with the capillary bed and the sCMOS sensor at conjugate planes. Thus the OBC system is effectively two 4F systems sharing a common focal plane in the sample and separated by the beamsplitter. In this geometry, the illumination plane, the object plane, and the image sensor plane are all conjugate, and a lateral displacement in one produces a lateral displacement in the others, with a magnification difference determined by their focal lengths. For example, as depicted in Figure 2-1(a), a lateral displacement of the imaging sensor $\delta x'$ produces an offset of the image of the LED in object space and the field of view in object space of (δx). The magnification is set by the ratio of the focal lengths of the imaging objective and the tube lens, which in this case is equal to $f_{TL}/f_M = 200mm/5mm$, and thus: $\delta x = \delta x'/40$. Figures 2-1(c) and its corresponding intensity plot profile (d) shows the gradient of illumination produced by this source-detector offset with a gaussian blurred image of a scattering phantom. From this data, it is clear that the LED is imaged to the left of the sensor axis, creating the source-detector separation δx. This single source OBC system achieves oblique back-scattered light that creates contrast to phase objects due to refraction towards or away from the aperture of the system, just as in DPC and OBM. The use of an LED in the green portion of the visible spectrum creates illumination that is also efficiently absorbed by hemoglobin (Figure 1-4), and thus the single-source OBC system can provide

phase contrast to otherwise transparent particles such as white blood cells and platelets, and combined phase and absorption contrast to red blood cells.

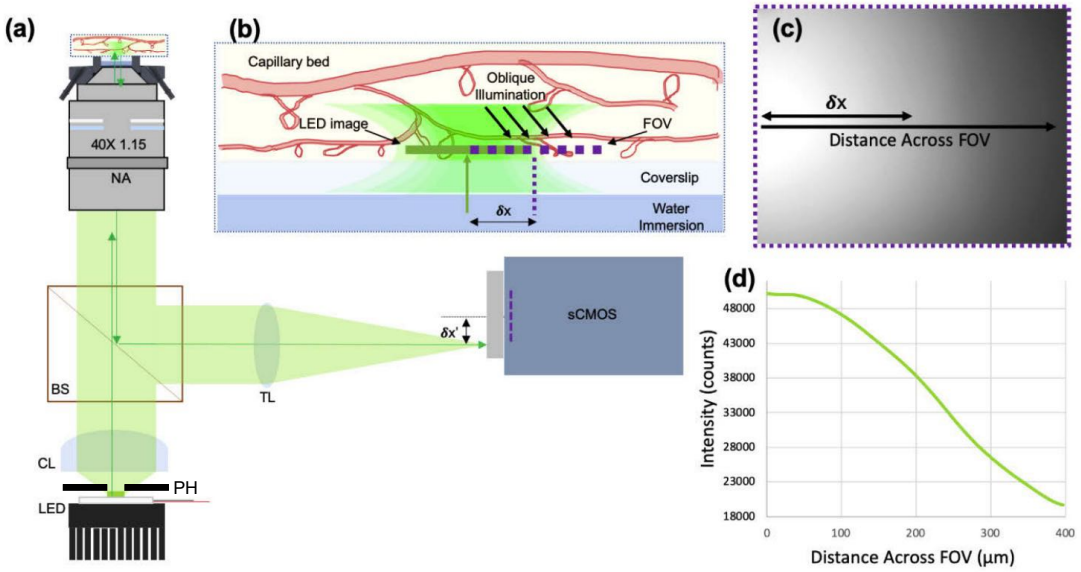

Figure 2-1. (a) Oblique back-illumination capillaroscope optical layout. An LED source with adjacent pinhole (PH, optional) is placed at the rear focal plane of a collimating lens (CL), which is critically imaged into a bulk scattering sample (such as a capillary bed) by a reverse pass through a 40X, 1.15 NA microscope objective. Back-scattered light is collected by the microscope objective, reflected off a beamsplitter (BS), and imaged onto a laterally offset sCMOS by a tube lens (TL). (b) Enlarged view of the capillary bed showing that the imaging field of view is laterally offset from the critically imaged LED illumination, producing net oblique illumination. The lateral offset in capillary-space is shown as variable δx. (c) A gaussian blurred image from a scattering phantom showing the gradient of illumination across the field of view, (d). [51]

Optical System: dual-source OBC

The single-source OBC system outlined in Figure 2-1 demonstrates that a close source-detector separation without external fiber sources can be achieved through critical imaging of an LED source into tissue. While this enables combined phase and absorption contrast, it is often helpful with techniques such as DPC and OBM to have two diametrically opposed illumination sources. This dual source illumination scheme enables two opposing views of phase objects, which can produce the $I_{DPC}(\boldsymbol{r})$ image when subtracted (equation (1.26) and Figure 1-21(g)). Previously, with OBM, this was achieved with sequential illumination and

detection, which ultimately reduced the frame rate of the system by half to 17.5 Hz [48]. The second iteration of OBM sought to increase imaging speed by using two spectrally distinct sources that were separated in imaging space using a Wollaston prism and filters. Imaging these two signals onto the same sensor simultaneously enabled higher frame rate imaging (44.5 Hz), though at a detriment to field of view since both signals were imaged onto the same sensor [49]. However, neither of these speeds are fast enough to image blood cell *in vivo* in humans. To enable high speed, simultaneous, large field of view, dual-channel imaging, a new OBC optical system is proposed, shown in Figure 2-2.

This method utilizes an LED board with two spectrally distinct LEDs symmetrically and laterally displaced from the optic axis. They are set by the manufacturer to be separated by approximately 600 μm. Again, similar to the single-source OBC system, the LED board can be placed at back focal plane of a collimating lens and critically imaged by a reverse pass through an infinity-corrected microscope objective. In this system, a collimating lens (CL) with a focal length of $f = 12$mm was paired with a microscope objective with a focal length of $f = 10$mm such that the lateral displacement from the optic axis to each LED image in object space is maintained at around $\delta x = 250\mu m$. A microscope objective with 20X magnification and 0.75 NA was chosen to enable larger field of view imaging. Again, a 50:50 beamsplitter collects back-scattered light, but now images it onto two CMOS sensors (The Imaging Source DMK 33UX252) separated by a dichroic mirror (Thorlabs DMLP605) with the same tube lens as before. The two CMOS sensors are each capable of 120 fps with a 350 μm x 265 μm field of view in object space. They are synchronized via a hardware trigger, controlled by an Arduino Uno connected to a 12-pin Hirose cable (Figure 2-3). The two LEDs have center wavelengths of 530nm and 640nm, which have minimal spectral overlap and can be efficiently separated by the dichroic. The 530nm green channel is efficiently absorbed by hemoglobin, providing a combined phase and absorption contrast image similar to the single-source OBC system shown previously, while the 640nm red channel demonstrates primarily only phase information from the opposite direction. This channel enables deeper imaging due to reduced

tissue scattering at longer wavelengths. Importantly, the two wavelengths are not spectrally close, and the objects such as blood cells under study do not have similar absorption across the two sources. If the images were added or subtracted then, it would no longer produce a purely absorption-only or phase-only image respectively as outlined in DPC and OBM. However, since the end goal of the project is to optimize for cell classification and tracking, the use of these two wavelengths will provide more information to computer vision algorithms than a single source system, or even a dual-source with spectrally close wavelengths.

The use of two Imaging Source DMK 33UX252 sensors in the dual-channel OBC system instead of using two pco.edge sCMOS sensors used in the single-source system is driven by cost, data, and weight. The Imaging Source DMK 33UX252 sensors provide high speed imaging for approximately 15X lower cost than the pco.edge sensor with simple USB 3.0 connectivity. The DMK 33UX252 sensors also much smaller and weigh only 65 g, while the pco.edge 5.5 sCMOS weighs around 1 kg, which is important for the portable dual-source system discussed in Chapter 4. However, these advantages come at the cost of significantly reduced field of view, which is highlighted in (Figure 2-4(c)). Importantly, for the 20X 0.75 NA objective chosen, the diffraction-limited resolution for 640nm illumination is around 521nm, which should be sufficient for resolving platelets, nuclei, and even some sub-cellular granules. Additionally, the 3.45 μm pixel pitch of the DMK 33UX252 sensor is adequately sampled with the 20X objective at 172.5 nm pitch in object space. Thus, the single source system has a higher NA objective and a more sensitive camera, and is likely to produce the highest quality OBC data. However, the sleeker, dual-source OBC system should provide sufficient resolution, field-of-view, and imaging speed as well as a more robust and practical system for acquiring data in human oral mucosa.

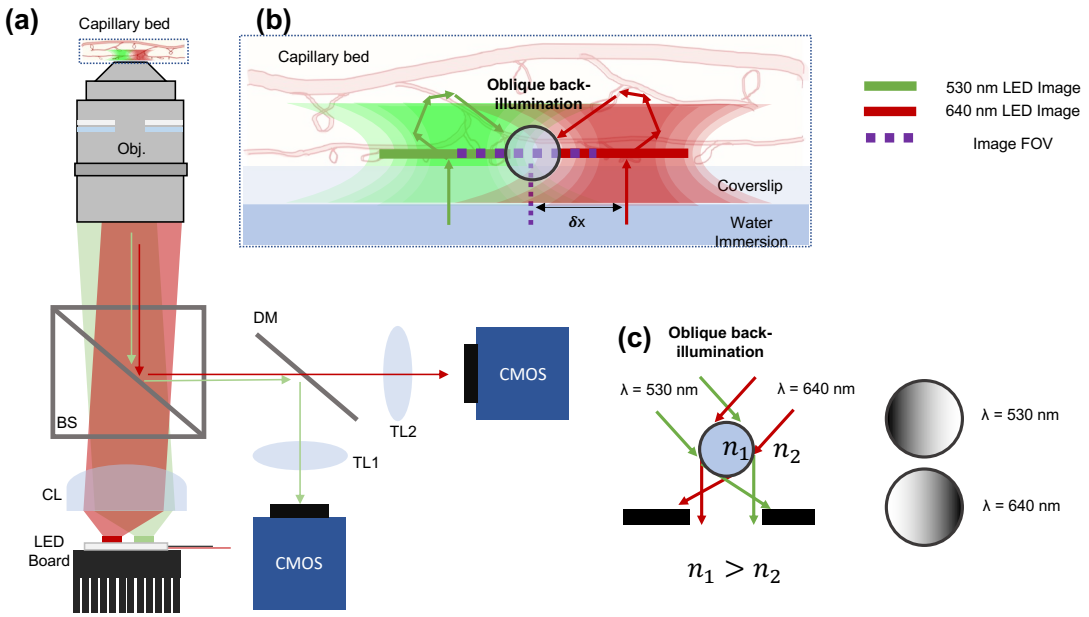

Figure 2-2. (a) A dual channel OBC system for high-speed, large FOV imaging. An LED board containing laterally offset 530nm and 640nm LEDs are collimated by a lens (CL), and imaged into tissue on opposing sides of a phase object. Back-scattered light is reflected off a beamsplitter (BS), and imaged onto two CMOS sensors by tube lenses (TL). A dichroic mirror (DM) is used to separate the two wavelengths. (b) Enlarged schematic of a capillary bed showing laterally offset, critically imaged LEDs and diametrically opposed, net oblique back-illumination. (c) Schematic of refraction by a phase particle under oblique back-illumination towards or away from the aperture of the system producing phase contrast.

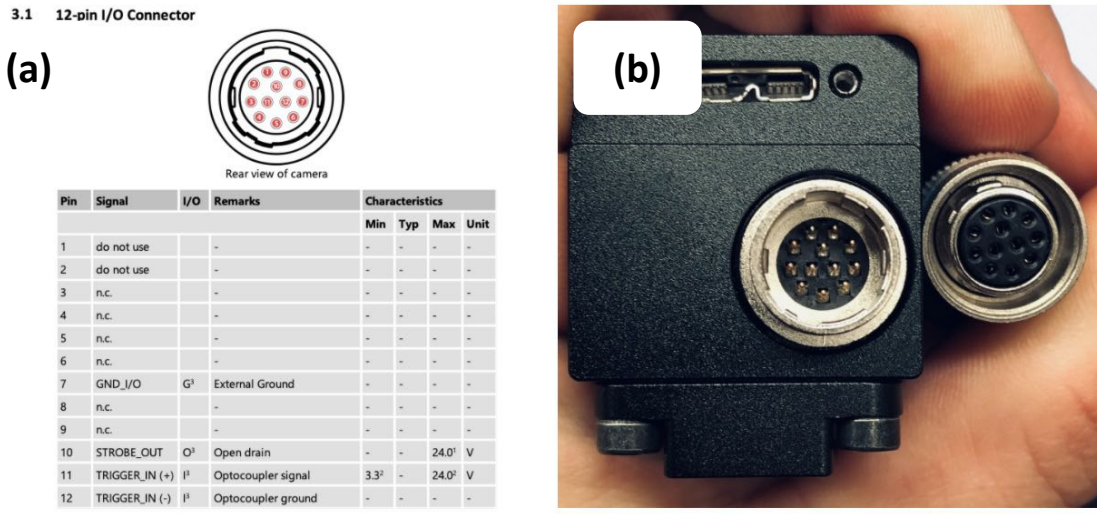

Pin	Signal	I/O	Remarks	Characteristics			
				Min	Typ	Max	Unit
1	do not use		-	-	-	-	-
2	do not use		-	-	-	-	-
3	n.c.		-	-	-	-	-
4	n.c.		-	-	-	-	-
5	n.c.		-	-	-	-	-
6	n.c.		-	-	-	-	-
7	GND_I/O	G[3]	External Ground	-	-	-	-
8	n.c.		-	-	-	-	-
9	n.c.		-	-	-	-	-
10	STROBE_OUT	O[3]	Open drain	-	-	24.0[1]	V
11	TRIGGER_IN (+)	I[3]	Optocoupler signal	3.3[2]	-	24.0[2]	V
12	TRIGGER_IN (-)	I[3]	Optocoupler ground	-	-	-	-

Figure 2-3. (a) 12-pin IO diagram for hardware trigger control of DMK 33UX252 used in the dual-source OBC system, (b) rear of camera with 12-pin hirose connector cable. Note that the parity of the hirose cable is flipped when connected to the sensor.

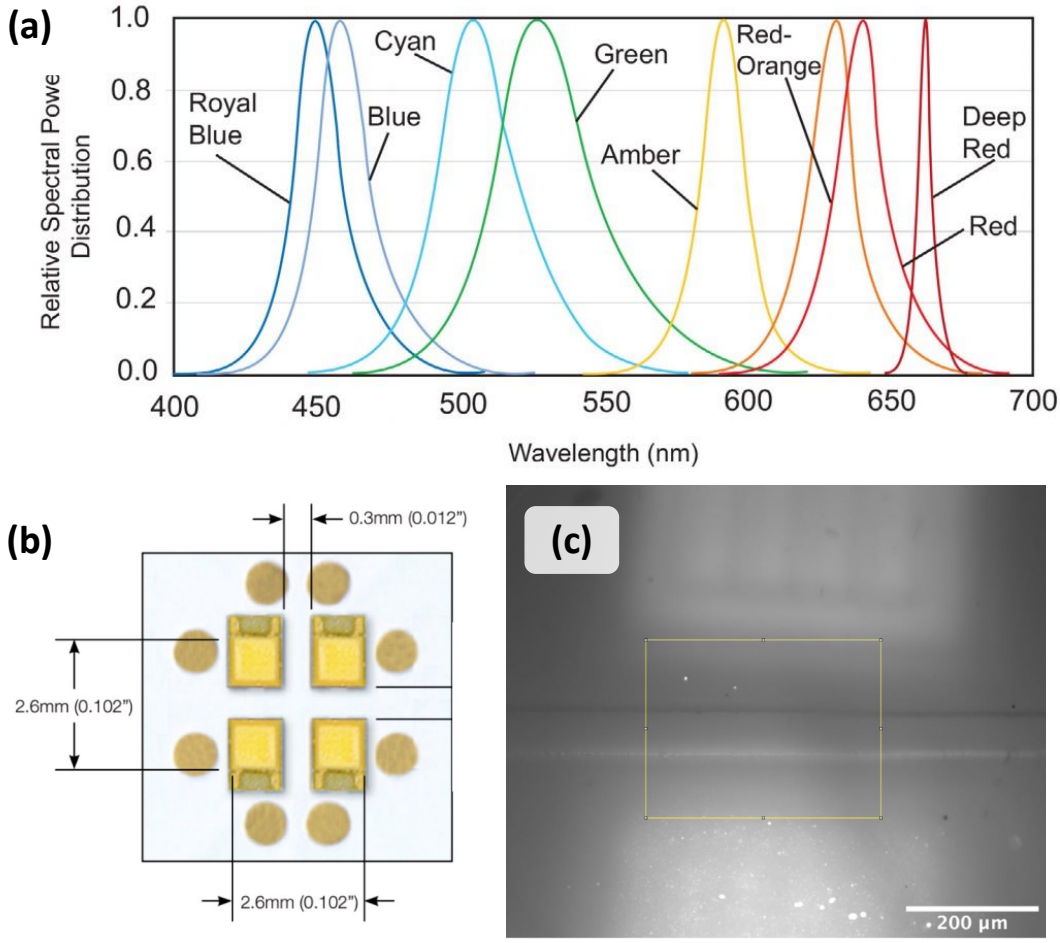

Figure 2-4. (a) Emission spectra of Luxeon star LEDs, with Green and Red wavelengths utilized in the dual-channel OBC system showing minimal spectral overlap. (b) A schematic of the LED board utilized in the OBC system. (c) Wide field of view captured with the pco.edge sCMOS with a single LED source on and the approximate field of view with the DMK 33UX252 sensor highlighted in the yellow box with the 20X objective. Note the optimized source-detector axis separation of approximately $\delta x = 250\mu m$.

Phase contrast phantom preparation

To demonstrate the phase contrast ability of the OBC system in a controlled sample, a phase-only phantom was created with a mixture of lipid and protein particles in an agar medium. This was achieved by mixing coffee creamer into a 1 % aqueous agar solution (10:90, v:v). The sample was poured into a 12-well culture dish and allowed to cure at 4 °C overnight before being removed and placed on a coverslip for imaging. The combination of the lipid particles in a mostly aqueous medium creates phase-only particles that can be

imaged in the OBC system with similar index of refraction to blood cells in aqueous blood plasma. One such particle approximately 6 μm in diameter, was imaged while the LED was laterally translated and the sensor was aligned on-axis. The Weber contrast was measured at each LED location by measuring the lateral intensity profile across the phase particle along the direction of LED motion. Additionally, images were taken at two diametrically opposed positions where phase contrast was optimized ($\delta = \pm 240\mu$m), and either summed or subtracted, respectively, to create the characteristic absorption-enhanced and phase-enhanced images analogous of oblique back-illumination microscopy. The results of this experiment are highlighted in Figure 2-5.

Pinhole Experiments

To test the impact of the spatial coherence of the illumination source on phase contrast, a pinhole with variable aperture (ϕ = 0.8 - 12 mm) can be placed directly above the emitting surface of the LED. With the LED imaged on-axis and the sensor also centered on-axis, the size of the pinhole can be varied to change the size of the critically imaged source in the sample. For this experiment, the extremes of ϕ = 12 mm and ϕ = 0.8 mm were tested by imaging approximately 20 μm deep in a sheet of paper. The results of this experiment are shown in Figure 2-6.

Flat-field correction

A flatfield correction algorithm was applied to the acquired images to correct for the intensity gradient across the field of view (Figure 2-1(c)) similar to [48, 49]. This was accomplished by dividing each image by a blurred version of itself. The blurred image was obtained by convolving with a Gaussian kernel with an 80-pixel standard deviation, which corresponds to 13 μm in object space.

Results

OBC generates phase contrast using net oblique back-scattered light similar to OBM. To demonstrate analogous illumination and optimize the phase contrast, lipid particles in an agar phantom were imaged (Figure 2-5). To optimize the phase contrast of the system, the image contrast of the lipid particle was measured as the LED was laterally translated, shown in Figure 2-5(b)-(d). In this experiment there is a clear optimization of phase contrast with a lateral displacement in object space of $\delta x = 240\mu$m, with contrast minima occurring with the LED centered on axis ($\delta x = 0\mu$m), and with the LED displaced $\delta x = 325\mu$m (the maximum measured). Images of the phase particle at $\delta x = 0\mu$m and $\delta x = 240\mu$m are shown in Figure 2-5(c)-(d), respectively.

Knowing phase contrast was optimized at $\delta x = 240\mu$m, the LED was displaced this magnitude on either side of the phase particle, upon which two images were taken *Figure 2-5(e)-(f)). These two images, labeled $I_L(x, y)$ and $I_R(x, y)$ are directly analogous to the diametrically opposed illumination images from OBM shown in Figure 1-21(d)-(e), and from DPC shown in Figure 1-20(c). Similar to OBM and DPC techniques, these two images can be added to create a brightfield, absorption-only image (Figure 2-5(g)), and subtracted to create a phase-only image (Figure 2-5(h)).

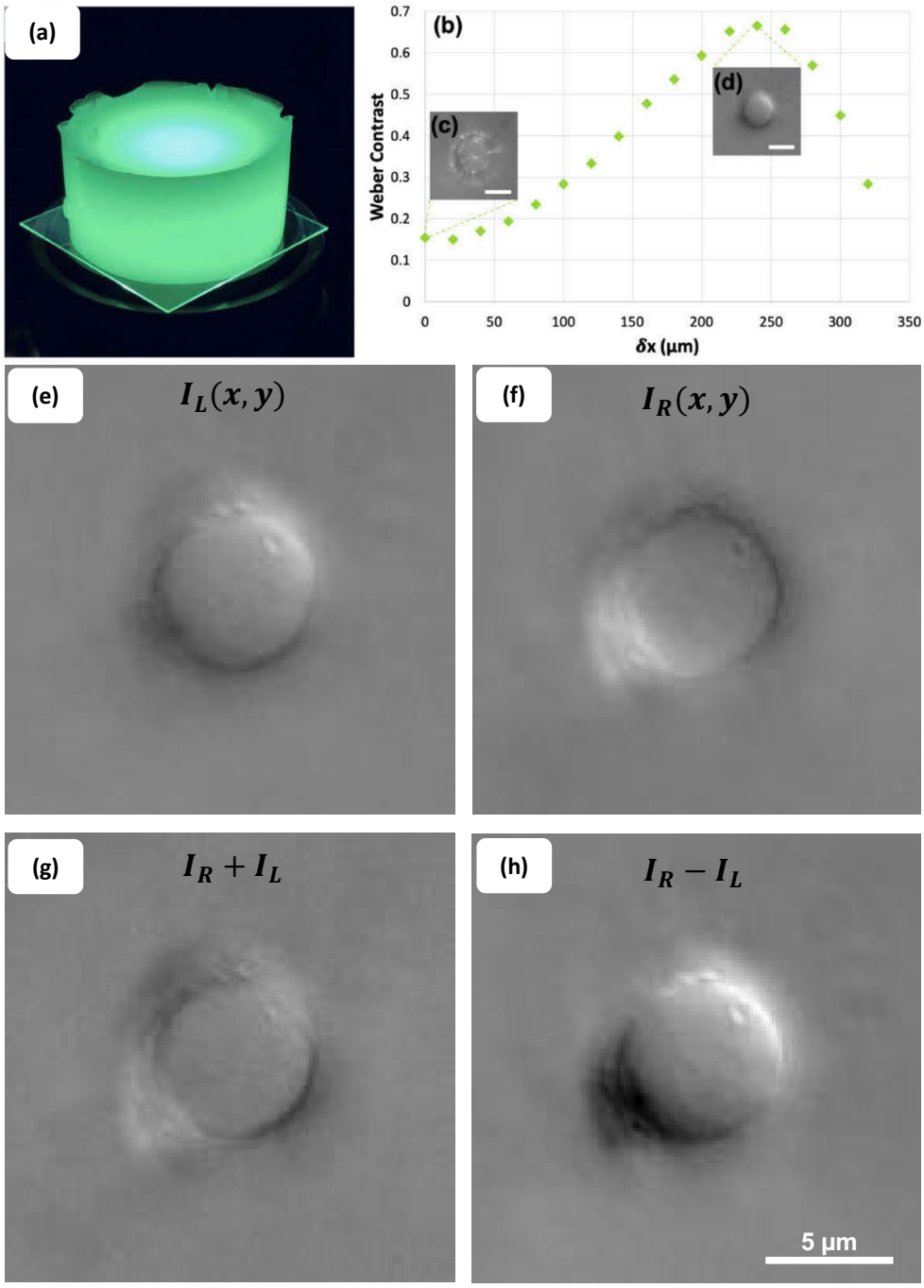

Figure 2-5. (a) Phase-only coffee creamer in agar phantom being imaged on a coverslip. (b) Phase contrast measurements vs. source-detector offset shows a peak around $\delta x = 240\mu$m. (c)-(d) Representative images of a 6 μm diameter lipid particle taken at $\delta x = 0\mu$m and $\delta x = 240\mu$m, respectively. (e)-(f) images of the same lipid particle with $\delta x = \pm 240\mu$m (diametrically opposed illumination). (g) Absorption only, summed brightfield image, and (h) phase-only, subtraction phase contrast image [51].

An additional insightful experiment is shown in Figure 2-6, where a piece of paper is imaged in the OBC system with varying pinhole size at the LED emitting surface. Importantly, in this case, both the LED and the sCMOS sensor are centered on-axis ($\delta x = 0\mu$m). Figure 2-6(a) shows a flat-field corrected image of the paper with the pinhole at 12 mm diameter, while Figure 2-6(b) shows an image of same location of the paper with the pinhole diameter set to 0.8 mm diameter. The phase contrast is markedly improved with the smaller pinhole diameter over the field of view shown. Additionally, there circularly symmetric pattern of phase contrast emanating outward from the center where the LED is imaged. In this case, the radial direction from the optic axis corresponds to the source-detector separation δx.

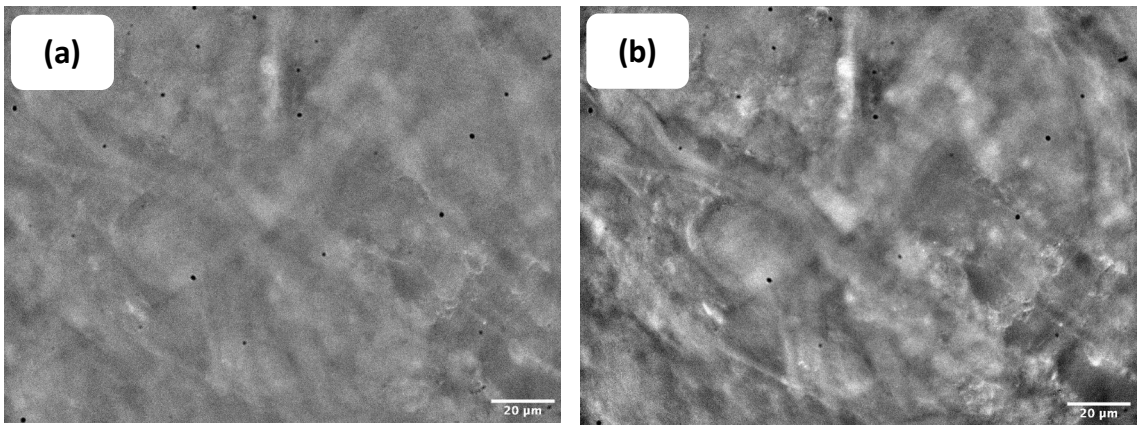

Figure 2-6. LED pinhole diameter experiment (a) $\phi = 12$ mm and (b) $\phi = 0.8$ mm. Note that phase contrast is significantly improved with the smaller pinhole size.

Discussion

The OBC system generates phase contrast analogous to OBM with oblique back-scattered light and epi-illumination, but without the need for external fiber sources. This decreases the form-factor of the system and enables the use of high magnification, high NA objective lenses. For example, in reviewing the OBM data in Figure 1-21, it is important to notice that the phase particle under study is 45 μm in diameter, approximately 5X bigger than a red blood cell and 20X bigger than a platelet. The NA that is used in this prototype is an impressive 0.8, however this is only achieved by using a micro-endosocope with a short working distance

of 60 μm that also uses an imaging fiber bundle that imparts structural artifacts in the image that degrade resolution. This is in contrast to the OBC system, where a magnification of 40X and an NA of 1.15 are easily achieved. In fact, nearly any microscope objective should work with OBC. The improvement in resolution and magnification is readily apparent in the images of the lipid phase particle shown in Figure 2-5, which are approximately the size of a red blood cell. Small features on the order of hundreds of nanometers are readily visible using OBC, which will be critical for resolving sub-cellular features such as granules within white blood cells.

Additionally, by imaging the LED directly through the microscope objective, small source-detector separations can be achieved. Due to the mostly forward-scattering nature of tissue, the further the illumination source is from the optic axis, the less light will make it into the imaging system. This means that either slower imaging speeds or higher power illumination sources must be used in order to achieve high signal-to-noise. The external fiber sources of OBM must be placed an order of magnitude further away from the detection optic axis than with OBC.

Source-detector separation is important for more than just collection efficiency and imaging speed. Though OBM can only achieve source-detector separation on the order of millimeters, the authors of the seminal OBM paper still used Monte Carlo simulations to investigate the impact of smaller source-detector separation on back-scattered light obliquity (Figure 1-24). In these simulations, the authors found that obliquity peaks at δx = 200-250 μm with point-source illumination. With larger diameter illumination, such as the 1 mm diameter fiber used, the peak phase contrast is found at approximately 600-700 μm, however due to steric hindrance from the external fiber sources and endoscopic imaging objective, they are not able to physically achieve this. Interestingly, it appears that the optimal source-detector separation for a given source is approximately the source radius. This is an important, but logical conclusion. Once δx is reduced below the source radius, part of the illumination goes beyond the imaging optic axis, and this portion of illumination produces back-scattered light

that is effectively net oblique in the opposite direction, and counteracts the phenomenon producing the phase contrast. Thus, the smaller the source that is used to illuminate tissue, the smaller δx can be while still maximizing phase contrast. And, the smaller δx is, to about 200-250 μm, the higher the net obliquity of light can be achieved.

The OBC system outlined in Figure 2-1 enables the reduction of the source-detector separation down to the ideal 200-250 μm predicted in Figure 1-24. By laterally translating the LED, its conjugate plane in the object is also laterally displaced, due to the critical illumination of the microscope. The contrast across a lipid phase particle approximately the same size as a blood cell is measured in Figure 2-5(b) at discrete values of δx. With $\delta x = 0\mu m$, the LED is imaged on-axis, and no appreciable phase contrast occurs across the lipid particle. As the δx is increased to approximately $\delta x = 240\mu m$, the phase contrast improves continuously, and the particle becomes more visible. This result is in direct agreement with the results from Ford et. al.'s simulations of source obliquity maximization with a point source. At $\delta x > 240\mu m$ however, the phase contrast begins to decline quite rapidly. This is due to the limitation of the field of view of the microscope objective, and is no longer directly comparable to the external fiber source illumination simulations of OBM. Importantly, the LED is also de-magnified. The collimating lens by the LED and the microscope objective together create a 4F system with a de-magnification factor of approximately 4X. This provides a straightforward way of illuminating tissue with a small enough source that the maximum phase contrast of $\delta x = 200 - 250\mu m$ can be achieved. The LED emitting surface is approximately 1mm x 1mm, which is demagnified to 250 μm x 250 μm in object space. Note that the source half-width (analogous to the radius of the fibers used in OBM), is then 125 μm, allowing small source-detector separations to be achieved without the illumination crossing over the optic axis. The importance of the size of the source on phase contrast is further evidenced in Figure 2-6, where an on-axis LED is imaged into a piece of paper with varying pinhole size. With the pinhole fully open, the LED is imaged in with its full emitting surface area showing into the sample Figure 2-6(a). Since there is no source-detector separation across

most of the field of view, phase contrast vanishes. However, when the LED source size is stopped down, Figure 2-6(b), phase contrast re-emerges in a pattern that shows improved contrast with radial distance from the optic axis. These results highlight a few important things. First, either the LED or the imaging sensor can be laterally displaced to observe phase contrast. In the case of Figure 2-6(b), phase contrast is still visible despite the on-axis nature of the LED image because areas in the periphery of the field of view still have an appreciable source-detector separation. Second, the size of the source plays an important role in the phase contrast produced by the system. This is something predicted by OBM simulations in Figure 1-24. However, while external fiber sources limit OBM, OBC allows small enough source sizes and close enough source-detector separation to optimize phase contrast with oblique back-illumination.

After optimizing a high-speed, single-source OBC system, a dual source OBC system with diametrically opposed illumination capable of simultaneous wide field of view imaging was developed. The prototype shown in Figure 2-2 contains two spectrally distinct LEDs on the same LED board to illuminate tissue from opposite directions. Back-scattered light is spectrally separated by a dichroic mirror, and imaged onto two CMOS sensors synchronized with a hardware trigger. This system enables simultaneous acquisition at 120 fps with a 350 μm x 265 μm field of view. Considering vessels are spaced approximately every 200 μm apart in the ventral tongue oral mucosa, this field of view is sufficient for finding vessels easily when imaging. At 120 Hz imaging with a 0.5 ms exposure time and with blood cells traveling up to 1 μm/ms, a blood cell should travel approximately 8 μm per frame with a motion blur of 0.5 μm, or 3 pixels. Considering the resolution of the microscope objective at 640nm is 0.52 μm, motion blur degrading the image quality should be on par with diffraction. Further, with a typical red blood cell diameter of around 7 μm, a lateral translation of 8 μm per frame at 120 fps should still be sufficient for video tracking algorithms to work. If necessary, however, frame rates significantly higher can be achieved by cropping the active area on the CMOS sensors.

Conclusion

Oblique back-illumination capillaroscopy provides combined phase and absorption contrast with epi-illumination at high speed that could enable *in vivo* blood cell imaging in humans in a label-free manner. Utilizing oblique back-scattered illumination, OBC produces phase contrast similar to differential phase contrast microscopy, where transmitted light at an oblique angle through phase objects can refract towards or away from the system aperture, thus converting phase changes to intensity changes. OBC is similar to its predecessor oblique back-illumination microscopy, which generates oblique back-scattered light acting as a virtual transmissive source through tissue back-scattering of laterally offset illumination. However, compared with OBM, OBC offers several important advancements. First, OBC obviates the external fiber sources required in OBM. These external fiber sources limit the minimum source-detector separation that can be achieved, which reduces collection efficiency and prevents optimizing obliquity of back-scattered light. OBC is capable of producing source detector separations on the order of hundreds of microns, instead of millimeters in OBM, which, in agreement with simulations from the seminal OBM paper, optimizes phase contrast. The elimination of external fiber sources also reduces the form factor of the OBC imaging probe, which could eventually be critical for imaging difficult-to-reach recesses in the human body, such as capillaries in the oral mucosa or imaging via endoscopic or laparoscopic approaches. Unlike conventional capillaroscopy, which contains absorption-only information that primarily highlights red blood cells, the addition of phase contrast should enable the resolution of otherwise transparent objects such as white blood cells and platelets. Thus, OBC is capable of revealing the etiology of optical absorption gaps, providing increased accuracy of non-invasive neutropenia screening, and perhaps even further white blood cell differential classification. Compared to other non-invasive epi-mode imaging modalities such as reflectance confocal microscopy, OBC is simple, fast, readily miniaturized, and has no scanning or moving parts. Its ability to record the forward scattered field through tissue with epi-illumination provides

access to rich information about low spatial frequency objects such as the overall cell shape. However, before turning to *in vivo* imaging, an *in vitro* model of capillaries will be studied to enable controlled imaging studies of OBC with human blood cells. Using this model, paired OBC imaging data with ground truth blood cell concentrations, classifications, and clinical diagnosis can be provided, which will be essential for the long-term translation of the technology to human use.

Chapter 3

A tissue-realistic microfluidic capillary model for establishing blood count ground truth and evaluating examples of hematologic disease.

Introduction

The OBC systems outlined in Chapter 2 theoretically have the ability to resolve blood cells *in vivo* given their spatial and temporal resolution, combined phase and absorption contrast, and epi-mode illumination geometry. However, the long-term success of OBC as a translational device will only be realized with the application of automated computer vision algorithms to analyze the video data collected. Deep learning algorithms that enable instance segmentation, video tracking, classification, and counting are likely to succeed [62, 209]. However, these algorithms require substantial amounts of labeled training data for each task they are to perform, a necessity often difficult to achieve with medical data [210, 211]. While genetically modified animal models could be used to produce ground truth blood cell classification labels with fluorescence, the use of exogenous fluorescent labels in humans is generally not preferred due to safety concerns. Transfer learning and domain adaptation from animal blood cells to human blood cells could also pose problems. For example, even mice, whose hematologic characteristics are often considered a good model for human studies, demonstrate significant

differences in blood cell size, concentration, and capillary diameter [212–214]. In the case of *in vivo* blood cell imaging with OBC in humans, generation of ground truth data is particularly challenging due to the novelty of the technique and a lack of previously established databases. While red blood cells can easily be distinguished from white blood cells based on absorption information provided by hemoglobin, and platelets can be distinguished from white blood cells based on substantial and consistent differences in size, the sub-classification of white blood cell type is more challenging. A tissue-realistic microfluidic model through which human blood with ground truth information can be flowed and imaged is a promising alternative technique, provided it is sufficiently realistic and representative of human tissue.

Optical phantoms mimicking biological tissue continue to be active areas of research in recent decades [215–217]. While numerous materials and techniques have been proposed, one of the most robust approaches is the use of polydimethylsiloxane (PDMS) doped with scattering and absorbing agents to match tissue optical properties [215, 217]. PDMS provides a firm, moldable base material with similar index of refraction to biological tissue ($n \sim 1.4$) [216]. Complex, multi-layer tissue phantoms, analogous to the layers of human skin, have also been demonstrated [53, 218].

While progress towards accurate modeling of bulk optical properties in tissue phantoms has been made, phantoms that permit physiologically realistic blood flow have been more difficult to fabricate. Several publications use microcapillary glass or plastic tubing embedded into a bulk phantom [219, 220], while another study proposed etching away thin copper wires with ferric chloride [221]. While relatively easy to fabricate, these techniques tend to use channels wider than a single capillary lumen, and their manufacture can introduce artifacts that are not representative of tissue. Artifacts include a volume of non-scattering material surrounding the channel in the case of tubing, and an irregular lumen surface in the case of etching. Microfabrication of smaller, capillary-sized channels using photolithography was accomplished for laser speckle contrast imaging calibration, however, the use of a glass-PDMS interface to seal the channels necessitated the capillaries be imaged beneath a transparent

glass substrate, rather than embedded beneath a scattering media [222]. More recently, an impressive multi-layer retinal phantom was made using photolithography and oxygen plasma bonding to create embedded microfluidic channels down to 50 μm; however, blood flow was not demonstrated [223]. Thus, despite tremendous progress, there is still a need for the development of an *in vitro* model of human capillary blood flow embedded in a tissue realistic medium.

In this chapter, a microfluidic device is presented that is made entirely of PDMS doped with TiO_2 and India ink to match human skin optical properties [55, 224]. Using photolithography techniques, the device has channels as narrow as 15 μm in diameter, similar in size to a human capillary, and enables blood flow exceeding the large physiological range of speeds predicted in human vasculature. Importantly, the microfluidic channels are embedded beneath a thin membrane of PDMS doped with TiO_2 and India ink, mimicking how capillaries reside beneath a thin layer of scattering skin within a bulk semi-infinite turbid medium *in vivo*. Using this model, human blood is flowed and imaged in the OBC system. The phase contrast is again optimized by laterally translating the LED similar to the lipid phantom experiment in Figure 2-5, however this time using a white blood cell as the object. Whole blood with ground truth complete blood count information is obtained and imaged, various examples of hematologic disorders including sickle cell disease, anemia, and leukemia are studied, and blood cell isolation experiments using negative selection antibody kits are conducted to study sub-classes of white blood cells. These experiments demonstrate the diverse utility of the microfluidic devices for OBC ground truth data generation, but should only be considered a starting point from which numerous other diseases, blood cell classes, and blood concentrations should be imaged and studied with paired ground truth information.

Materials and Methods

Microfluidic fabrication

The microfluidic device is made of polydimethylsiloxane (PDMS) doped with TiO_2 and India ink to introduce scattering and absorption. These doping agents were added following a similar protocol to Ayers et al., with 1.5 mg/mL TiO_2 added to make $\mu_s' \sim 1.5\ mm^{-1}$ at 650nm, and 0.2 mg/mL India ink to make $\mu_a \sim 0.02\ mm^{-1}$ (Figure 3-1) [52, 53].

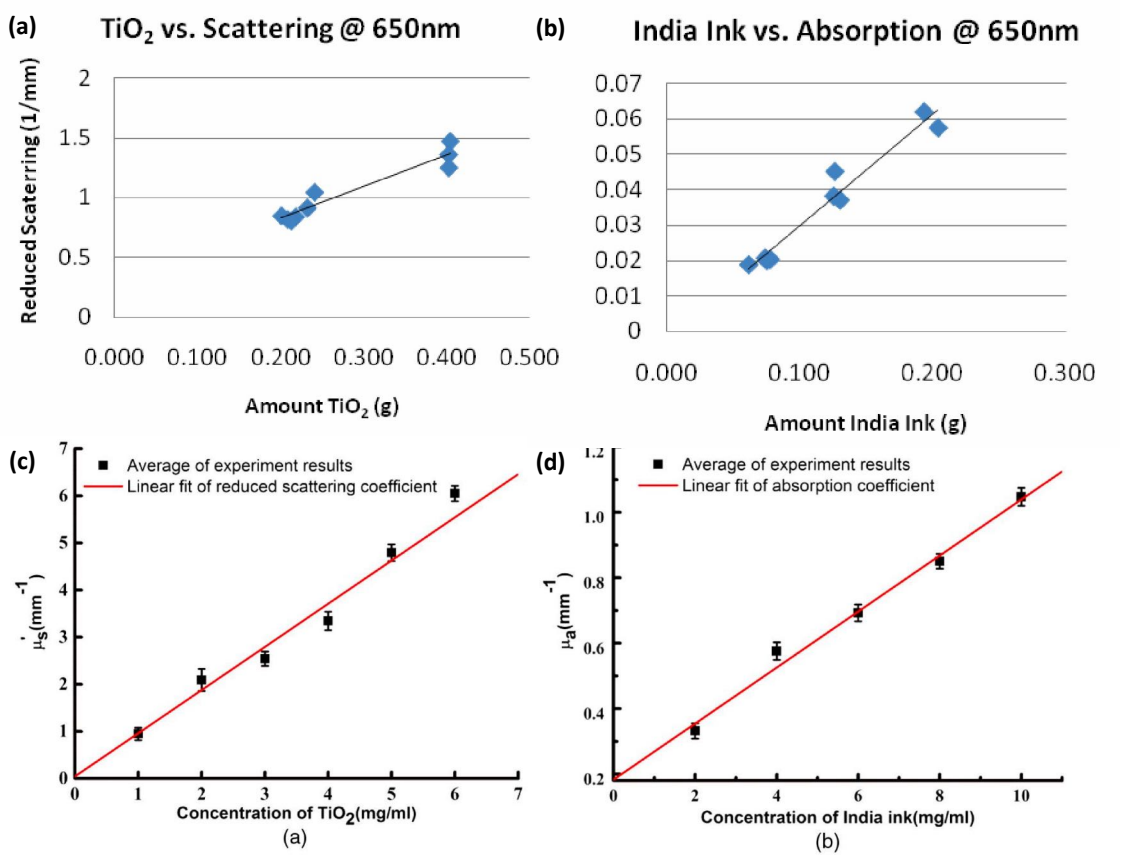

Figure 3-1. (a) Reduced scattering vs. TiO_2 in 275mL of PDMS, and (b) absorption vs. India ink in 275mL of PDMS [52], (c) reduced scattering vs. TiO_2 concentration in PDMS, and (d) absorption vs. India ink concentration of PDMS [53].

Figure 3-2(a) outlines the protocol used to fabricate the capillary phantom. First, a custom UV mask was designed in the shape of the desired capillary bed structure (Figure 3-2(b)). It consists of a branching design, 55 mm in total length, starting with a single 1 mm wide channel, and bifurcating 6-times (every 4.25mm) to generate 64 individual 15 μm wide

channels. The 15 μm channels symmetrically recombine back to a single 1 mm wide channel as the outlet. The UV mask was overlaid onto a Si wafer coated with SU8-3010 photoresist. SU8-3010 was spin-coated onto a clean 76.2 mm Si wafer at 1000 RPM for 45 seconds, and soft baked at 95°C for 10 minutes. A 350nm long pass filter was used for UV exposure in a mask aligner, following the SU8-3010 manufacturer's instructions [225]. A layer of photoresist (PR) 15 μm in height (h) was generated on the wafer, and hard baked (200° C, 20 minutes) to finalize the device mold. Doped-PDMS is cast over the device mold taped to the bottom of a petri dish, and cut out using a razor blade after curing at 75°C overnight to create the device base. Separately, a different Si wafer was coated with SU8-1813 photoresist, and soft baked at 95°C for 10 minutes. A thin membrane of doped-PDMS was spin-coated on top of the PR layer with different spin-coating parameters determining the membrane thickness (s). Using oxygen plasma bonding, the PDMS membrane was fused with the cut-out PDMS device base, and the final device was generated by releasing the membrane-bound Si wafer by dissolving the soft-baked SU8-1813 photoresist layer with acetone.

The finished capillary phantom consists entirely of media with optical properties and index of refraction similar to tissue, and has capillaries with 15 μm width (w) and 15 μm height (h). The depth of the capillaries (s) from the device surface is adjustable by changing the spin coating rate of the PDMS membrane. Membrane thicknesses ranging from 50 μm to 500 μm were achieved. Flow through the device is readily controlled by inserting PEEK tubing (1/32" OD) into holes carved through the PDMS device base before oxygen plasma bonding by a 20 gauge blunt tipped needle.

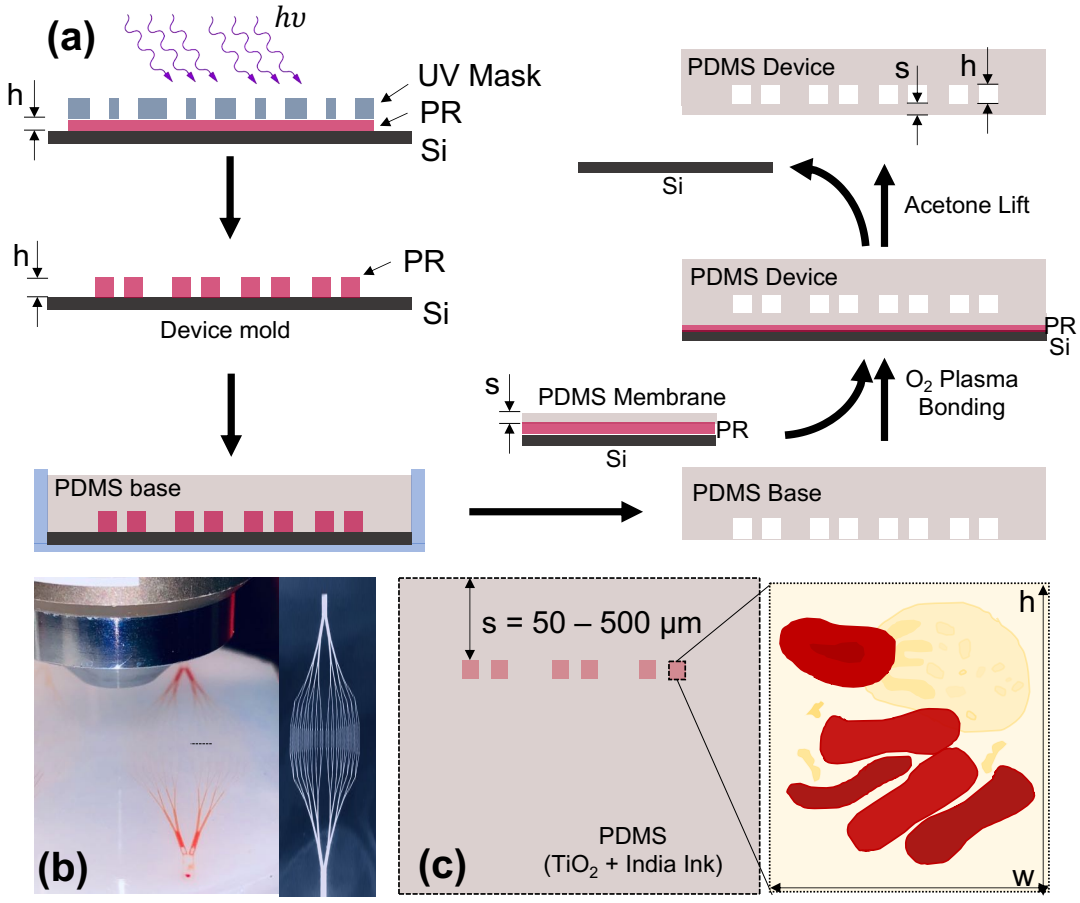

Figure 3-2. (a) Method for fabrication of microfluidic device. A standard photolithography procedure with SU8-3010 photoresist (PR) was followed to create 15 μm channel height (h) on a silicon wafer (Si) engraved with a custom UV mask in the shape of the capillary bed design. The device base is created by casting PDMS (with TiO_2 and India ink) over the device mold. Separately, a membrane is created by spin coating PDMS onto a SU-1813 PR coated silicon wafer. Using oxygen plasma bonding, the membrane is securely bonded to the device base, and the SU-1813 PR is dissolved with acetone to remove the Si wafer and create a PDMS-only device. (b) Image of capillary phantom and corresponding UV mask. (c) Phantom cross-section of smallest channels - 15 μm in height (h), 15 μm in width (w), and variable depth beneath the surface (s). [54]

Blood cell imaging

The microfluidic devices are connected to a 1mL syringe via PEEK tubing with luer lock connectors (IDEX 1569L, P-659, F-247, F-333NX) and mounted into a syringe pump (Figure 3-3(a)). Whole blood is added to the syringe, containing small a magnetic stir bar on the inside. A custom 3D printed syringe mixer consisting of a rotating magnet external to the syringe is controlled via servo motor powered by an Arduino. This is done to ensure the blood stays homogenously mixed during imaging (Figure 3-3(b)-(c)), which otherwise tends to settle and visually separate by density after only 15-30 minutes. Blood is pumped into the microfluidic chamber using a syringe pump (Braintree Scientific BS-9000-2). Flow rates from 0 mm/s up to 6 mm/s were achieved in the microfluidic device without rupturing the thin membrane creating the top of the channels.

For optimizing phase contrast to a white blood cell, images of the same leukocyte were taken as the LED source in the OBC system was laterally displaced (Figure 3-4). The source detector-separation (δx) of the OBC system was varied similar to Figure 2-5, while the contrast-to-noise ratio (equation (3.1)) was optimized. Second, using a similar approach, thin scattering membranes of varying depth (s) were layered on top of the phantom to enable studying the CNR to a white blood cell with varying imaging depth through a scattering medium. The thin membrane layers were alternated with mineral oil to index match the PDMS and prevent scattering from air PDMS interfaces. An alternative approach would be to create multiple microfluidic devices with varying spin coating parameters to change capillary depth, however the approach taken allows the study of the same leukocyte across the experiment. For blood cell isolation experiments, human whole blood is treated with magnetic antibody negative selection kits to isolate individual white blood cell types (STEMCELL Technologies EasySep 19666, 19655, 19669, 19656, 19667). These include the five major white blood cells of a complete blood count with 5-part differential: neutrophils, lymphocytes, monocytes, eosinophils, and basophils. WBC pellets are concentrated with centrifugation (300g x 5min) and resuspended in EasySep Buffer (STEMCELL Technologies 20144) before

imaging in the microfluidic devices. Human whole blood with paired ground truth hematologic and complete blood count information was obtained from the Johns Hopkins Hospital core laboratory under a protocol approved by the Johns Hopkins University IRB (IRB00215528). When ground truth blood counts or hematologic diagnosis were not needed, human whole blood was purchased from ZenBio (SER-WB-SDS).

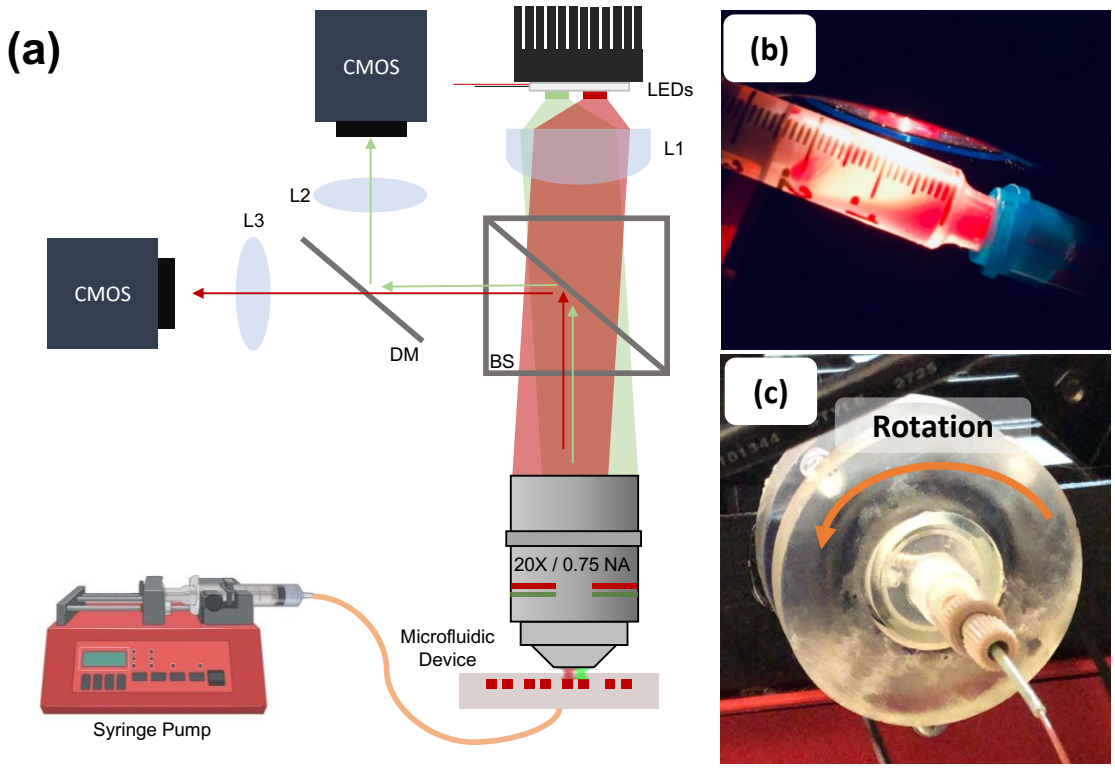

Figure 3-3. (a) The microfluidic device is imaged in the dual-channel OBC system connected to a syringe pump. (b) Whole blood shows significant separation due to differences in blood cell and plasma density, which can be alieviated with a cystom syringe mixer (c) [55].

$$CNR = \frac{(\mu_a - \mu_b)}{\sqrt{\sigma_a^2 + \sigma_b^2}}. \tag{3.1}$$

When studying anemia, nine blood samples with varying hemoglobin were selected for imaging in microfluidic device channels. To correlate absorption measurements in the 530nm green channel to hemoglobin concentration, a time-average of 20 consecutive frames in the OBC system was taken and the capillary optical density (OD) compared to background tissue was calculated according to equation (3.2).

$$OD = -log_{10}(I_t/I_0) \tag{3.2}$$

Where I_t is the transmission through the capillaries and I_0 is the transmission through the background tissue (average value above and below the capillary).

Various other examples of hematologic disorders were imaged including sickle cell disease, chronic lymphocytic leukemia, neutropenia, leukocytosis, eosinophilia, thrombocytopenia, and myeloproliferative disorders. These represent only a portion of hematologic disorders that could be studied with OBC and were selected based on availability.

Results

Optimizing source-detector separation for WBC phase contrast

Previously, the phase contrast of OBC was optimized by varying the source-detector separation (δx) while imaging a lipid particle approximately the same size as a blood cell in a scattering agar phantom (Figure 2-5). While this approach demonstrated the analogous nature of phase contrast produced by OBC as compared to OBM, the optical properties of this phantom were unknown. Thus, it is unclear how representative this phantom model of phase contrast optimization is to biological tissue. The microfluidic chambers offer a more realistic scenario to test the same phenomenon. Using a technique similar to Figure 2-5, the phase contrast was again optimized by laterally translating the LED to vary the source detector separation (δx) while blood flow was held stationary with a white blood cell present in the field of view (Figure 3-4(a)-(c)). The contrast to noise ratio of plot profiles were measured across the white blood cells in the direction parallel to LED translation, and the phase contrast was found to be optimized at δx = 280 μm. With smaller δx, phase contrast was reduced and ultimately vanished as the source obliquity was degraded. At higher δx values, phase contrast was still present, however the signal was corrupted by noise as the signal from the LED weakened as its image was translated outside the field of view of the microscope objective. Figure 3-4(d)

shows representative intensity plot profiles from the on-axis illumination (blue curve, δx = 0 μm) and from the phase contrast optimized displacement (orange curve, δx = 280 μm). Note that with on-axis illumination, the intensity profile remains nearly flat across the white blood cell, and there is little contrast distinguishing it from the background intensity contributed by the scattering medium. This is similar to what was observed in Figure 2-5(c). However, with the LED displaced to δx = 280 μm, the characteristic gradient of illumination across the white blood cell becomes apparent, with the plasma membrane of the white blood cell being darker on the left and brighter on the right (akin to Figure 2-5(d)). Note in this case the LED is laterally displaced off to the left, producing an intensity profile across the white blood cell that appears dark on the side closer to the LED and bright on the side further from the LED. This is because the relatively spherical white blood cell has a higher index of refraction than the lower-index blood plasma surrounding it. It acts similar to a positive lens, as is outlined in Figure 1-21(c). However, the microfluidic chamber edge demonstrates the opposite intensity parity of the white blood cell (bright-to-dark). This is because the oblique light is traversing a straight, flat edge of the capillary channel from PDMS into blood plasma, a higher-to-lower index of refraction change that causes the light to bend towards the optical system on the edge closer to the LED image, but away from the optical system on the opposite channel edge.

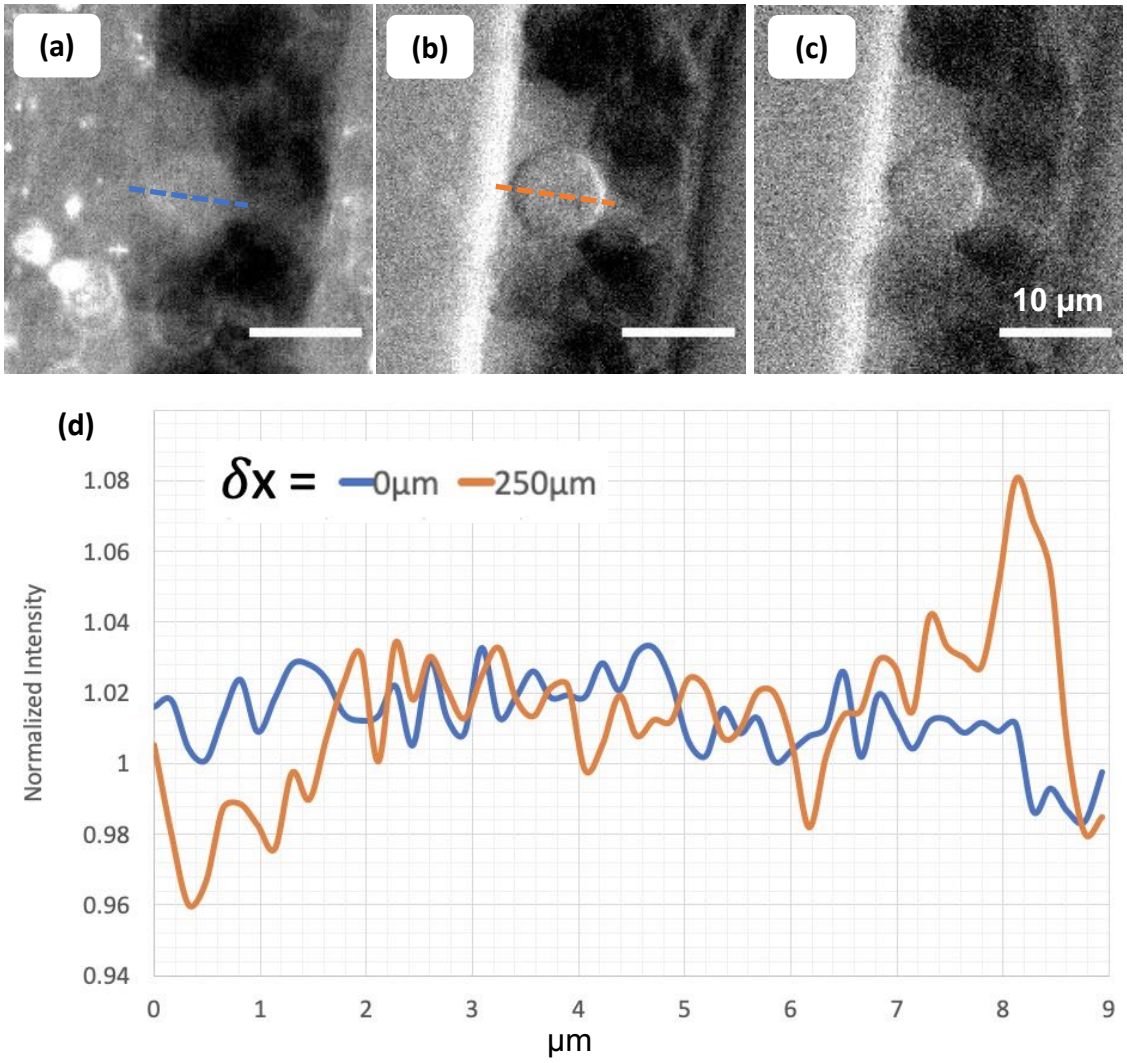

Figure 3-4. Representative images of the same white blood cell at different source-detector separations. (a) On-axis illumination (δx = 0 μm), (b) optimized oblique illumination (δx = 280 μm), (c) oblique illumination past optimization (δx = 470 μm). Phase contrast is optimized with the LED translated δx = 280 μm in object space. Phase contrast is insignificant with on-axis illumination, and phase contrast becomes noise-dominated beyond δx > 280 μm. Scale bars are 10 μm. [55].

OBM was shown to have phase contrast only with superficial tissue structures approximately less than one mean free path in depth (Figure 1-23). The microfluidic channels offer a controlled environment to study this phenomenon with blood cells. Layers of thin membrane doped with TiO_2 and India ink were added atop the microfluidic phantom to simulate the same white blood cell at increasing tissue depth. These results are shown in Figure 3-5, with CNR vs. δx plotted for five curves each of different imaging depth. Similar to Figure 1-23, contrast is highest in the most superficial samples, with a CNR ≥ 1 only at the 70 μm deep sample, and with contrast degrading entirely beyond 170 μm depth. The reason for the phase contrast persisting deeper than in Figure 1-23 is not entirely clear, but likely has to do with differences in the scattering generated by TiO_2 in the phantoms as compared to tissue, rather than any fundamental differences in the phase contrast produced by OBM vs. OBC. The degradation of the phase contrast is due to a net loss of obliquity with increased scattering depth as the illumination becomes more diffuse and homogenous. This phenomenon should apply equivalently between OBM and OBC, and is more so dependent on the optical properties of the object under study.

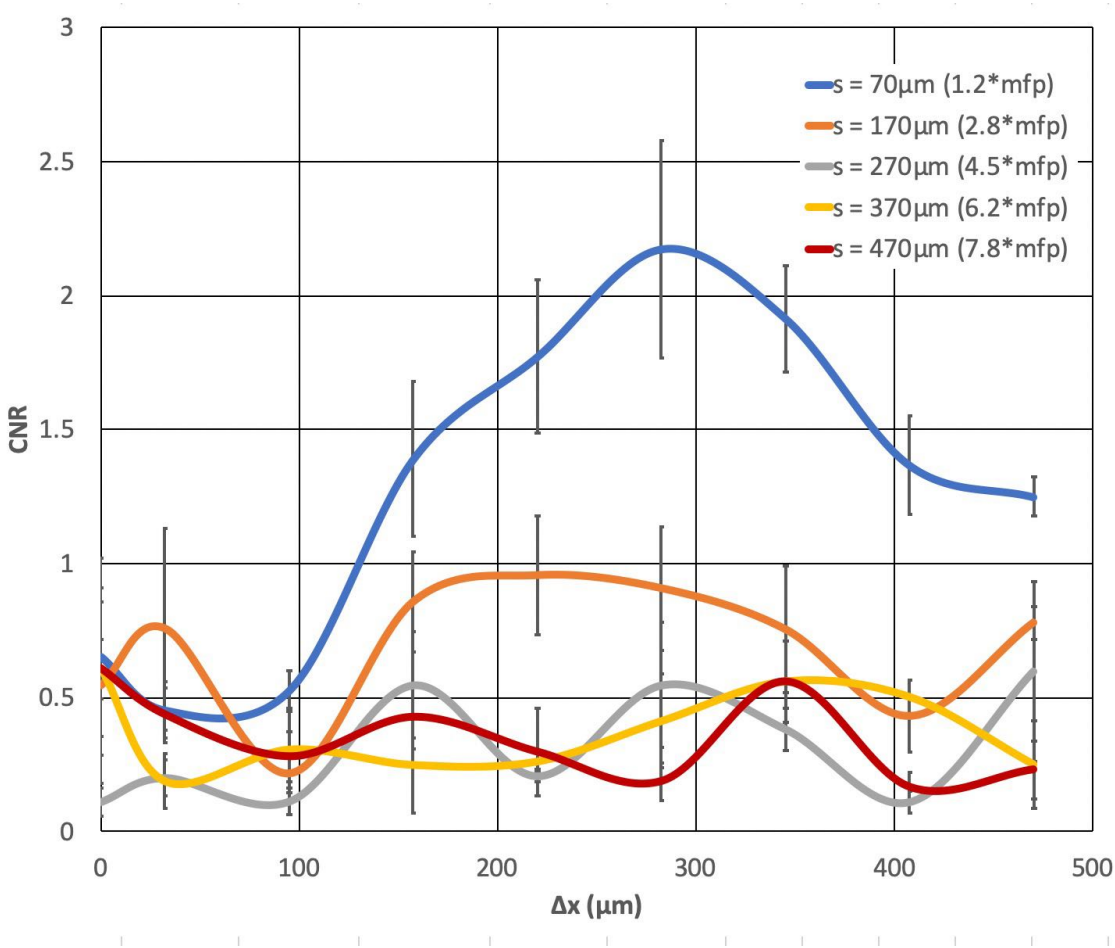

Figure 3-5. Contrast to noise ratio (CNR) vs. LED displacement (δx) at different scattering depths. At approximately $\delta x = 280\mu m$, white blood cell CNR appears to peak, and phase contrast diminishes with increasing scattering depth. Error bars are ± 1 standard error [55].

Whole blood imaging with ground truth

Whole blood with previously acquired complete blood counts can be imaged in the microfluidic device to generate ground truth information for training or validating deep learning algorithms essential to automating analysis of *in vivo* OBC images. An example of this is shown in Figure 3-6, where red blood cells and a white blood cell from whole blood with paired ground truth complete blood count are clearly visible flowing in the microfluidic device with the dual-source OBC system. At 530nm illumination, red blood cells appear dark due to absorption by hemoglobin, while white blood cells are bright like the background scattering phantom. However, despite not having efficient absorption in the visible spectrum, the WBC shown in

Figure 3-6 is clearly visible due to the phase contrast provided by oblique back-illumination. The red 640nm illumination channel shows primarily phase-only information, as neither red nor white blood cells absorb efficiently at this wavelength. As expected, the phase contrast profile in this channel has the opposite intensity parity to the green channel, with opposite sides of the cells and channel appearing bright/dark as compared to the green illumination. For simplicity, only the green channel is presented for many of the following results, however data was acquired with simultaneous triggering of two sensors recording each illumination wavelength. This approach can be used for a wide range of patient complete blood counts to generate vast amounts of training and testing data on human blood in a label-free, controlled manner. It can also be used to study specific examples of hematologic disease, some of which are demonstrated below.

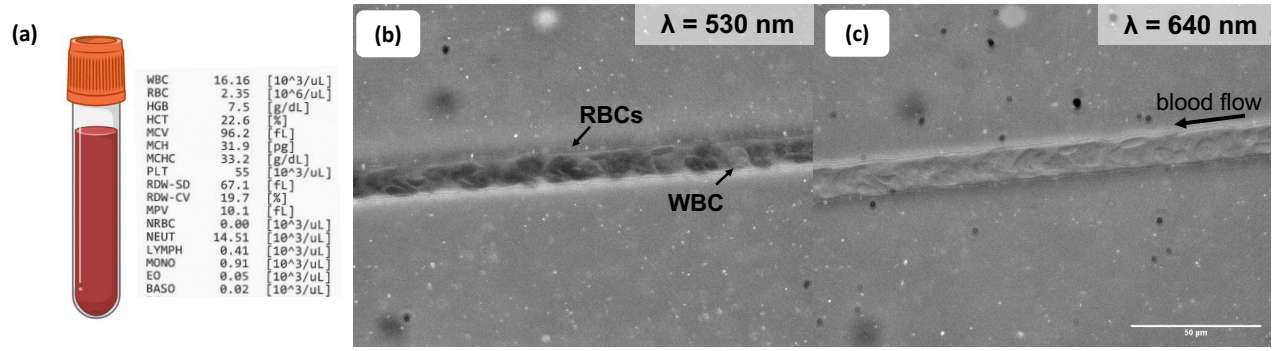

Figure 3-6. (a) Whole blood with ground truth complete blood counts is obtained and imaged in the microfluidic device with the dual-channel OBC system. (b) The green 530nm illumination channel shows combined phase and absorption contrast, while the red 640nm channel (c) shows primarily phase-only information.

Anemia

With a microfluidic model mimicking human capillaries and the ability to image whole blood with complete blood count and clinical diagnosis, OBC can be used to study hematologic disease. Anemia is a common condition characterized by a reduction in circulating whole blood hemoglobin. Its causes are numerous, including bleeding, nutrient deficiency, hemolysis, and malignancy, and it leads to dyspnea, fatigue, syncope, and cardiovascular failure if severe

[167, 226, 227]. By imaging blood from patients with a range in hemoglobin values from 4 g/dL to 15 g/dL, the potential utility of the microfluidic chamber with paired ground truth information can be demonstrated. Figure 3-7(a) shows time-averaged frames of whole blood flowing through the microfluidic device with a normal hemoglobin of 14 g/dL, as compared to blood from an anemic patient with hemoglobin of 4.2 g/dL. Note the intensity of the microfluidic chamber lumen appears darker in the case of normal hemoglobin due to increased absorption. These images are not flat-field corrected, and thus the gradient of illumination is readily observed from the green LED being imaged below the chamber. By quantifying the optical density (OD) using equation (3.2), a linear correlation to hemoglobin is quantitatively observed across nine different patient samples ($R^2 = 0.8492$, Figure 3-7(c)). Thus simple absorption-based measurements using 530nm illumination of whole blood could provide a means of non-invasive measurement of hemoglobin, provided calibration steps are taken to account for its correlation to optical density.

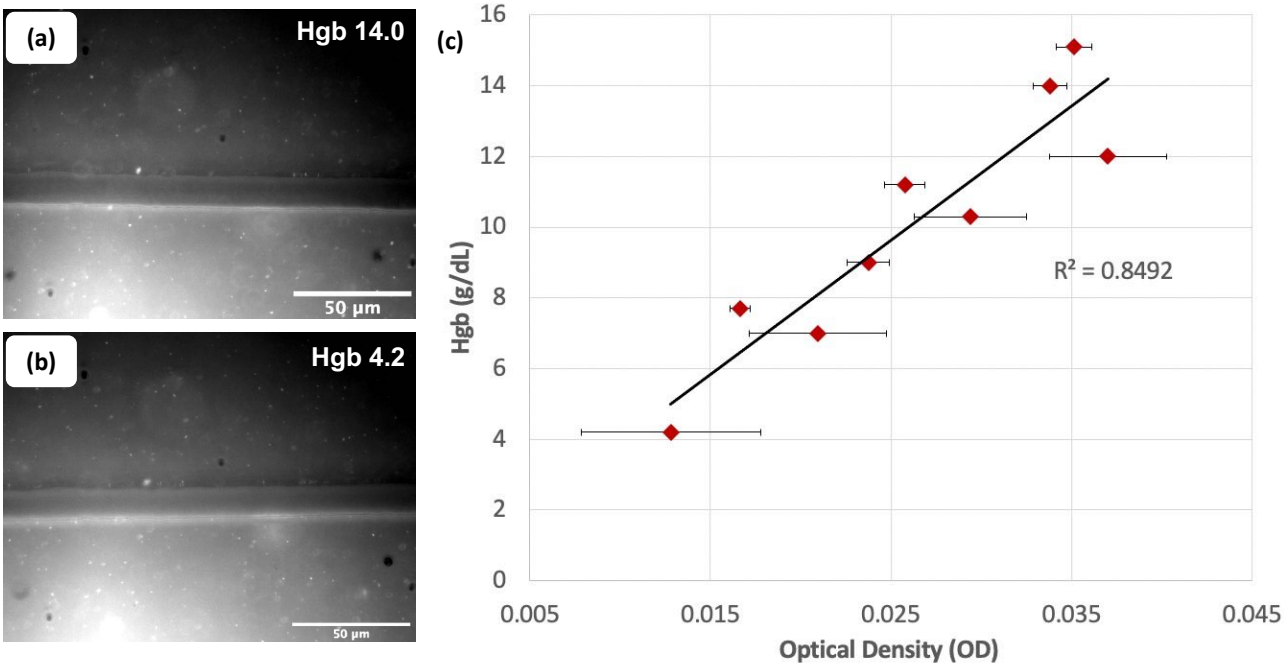

Figure 3-7. (a) Time average of whole blood with a normal hemoglobin of 14 g/dL, and (b) time average of whole blood with anemia and a hemoglobin of 4.2 g/dL. (c) Ground truth hemoglobin vs. measured optical density with OBC shows a linear correlation.

Due to the branching nature of the microfluidic device, wider channels can also be imaged, which show a remarkable difference in the density of red blood cells when looking at individual frames of the video that are not time-averaged (Figure 3-8). Here blood from an anemic patient with hemoglobin of 6.6 g/dL and hematocrit value of 23.7 (a), is qualitatively compared to a more normal blood sample with a hemoglobin of 11.8 g/dL and hematocrit value of 35.7, (b). These data suggest that OBC is likely not just able to estimate hemoglobin through optical density measurements, but may also provide a surrogate measurement of the hematocrit value by quantifying and comparing the relative area within the capillary that is composed of blood cells as compared to background blood plasma.

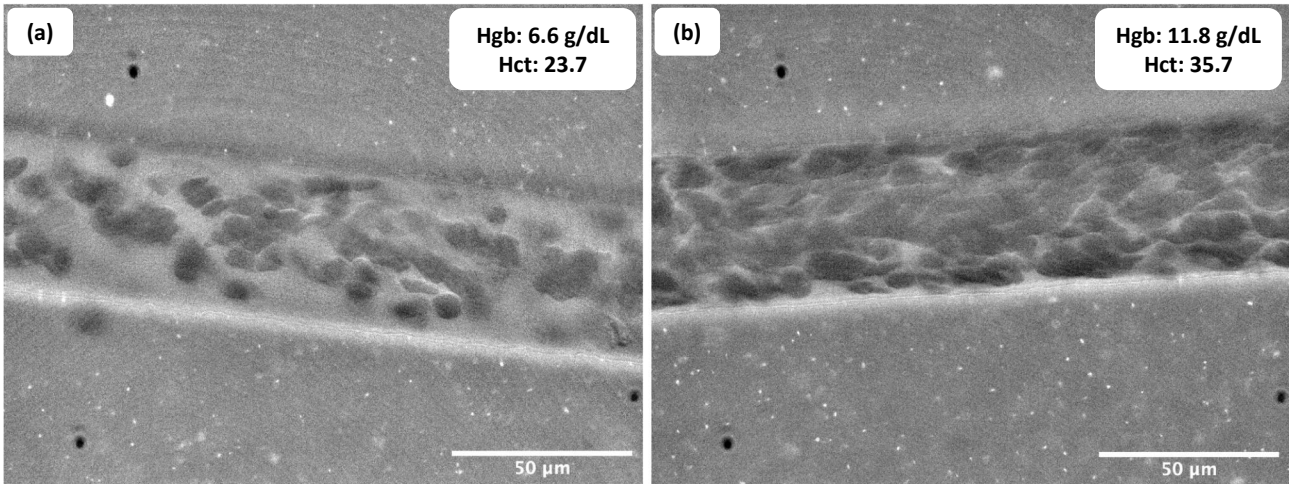

Figure 3-8. (a) Whole blood with anemia (Hgb 6.6 g/dL), and (b) normal whole blood (Hgb 11.8 g/dL).

The mean corpuscular value is of critical importance to determine the etiology of anemia. For example, low MCV values < 80 fL are often suggestive of iron deficiency or chronic disease, while high MCV values > 100 fL often imply an issue with DNA synthesis. In the middle are normocytic anemias (MCV 80-100 fL), which can be caused by bleeding. Importantly, in a conventional CBC, the MCV is determined analytically from the RBC concentration and the hematocrit value using equation (1.1), rather than through direct, independent measurement. In OBC however, due to the imaging nature of the technology, it may be possible to measure the MCV independently from the RBC concentration and hematocrit, which could yield

higher accuracy. Preliminary evidence that this may work is shown in Figure 3-9, where example red blood cells from two cases of anemia with different MCV values are shown. Figure 3-9(a) shows examples of red blood cells from a whole blood sample with Hgb 6.6 g/dL, Hct 23.7, and MCV 102.2 fL. This is an anemic case with an MCV right on the cusp of macrocytic. In contrast, Figure 3-9(b) shows examples of red blood cells from whole blood that has a Hgb 4.7 g/dL, Hct 16.6, and MCV of 70.9 fL, a microcytic anemia. By segmenting the cells and measuring their area manually, the normocytic/macrocytic RBCs show an area of 46.1 $\pm$ 4.5 μm^2, while the microcytic RBCs show an area of 19.2 $\pm$ 2.7 μm^2 (mean $\pm$ stdev.). Converting these two dimensional measurements of red blood cell area in the image to an accurate volumetric mean corpuscular volume measurement may require more complex mathematical modeling and imputation of red blood cell shape along the missing dimension. Regardless, even differences in the 2D measured RBC area in OBC images could be enlightening and clinically useful. Area-based measurements of RBC segmentation may be enough information alone as a surrogate *in vivo* measurement of MCV.

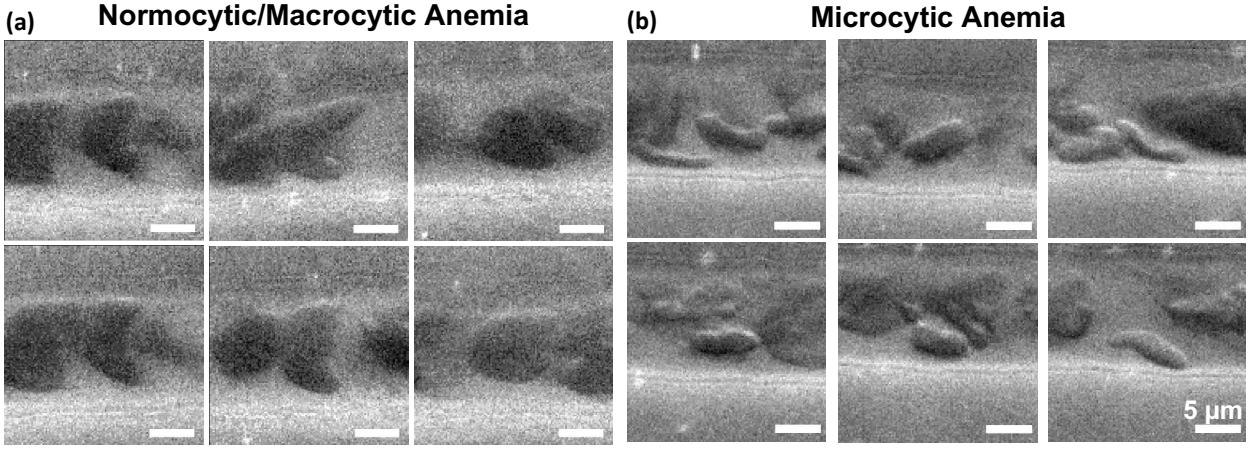

Figure 3-9. (a) Example red blood cells from whole blood with a normocytic/macrocytic anemia (Hgb 6.6 g/dL, Hct 23.7, and MCV 102.2 fL), and (b) Example red blood cells from whole blood with a microcytic anemia (Hgb 4.7 g/dL, Hct 16.6, and MCV is 70.9 fL).

While non-invasive anemia detection is not a new concept, OBC presents a novel and exciting window into red blood cell function and morphology that other conventional capillaroscopy [228] and wide-field smartphone camera based technologies do not [229]. With its high spatial

and temporal resolution, OBC offers the ability to not only correlate transmission-based absorption measurements calculated via optical density to hemoglobin, it also offers the ability to directly observe and measure red blood cell shape, potentially enabling the independent measurement of MCV. These data highlight the important unmet need in the analysis of OBC imaging data. As thousands of red blood cells can be observed in a matter of seconds, manual counting and segmentation will be prohibitive, and the development of automated analysis computer vision tools will be critical for translation of the technology.

Sickle cell disease

Sickle cell disease (SCD) is a genetic disorder of hemoglobin, where an amino acid substitution yields a new tetramer prone to crystallization in low-oxygen environments [56, 95, 230–233]. While normal red blood cells are deformable and able to squeeze through small capillaries and around tight turns in capillary loops, sickled RBCs are rigid and undeformable (Figure 3-10(a)-(b)). Their mechanical properties make them prone to microvascular occlusion, causing ischemia, hypoxia, inflammation, and tissue death that can occur in nearly any organ [56, 95, 230–233]. Though mortality has improved considerably in high-resource settings, SCD still accounts for a high burden of childhood death in low-resource settings [232–234]. Non-invasive, portable screening tools that operate without expensive or bulky laboratory equipment could help address this global health crisis. *In vivo* studies of SCD have shown a variety of changes in capillary flow and morphology (Figure 3-10(c)-(d)) [57, 58, 235], however no studies have utilized a technique such as OBC that can offer high spatial and temporal resolution of blood cells. Thus, OBC is a promising new investigational technology to study whole blood of patients with sickle cell disease in their native environment. For example, it could be used to screen undiagnosed patients for SCD in low-resource settings and track response to therapy such as transfusion or other pharmacologic intervention. It could also be used as a basic science tool for studying mechanisms of vaso-occlusive crises.

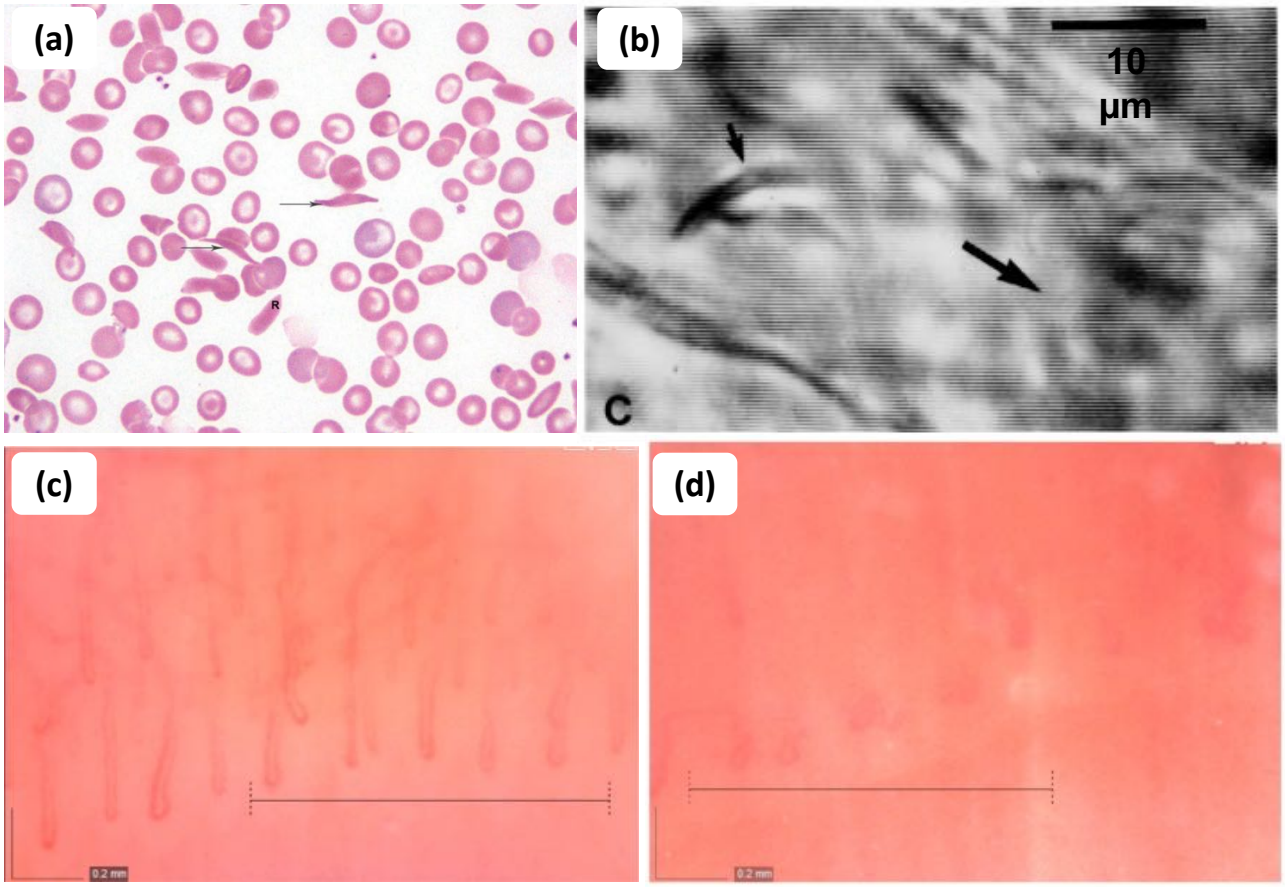

Figure 3-10. (a) Peripheral blood smear highlighting sickled RBCs [56], (b) *in vivo* imaging of mouse vasculature shows adhered sickled RBCs to vascular endothelium [57], nailfold capillaroscopy of a control patient (c) and a patient with SCD (d) shows capillary morphological changes [58].

Whole blood from patients with sickle cell disease was obtained and imaged in the microfluidic device to demonstrate the ability of OBC to resolve sickled cells. Figure 3-11(a) shows a widefield image of whole blood from a patient with sickle cell disease and anemia (Hgb 6 g/dL, Hct 18), as compared to a normal control (Hgb 14.6 g/dL, Hct 44.3) in Figure 3-11(b). Both the predicted reduced density of red blood cells from the anemia and the presence of sickled cells appear present. Examples of sickled cells vs. normal controls are further highlighted by selecting regions of interest around individual red blood cells from different time points throughout the videos (Figure 3-12).

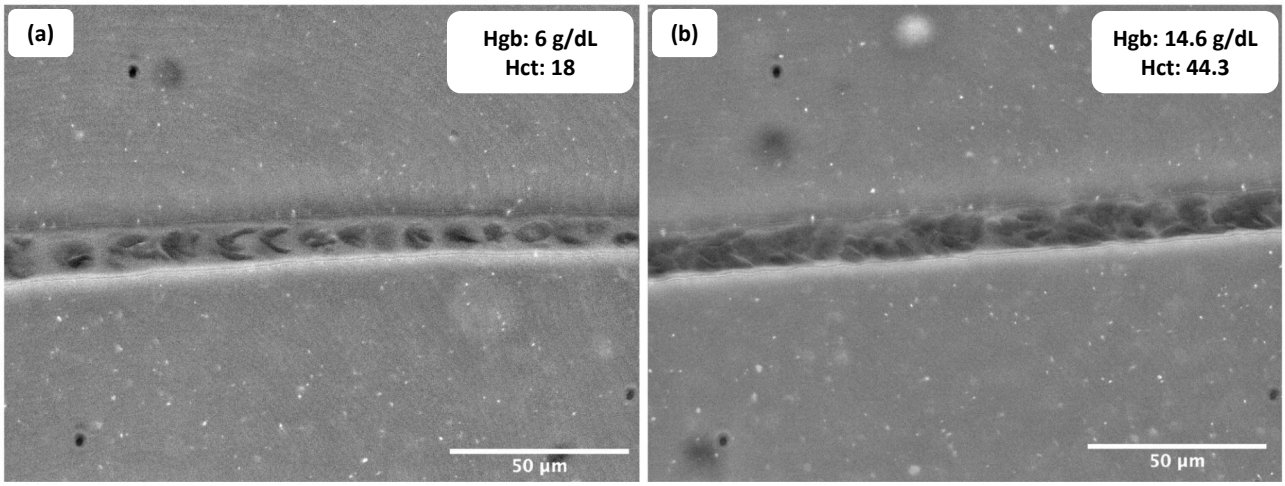

Figure 3-11. (a) Whole blood from a patient with sickle cell disease and anemia (Hgb 6 g/dL, Hct 18), and (b) normal whole blood (Hgb 14.6 g/dL, Hct 44.3).

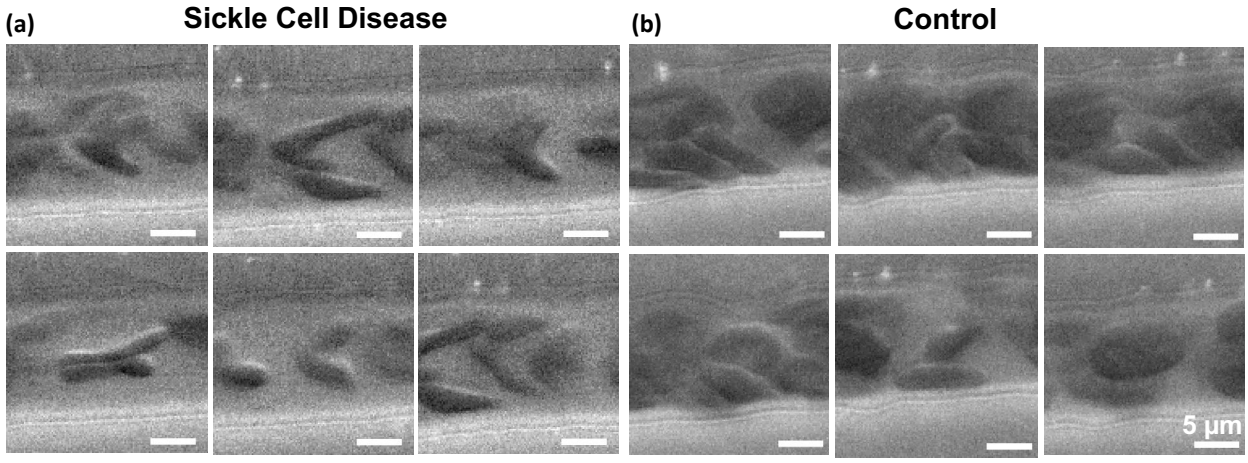

Figure 3-12. (a) Example red blood cells from a patient with sickle cell disease and anemia (Hgb 6 g/dL, Hct 18), and (b) control normal red blood cells (Hgb 14.6 g/dL, Hct 44.3).

From these preliminary data, it is clear the characteristic shape of sickled red blood cells is directly observable with OBC. Further studies correlating the morphology of red blood cells to oxygenation and disease severity should be conducted, along with *in vivo* studies of sickle cell patients. Importantly, the morphology of vasculature should be considered as a potential biomarker, as has been previously shown in the nailfold (Figure 3-10(c)-(d)). Further, similar to analysis of anemia and mean corpuscular volume, the development of deep learning based algorithms that can segment and analyze the morphology of red blood cells could be further

be utilized to estimate the percentage of sickled cells or other markers of disease severity. These approaches could yield an *in vivo* method to track the efficacy of interventions and treatments such as transfusion and other pharmacologic approaches. OBC could also provide novel insight and reveal new biomarkers related to rheological changes and microvascular occlusion that lead to tissue damage and pain crises. If adapted into a portable technology, such as with a mobile phone platform, OBC could yield a novel method of screening for sickle cell disease in low-resource settings. However, due to the production of fetal hemoglobin early in life leading to less blood cell sickling, further work must be done in order to create an imaging-based technology that can screen for SCD in newborns.

Leukocyte imaging

The quantification of optical absorption gaps in nailfold capillaroscopy videos has shown promise as a non-invasive neutropenia screening tool (Figure 1-15) [31–33]. However, without phase contrast or some other ability to resolve white blood cells, the composition of the OAGs is uncertain. Using OBC, white blood cells are visible, and can be distinguished from background blood plasma. The microfluidic model offers the ability to study a range of white blood cell concentrations and disorders. For example, Figure 3-13 shows examples of neutrophilia (a) and neutropenia (b), two common white blood cell disorders that can occur in the setting of infection and immunosuppression, respectively. Though the exact sensitivity and concentration estimation of white blood cells in these data cannot be estimated readily without the development of automated analysis or counting hundreds to thousands of cells manually, it is clear from a preliminary overview that many more white blood cells appear throughout the video in Figure 3-13(a) vs. (b). In the same time period, all five of the white blood cells shown in Figure 3-13(c) were observed in the neutrophilic data, while no white blood cells were observed in the neutropenic video. These results are consistent with observations of the frequency of optical absorption gaps shown in Figure 1-14 and Figure 1-15 correlating to neutropenia status. However, with the use of phase contrast provided by

the OBC system, the white blood cells can be directly observed, instead of just inferring their presence from gaps between red blood cells.

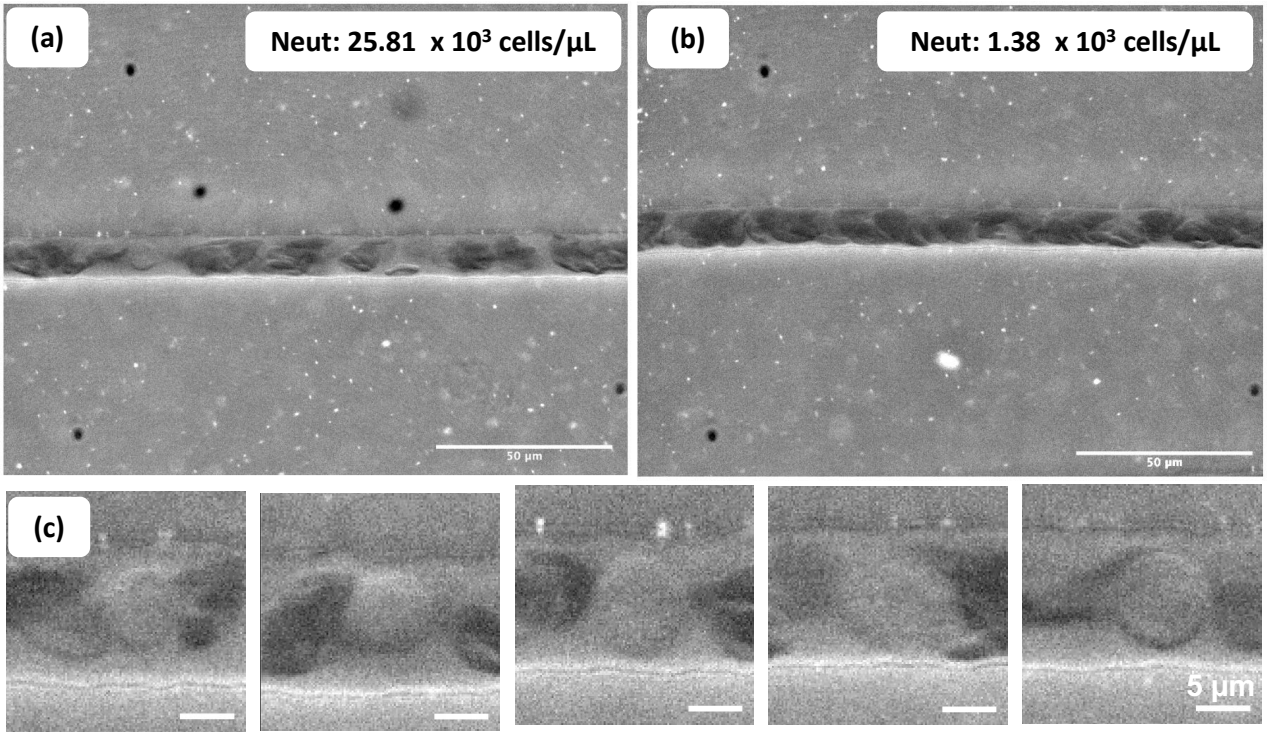

Figure 3-13. (a) An image of neutrophilic blood as compared to (b) neutropenic blood. (c) Five white blood cells were observed in the neutrophilic video while no white blood cells were observed in the same time period in the neutropenic blood.

One of the most promising applications for OBC pertaining to white blood cell imaging is in the study of leukemia. Leukemia, characterized by uncontrolled proliferation of leukemic cells in the bone marrow, includes a diverse set of cancers with different ages of onset, causes, and cellular origin. It is the 11th leading cause of cancer death and the most common childhood cancer worldwide [236]. While white blood cells typically are about 1000-fold lower in concentration than red blood cells, leukemic patients can often have leukocyte counts greater than 10-times normal [237]. In Figure 3-14 an example of chronic lymphocytic leukemia is presented, where whole blood with a severely elevated lymphocyte concentration is imaged in the microfluidic device. Note the concentration of lymphocytes here is 240.3 x 10^3 cells/μL, nearly 120-fold higher than the typical 2 x 10^3 cells/μL. Figure 3-14(a) shows an image from a wider channel with numerous, small white blood cells surrounded by absorptive

red blood cells, and Figure 3-14(b) highlights regions of interest surrounding some of the white blood cells observed throughout the video. As predicted by the chronic lymphocytic leukemia presentation, an abundance of small, round white blood cells approximately 5-7 μm in diameter consistent with mature lymphocytes were observed. The ratio of these lymphocytic CLL cells to red blood cells in a single frame of the video is a approximately 1:20, instead of the approximately 1:2000 ratio of lymphocytes to red blood cells predicted in a healthy patient's blood. Interestingly, there also appears to be sub-cellular structures observed in the the white blood cells of unknown origin.

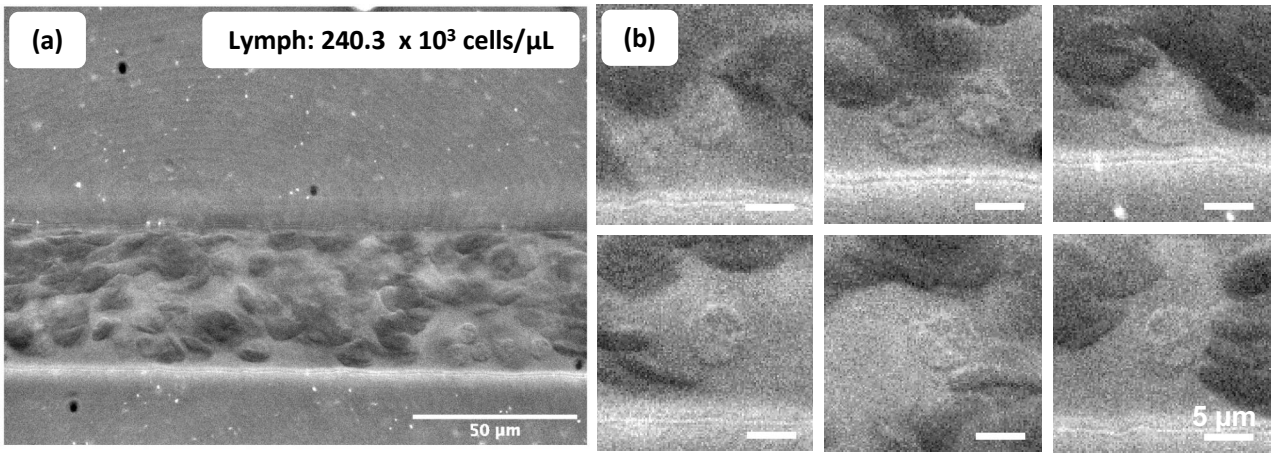

Figure 3-14. (a) A chronic lymphocytic leukemic patient's blood is imaged in the microfluidic chambers showing (b) numerous small white blood cells.

The microfluidic model also offers the opportunity to study rare hematologic disorders, such as the severe eosinophilia shown in Figure 3-15. Here, the eosinophil concentration is approximately 100X higher than normal counts. The white blood cells shown are approximately 10 μm in diameter and have distinct sub-cellular features that could be the cell's granules.

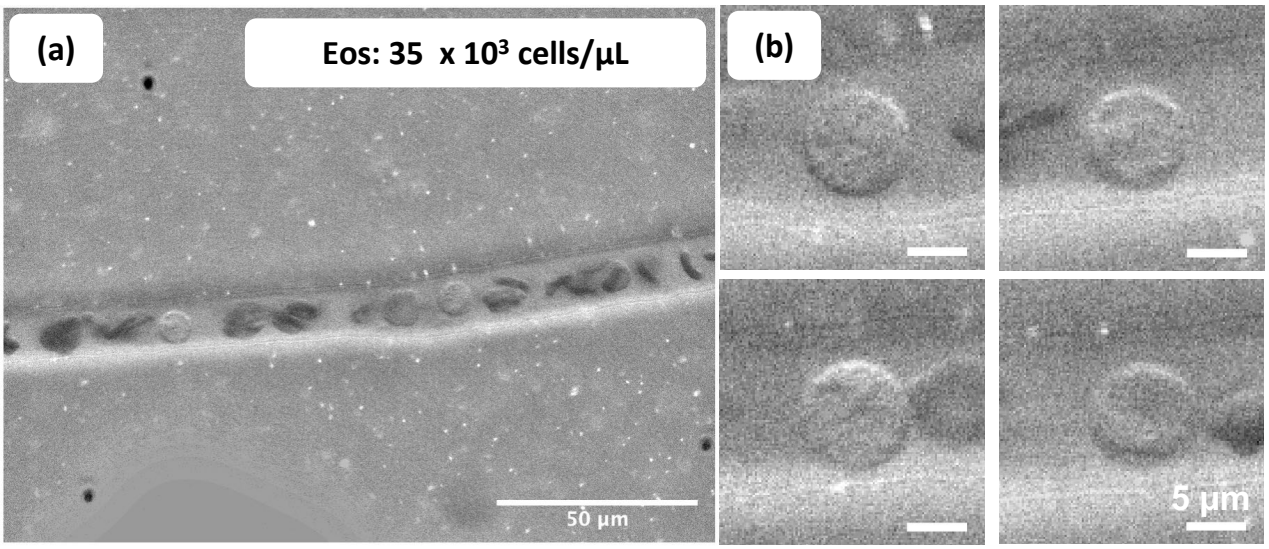

Figure 3-15. (a) A patient with severe eosinophilia shows a remarkable number of white blood cells with sub-cellular granules.

Platelets

While red blood cells and white blood cells are readily distinguished from each other using hemoglobin's absorption contrast, platelets are similarly transparent to leukocytes. Thus, the phase contrast of OBC should render them visible in the microfluidic chambers, especially given the system resolution is sufficient to resolve their smaller size. Figure 3-16 shows the results from imaging three samples with a wide range of platelet concentration. Unfortunately, the thrombocytopenic case in Figure 3-16(a) is indistinguishable from the thrombocytosis present in Figure 3-16(b). Despite a 900-fold increase in platelet concentration, the two different samples look largely the same. Platelets are difficult to see when crowded by red blood cells in normal whole blood. However, in the case of Figure 3-16(c), in the setting of a myeloproliferative disorder, the severe anemia accompanying the thrombocytosis enables viewing numerous platelets within the gaps between red blood cells. Thus, while OBC is capable of spatially and temporally resolving platelets, their small size and encircling red blood cells obscures them from view. OBC in its current form is likely to have difficulty acting as a non-invasive platelet concentration counter, and other sensing capabilities may have to be added in addition to the phase and absorption contrast to detect platelets in

whole blood reliably.

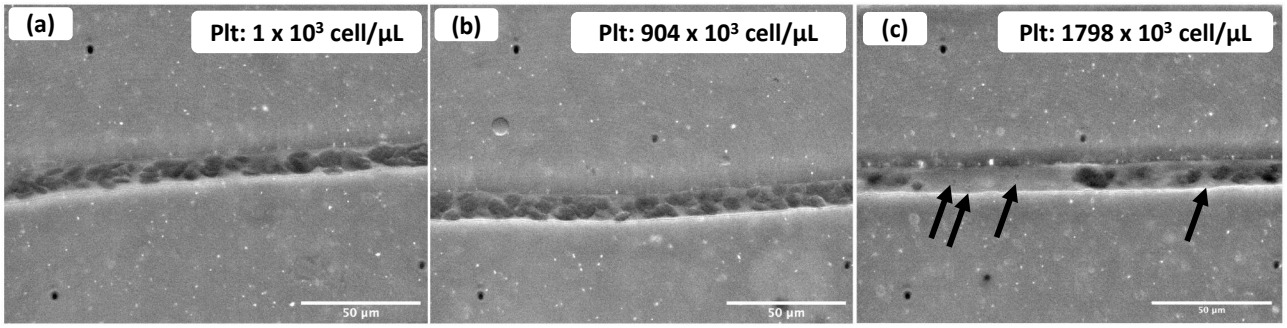

Figure 3-16. (a) Severe thrombocytopenia is difficult to discern from (b) thrombocytosis in whole blood without anemia. (c) The presence of thrombocytosis along with anemia provides an opportunity to visualize numerous platelets (arrows) in the gaps between red blood cells.

Blood cell isolation experiments

Manual counting and analysis of blood cells is impractical for widespread adoption of OBC. Deep learning algorithms that enable video instance segmentation, classification, and counting are suitable candidates to enable automated analysis. However, while many deep learning architectures exist that can accomplish the required tasks, they must be retrained with ground truth labeled OBC data in order to work for blood cell imaging. Developing ground truth labels by imaging blood cells *in vivo* in humans is prohibitive due to the inability to add cellular labels or fluorescent dyes non-invasively and safely. The tissue-mimicking microfluidic chambers developed in this chapter offer a compelling alternative.

In the previous sections, whole blood from humans with ground truth complete blood counts or clinical hematologic diagnosis were imaged in the microfluidic device with OBC. While many of these cases are compelling and exciting, developing a robust algorithm for accurate cell classification requires first knowing what each individual cell type looks like. Thus isolating and imaging individual human blood cells with ground truth labels would provide the basis of this dataset. While this can be accomplished in several ways, magnetic antibody negative-selection kits offer a label-free method of isolating individual blood cell classes with minimal tampering of their native state. The individual classes of white blood

cells can be separated from whole blood and imaged in the microfluidic chambers (Figure 3-17). Example images from these experiments are shown in Figure 3-18, where neutrophils, lymphocytes, monocytes, basophils, and eosinophils are each shown column-wise under their respective labels.

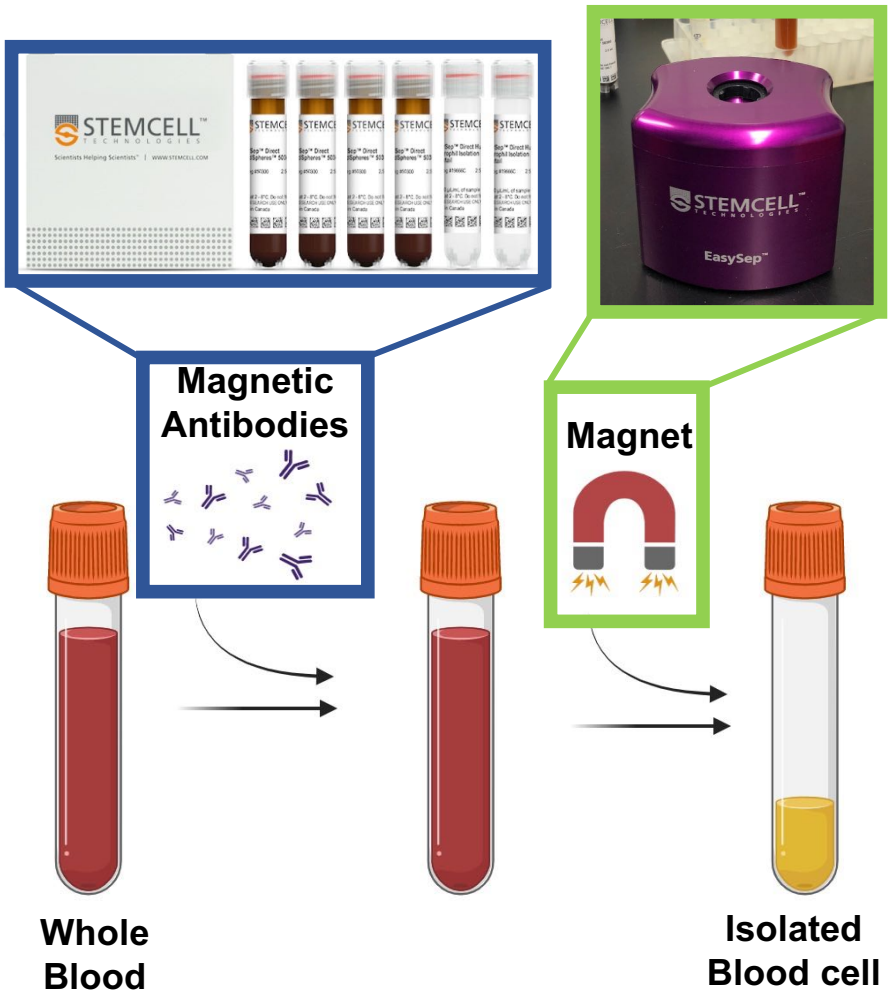

Figure 3-17. Whole blood can be processed with magnetic antibody negative-selection kits in order to isolate specific blood cell types for ground truth labeling.

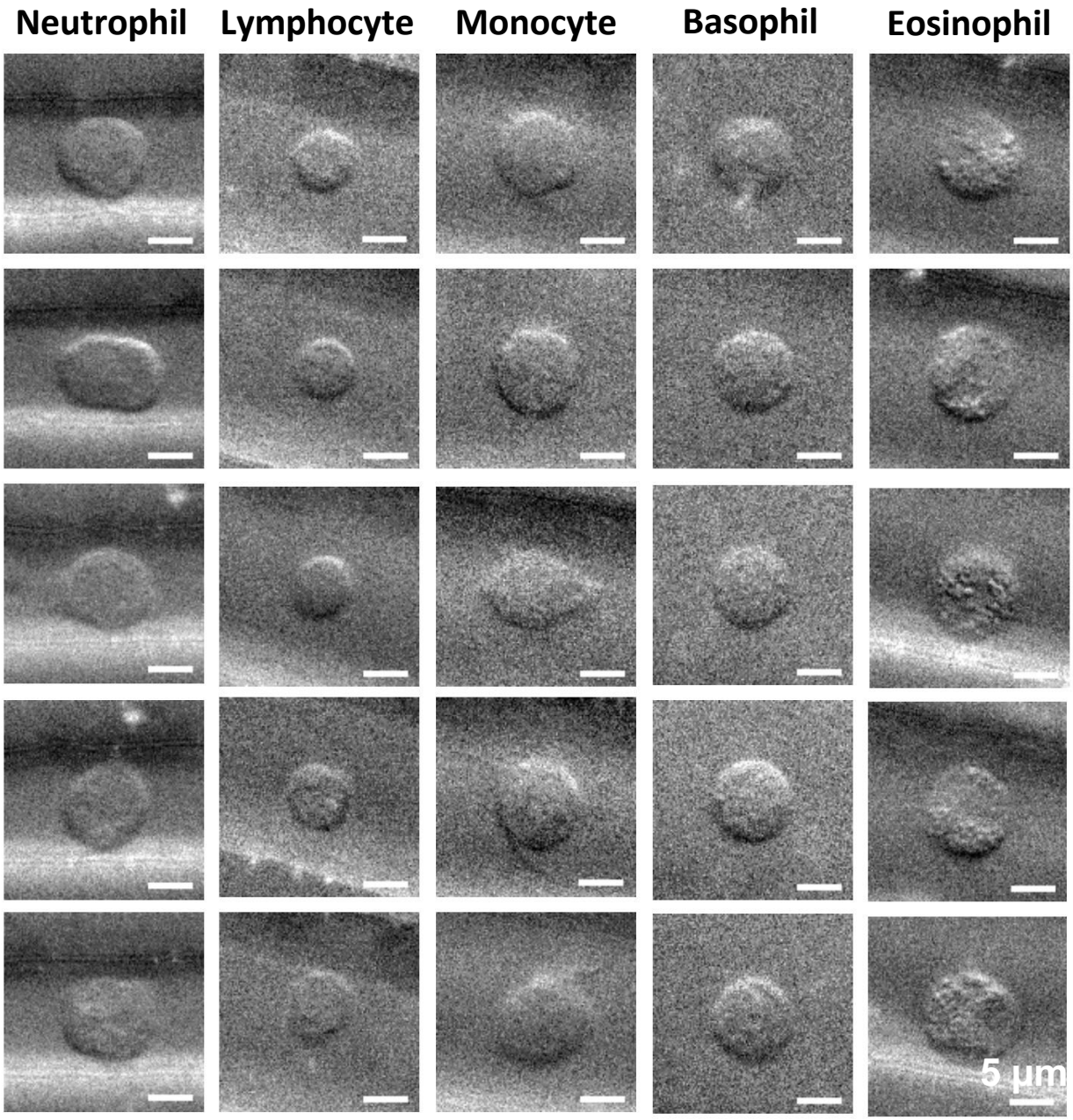

Figure 3-18. Magnetic negative selection antibody kits can be used to isolate the five white blood cell classes of a CBC with differential for generating ground truth training data. Each cellular label applies to all cells within a column beneath it.

Discussion

Oblique back-illumination capillaroscopy has the potential to disrupt the conventional workflow of blood cell analysis by providing a window into *in vivo* blood cell activity. However, the novel technology introduced here faces a mature field of blood analysis that has been developed over decades. Automated hematologic analyzers generate blood cell counts in mere minutes, and blood smears with finely tuned stains, complex slide scanning microscopes, and computer vision algorithms provide precise and critical information to hematologists efficiently. In order to realize the full potential of OBC as a translational tool, automated cell analysis is crucial, which will likely take the form of deep learning-based algorithms tailored to video instance segmentation, cellular tracking, classification, and morphological assessment. To train these algorithms, an accurate *in vitro* model of *in vivo* vasculature and blood flow is crucial, given challenges associated with developing sufficient ground truth labels in humans.

This chapter introduced a tissue-mimicking microfluidic device that matches human optical properties, index of refraction, capillary depth, vessel dimensions, and blood flow velocities. Using this device, the OBC system phase contrast was optimized to white blood cells by varying the source-detector axis separation in Figure 3-4. An optimized $\delta x = 280$ μm was observed, which showed a similar result to the phase-only lipid particle of Figure 2-5, where a source-detector axis separation of approximately $\delta x = 250$ μm in object space yielded optimum phase contrast. Further, as predicted from the seminal OBM paper, phase contrast steadily degrades with increasing imaging depth through scattering media (Figure 3-5). Given the anatomical survey conducted in the Introduction (Chapter 1), OBC is unlikely to work in the nailfold capillaries, whose depth are typically 150-400 μm (Figure 1-16). However, it should succeed in providing phase contrast that highlights white blood cells and platelets *in vivo* in the oral mucosa capillaries.

The microfluidic devices shown here can be used to study ground truth examples of hematologic disease such as anemia (Figures 3-7, 3-8, and 3-9), sickle cell disease (Figures 3-11

and 3-12), leukemia (Figure 3-14), and thrombocytopenia (Figure 3-16). This approach can yield insight into disease processes with an efficient *in vitro* model, allowing many different hematologic disorders to be easily screened by imaging *ex vivo* blood drawn for standard clinical care to learn which will be most suitable candidates for OBC imaging *in vivo*. For example, while anemia, SCD, and leukemia show tremendous promise for OBC and should be studied *in vivo*, platelet imaging in Figure 3-16 proved more challenging, and it is likely that OBC alone cannot achieve accurate platelet counts.

To train deep learning algorithms for cell classification, ground truth cellular labels must be generated. The microfluidic devices presented here provide a suitable model for this when combined with blood cell isolation procedures. Figure 3-18 shows the results of isolation experiments, where individual classes of leukocytes are isolated using antibody negative-selection kits. A few interesting results emerge from these experiments. First, while all granulocytes do show some sub-cellular features, it is clear that the eosinophil granules are most readily visible in the system. The reason for this is not entirely clear, however recalling the crystalline structure of eosinophil granules discussed in Chapter 1 and shown in electron microscopy in Figure 1-9, it could be that their higher index leads to more pronounced refraction of the incoming oblique light. More work should be done to investigate the effect of the oblique incident angle, system numerical aperture, and other methods of structured illumination to determine if a modification of OBC can be made to highlight neutrophil and basophil granules with similar clarity. Lymphocytes appear as small, relatively uniform cells, as expected. Their morphology is similar to the example of chronic lymphocytic leukemia imaged in Figure 3-14. Monocytes also appear more uniform than granulocytes, but are much larger in size than the lymphocytes and demonstrate cellular projections growing from their soma. These are likely due to the activation of monocytes and their transition into macrophages after removal from the intravascular space. While the use of a negative selection antibody kit as opposed to a positive selection protocol should minimize the activation of the white blood cells under study, it may be that faster phlebotomy-to-image times are required

to study monocytes before they undergo morphological changes.

Thus, the microfluidic model shown here will be an essential tool for generating training data for OBC and for performing system optimization. It provides a good general model of microvascular blood flow and tissue optical properties that could be applied to any imaging technology in need of a capillary model. However, despite improvement over other designs in literature, there are a few ways in which this model is still not a perfect representation of *in vivo* vasculature. Its capillary lumen cross section is square (or rectangular), rather than the approximately ellipsoid or circular cross section of an *in vivo* vessel. The microfluidic channels are straight and at a single axial plane, as opposed to the curving capillary structures that often wind laterally and course in-and-out of the axial plane of focus. The use of TiO_2 and india ink to match tissue optical properties works well on a macroscopic scale and does provide oblique back-scattering in the microfluidic chamber similar to tissue. However, its heterogeneous punctated particles create small, dense, bright regions of scattering in the PDMS that are not directly representative of the scattering structures of tissue. Finally, molecular interactions between endothelial cells and blood cells such as leukocyte adhesion are a critical phenomenon to study with *in vivo* OBC. This is not currently possible in the microfluidic model as the capillary lumen is made of PDMS rather than endothelial cells. Collaboration in the space of cell and tissue engineering to line the PDMS with endothelial cells or even replace the PDMS with a 3D cell culture could yield more realistic microfluidic models. Thus, while the microfluidic chambers provide a good model of human vasculature for controlled OBC studying, there are further developments that can be made to optimize their realistic nature. Regardless, in the next chapter, OBC will be applied and tested for human blood cell imaging *in vivo*, which is the ultimate test of the technology's translational imaging capability.

Chapter 4

A portable oblique back-illumination capillaroscope for human capillary imaging.

Introduction

In previous chapters, OBC was applied to *in vitro* models, where, using both lipid phantoms and custom microfluidic chambers, it was shown to produce small source-detector separations that could resolve human blood cells in bulk scattering media with epi-illumination. While these results are promising, the true test of OBC's potential as a translational tool is its ability to resolve blood cells *in vivo* in humans.

Imaging human capillaries with OBC poses new challenges as compared to the *in vitro* model. According to the scattering depth experiments shown in Figure 3-5, OBC phase contrast is not predicted to work effectively unless the capillaries are < 100 μm deep from the tissue surface. Further, melanin in the peripheral skin degrades absorption and phase contrast. In Chapter 1, these anatomical constraints were considered in detail, and it was determined that the oral mucosa, specifically the ventral tongue, provides an optimal window to imaging human vasculature (Figures 1-16 and 1-18). However, along with the promise of this anatomical location for *in vivo* blood cell imaging comes unique challenges. Mainly, the ventral tongue capillaries reside in the recess of the oral cavity and are more difficult to

reach than, for example, the nailfold capillaries. Further, the tongue is a highly muscular and mobile tissue, and imaging microscopic blood cells during macroscopic motion is problematic.

In this chapter, the OBC system is applied to *in vivo* human blood cell imaging. Special consideration is given to the above challenges, and an inverted, portable, ergonomic OBC system is adapted to an ophthalmic slit lamp housing to enable comfortable, stable positioning of the human head during imaging. To further stabilize the tongue capillaries, a custom pneumatic tissue stabilization cap is developed around the housing of the microscope objective. With these modifications, OBC demonstrates similar contrast to blood cells regardless of skin type. The human blood cells are observed with remarkable clarity in their native environment, including red blood cells, white blood cells, and platelets. Numerous interesting phenomena such as leukocyte adhesions, red blood cell deformability, and pulsatile flow at the microvascular level are observed.

Materials and Methods

Portable and ergonomic OBC system

A schematic of the dual-channel, portable OBC system is shown in Figure 2-2. The OBC system was adapted to an ophthalmic slit lamp housing that enables fine 3-axis translation and comfortable positioning of the head during imaging, shown in Figure 4-1. Two LEDs (Luxeon Star Saber Z4, 530nm and 640nm) are collimated by a 12mm focal length condensing lens (Thorlabs ACL1512U-A) and critically imaged into a capillary bed by a reverse pass through the microscope objective (Nikon Plan Fluor 20x / 0.75 MImm DIC M Oil Water Glycol). Back-scattered light is collected by the microscope objective and reflected off a non-polarizing 50:50 beamsplitter (Thorlabs CCM1-BS013). A tube lens (f = 200 mm) focuses the signal from the red and green LEDs onto two different CMOS sensors (The Imaging Source DMK 33UX252), separated by a dichroic mirror (Thorlabs DMLP605R). The CMOS sensors are synchronized for simultaneous acquisition across the two illumination channels

using a hardware trigger controlled by an Arduino Uno. Images were acquired using 1ms exposure time at 200 Hz. The slit lamp housing itself is affixed to a clinical cart on caster wheels with a motorized height adjustment.

Pneumatic stabilization

A custom, pneumatic objective cap was designed in Solidworks and 3D printed in aluminum to surround the microscope objective (Figure 4-2. This cap contained eight suction ports, equally spaced every 45 degrees about a 21 mm diameter circle around a coverslip collar. The correction collar of the microscope objective was set to 150 μm for use with 12 mm diameter #1 thickness coverslips. The imaging depth of the microscope was tuned to match the depth of the superficial capillaries by manually threading the coverslip collar up and down within the objective cap. A vacuum was connected to these ports using 1/16" ID PVC tubing connected to two straight flow rectangular manifolds with barbed tube adapters (McMaster-Carr 5233K51, 1023N13, and 4406T15, respectively). Pressure was increased slowly to stabilize capillaries without causing pain or tissue damage. The application of suction can be triggered on and off by a circuit controlling a solenoid (Beduan 2-Way Normally Closed 1/8" NPT EVI 7/9 12V DC).

Figure 4-1. The portable OBC system is built on an ophthalmic slit lamp housing for ergonomics with an inverted setup for ventral tongue imaging.

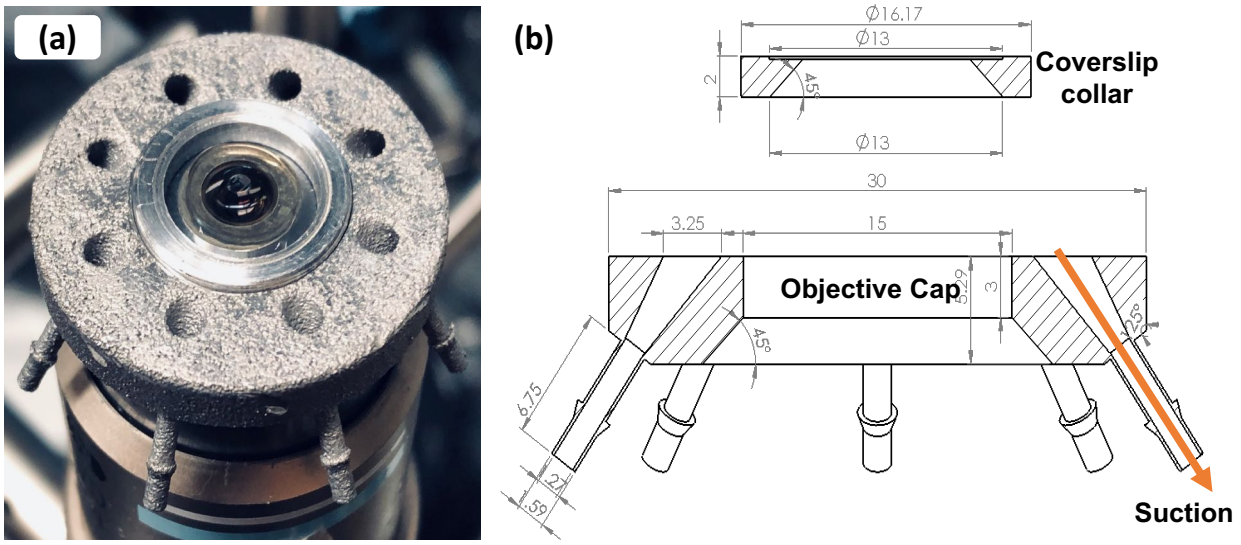

Figure 4-2. (a) The pneumatic stabilization cap is a custom aluminum housing surrounding the microscope objective that enables suction to be applied symmetrically to the tongue surrounding the capillary.

In vivo human blood cell imaging

Imaging data was collected on healthy human participants under a Johns Hopkins University IRB approved protocol (IRB00204985). To optimize phase contrast to blood cells *in vivo*, images of a single capillary were taken with the single-source OBC system with the LED imaged critically on-axis, and the detector offset 208 μm (half of the FOV of the detector in object space) such that the peak intensity of the gradient field was conjugate to the edge of the sensor (Figure 2-1(c)-(d)). A video was acquired at 50 Hz of the same capillary as it was laterally translated from left to right across the field of view, while keeping the LED and sensor position fixed. The phase contrast between adjacent, stacked red blood cells at different distances across the FOV was measured using Weber contrast ($C_W = (I_{max} - I_{min})/I_{min}$), calculated from plot profiles taken across the cells in the direction of the illumination-detection offset. Though phase contrast is most useful in imaging white blood cells, since these are rare, heterogenous, and difficult to visualize in the absence of phase contrast, the contrast

of the plasma membrane between adjacent, stacked red blood cells was measured instead in order to characterize phase contrast over a range of illumination-detection separations (Figure 4-3). Three individuals were enrolled for imaging, with Fitzpatrick skin phototypes II, IV, and VI. Images of blood cells (Figure 4-4) were selected from videos acquired at 200 Hz and 500 μs exposure time. Images of participants with different skin tones (Figure 4-5) were acquired at 50 Hz and 500 μs.

Results

Single-source OBC *in vivo* phase contrast optimization

With the pneumatic objective cap turned off, a video was acquired of a single capillary in the ventral tongue of a human volunteer as it was swept laterally across the full FOV (Figure 4-3(a)-(c)). The plasma membrane of red blood cells appeared visible only from absorption contrast when the capillary was near the illumination axis (Figure 4-3(d)), and phase contrast was at a maximum near the center of the FOV (Figure 4-3(e)). Plot profiles across adjacent, stacked red blood cells show the improvement of phase contrast as the target is moved away from the peak illumination (Figure 4-3(f)). The Weber contrast between overlapping red blood cells was measured at known capillary distances across the FOV (Figure 4-3(g)). Phase contrast was maximized at approximately 200-250 μm, regardless of whether the contrast was calculated with raw or flat field corrected data.

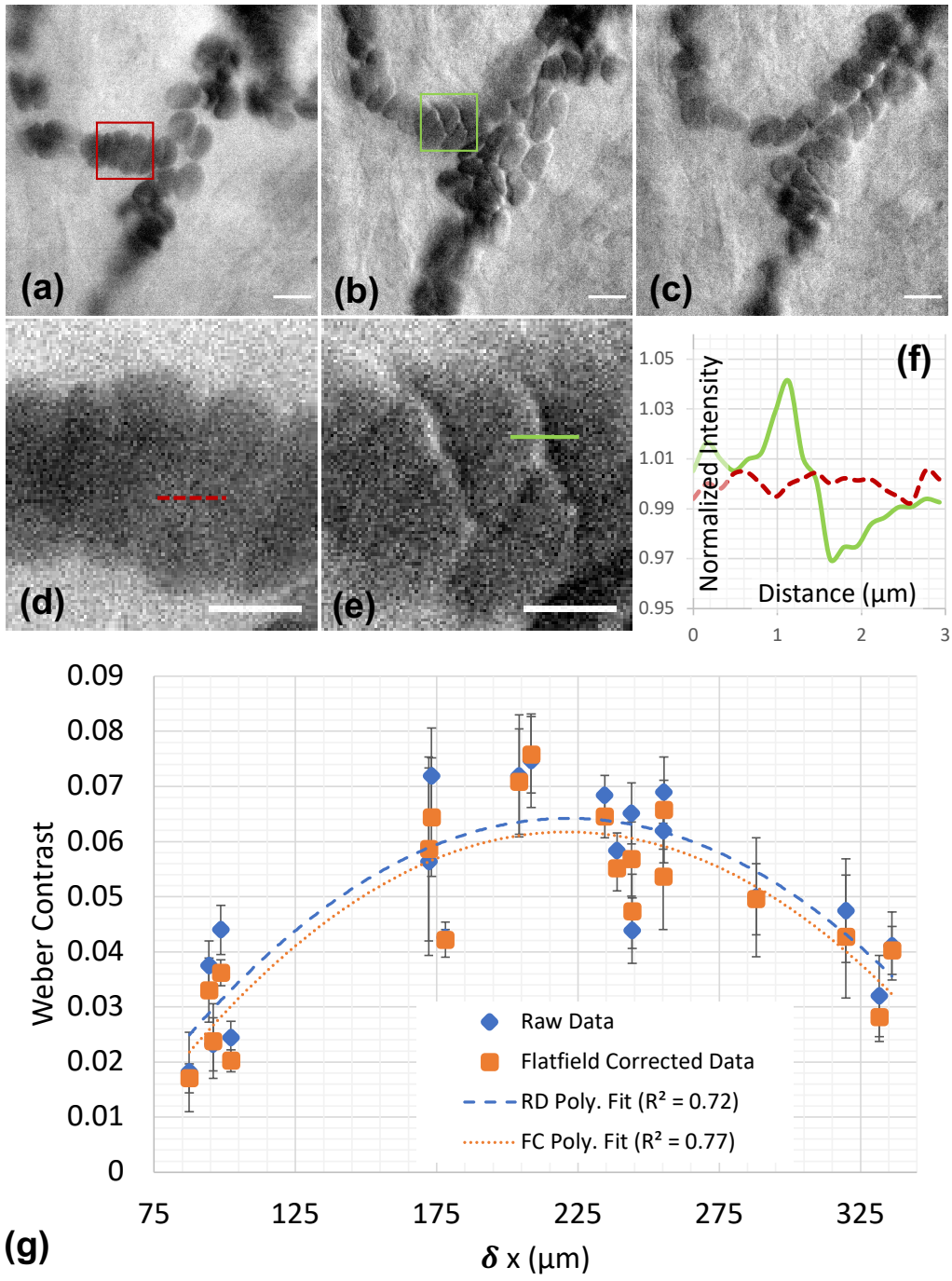

Figure 4-3. Imaging a single capillary translated across the full FOV to vary source-detector separation (δx). (a) Red blood cells close to the intensity peak (small δx) demonstrate only absorption contrast, (b) phase contrast is maximized near the center of the full FOV (δx = 200 - 250 μm), and degrades due to low signal at large displacements, (c). (d) & (e) Enlarged regions of interest (15 x 15 μm) at locations of minimum and maximum phase contrast, respectively, with example normalized intensity plot profiles shown for each, (f). (g) Overall trend of phase contrast vs. δx demonstrates highest contrast at approximately 200-250 μm illumination-detection separation. Scale bars 10 μm (a)-(c) and 5 μm (d)-(e).

Single-source OBC *in vivo* blood cell imaging

Both the single-source (Figure 2-1) and dual-source (Figure 2-2) OBC systems were used to image capillaries *in vivo* with pneumatic stabilization. Blood cells flowing through a variety of vessel sizes are spatially and temporally resolved clearly. Some representative images of different blood cells observed are highlighted in Figure 4-4. As expected from the green illumination, red blood cells are visible with combined phase and absorption contrast. Their bi-concave discoid structure is clearly resolved (Figure 4-4(a)-(b)). White blood cells are also clearly visible, however are only highlighted with phase contrast due to weak absorption at the visible wavelengths used (Figure 4-4(e)-(l)). Importantly, not only can the size of white blood cells be established from these images, but sub-cellular granules are clearly visible in some white blood cells, while absent in others. Despite difficulty observing them with the *in vitro* microfluidic devices, platelets are also clearly visible as small discs with the characteristic gradient phase contrast provided by the oblique illumination (Figure 4-4(b)-(c)). The impressive resolution of OBC is fully realized by its ability to resolve a lipid particle, roughly only 600 nm in diameter flowing through the capillary (Figure 4-4(d)). Not only are blood cells visible, but the boundary of the capillary lumen and features of the peripheral skin are clearly visible. The characteristic intercellular junctions (desmosomes) of the stratum spinosum are observed surrounding the capillary, as expected if the capillary is contained within a dermal papilla.

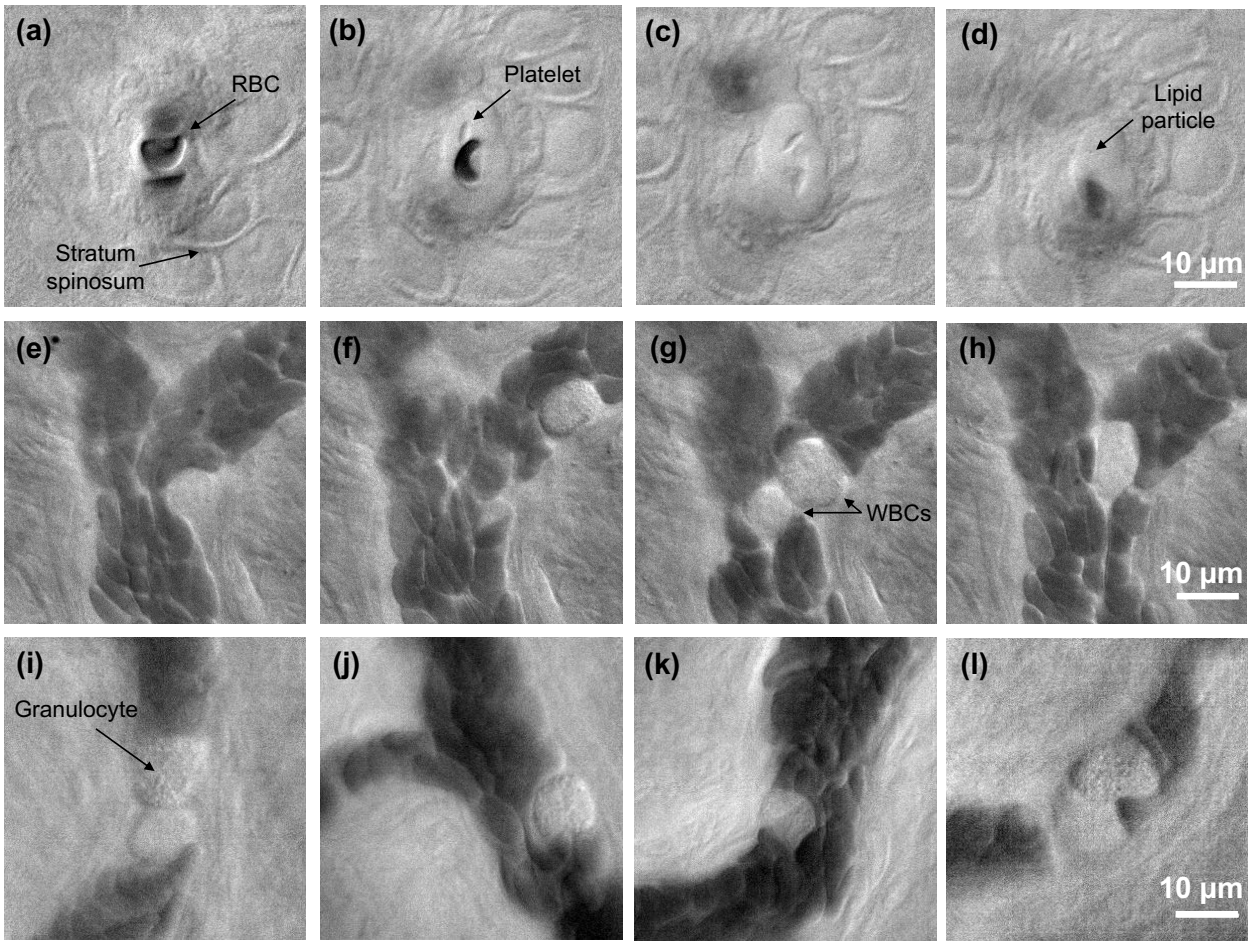

Figure 4-4. Imaging blood cells flowing through microvasculature with the single-source OBC system shows clear resolution of red blood cells, white blood cells, platelets, and even small lipid particles (potentially a chylomicron). Sub-cellular granules present within the white blood cells are clearly visible along with intercellular junctions of stratum spinosum in the surrounding skin.

One of the main predicted advantages of OBC imaging in the oral mucosa is its ability to resolve blood cells regardless of Fitzpatrick skin phototype. Unlike nailfold capillaroscopy, where increased melanin degrades absorption contrast, oral mucosa imaging provides a window to capillaries with minimal melanin regardless of skin type. This hypothesis was tested by imaging the blood cells of three human subjects with Fitzpatrick skin phototypes II, IV, and VI, results of which are shown in Figure 4-5. Similar appearing blood cells from superficial capillaries were selected and analyzed using intensity profiles across the direction of LED displacement, which showed similar combined phase and absorption contrast (Figure 4-5(d),(h)) regardless of skin phototype.

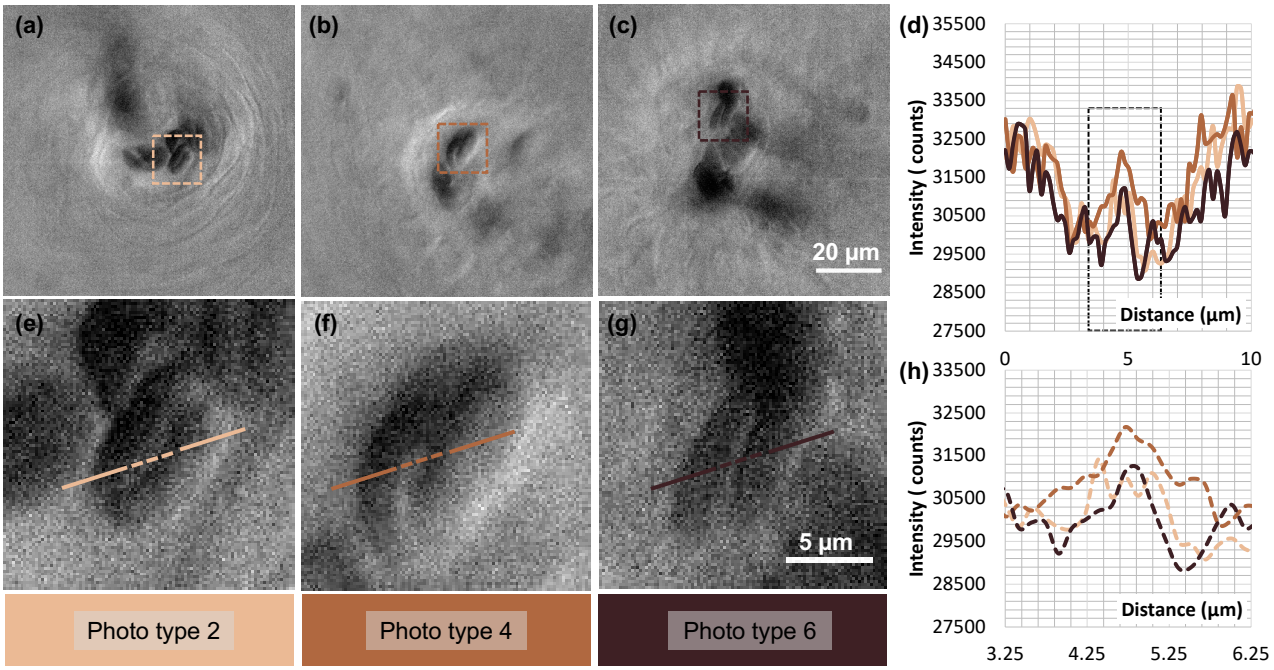

Figure 4-5. Imaging blood cells flowing through a capillaries of humans with different Fitzpatrick skin phototype shows similar contrast to red blood cells.

Dual-source OBC *in vivo* blood cell imaging

While the single-source OBC system with its higher power 40X, 1.15 NA microscope objective provides impressive detailed images of blood cells, the dual-source OBC system provides a more robust imaging device with its wider field of view. The dual-source OBC system was applied to imaging human ventral tongue vessels, and representative images of ventral tongue microvasculature observed in this system are shown in Figure 4-6. The use of the 20X objective in the dual-source system enables viewing a long stretch of the same vessel, allowing the same blood cells to be tracked as they course along its 250 μm length. Despite the wide field of view, the system is still capable of high imaging speeds and combined phase and absorption contrast due to the use of the two CMOS sensors and corresponding diametrically opposed illumination sources. As expected, the red 640nm illumination produces primarily phase-only information (Figure 4-6(a)) due to minimal absorption of biological tissue at this wavelength, while the green 530nm illumination shows red blood cells as darkened shadows

from hemoglobin's absorption.

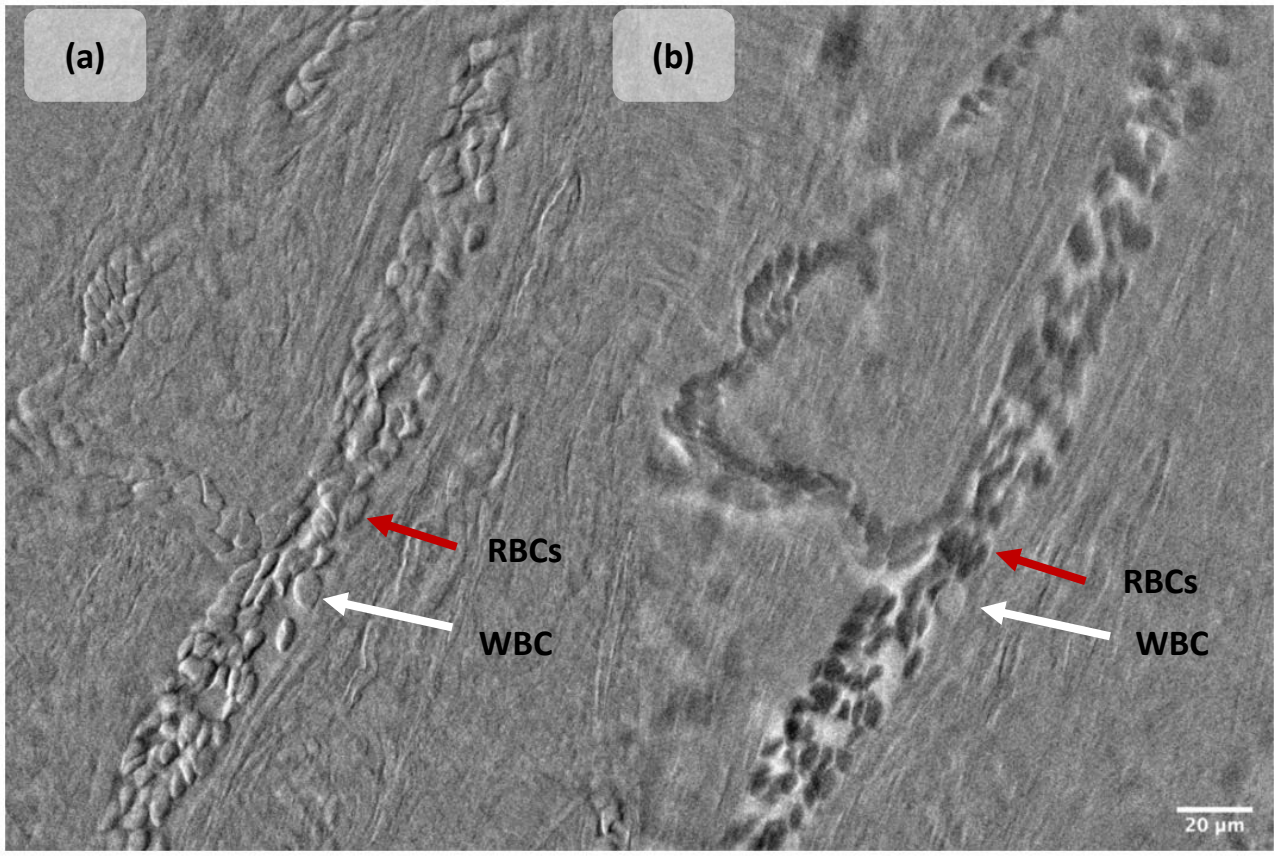

Figure 4-6. The dual-source, portable OBC system provides high speed, wide field of view imaging of a large vessel. A leukocyte can be seen during adhesion to the endothelial cell wall (WBC, white arrow).

The ergonomic combination of the ophthalmic slit lamp house, adjustable table, and pneumatic tissue stabilization enable imaging the same blood vessel longitudinally. With this setup, a large number of superficial capillaries and vessels with varying dimensions and morphology are visible with the OBC system. Examples of this are shown from the red channel in Figure 4-7.

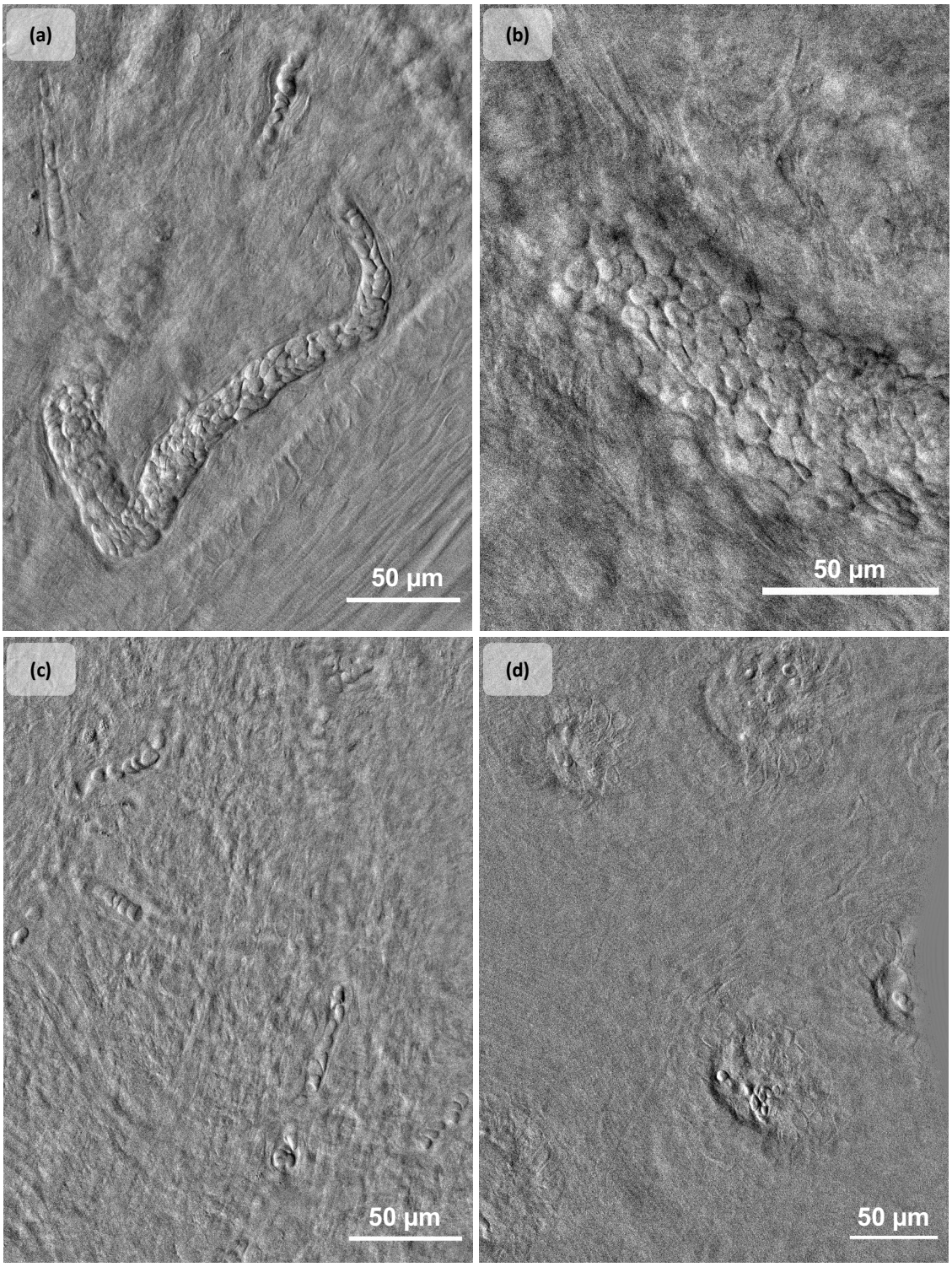

Figure 4-7. Blood vessels with varying size (10-50 μm diameter) and morphology are visible with the portable OBC system and 640nm illumination.

Observations of leukocytes and optical absorption gaps

The longitudinal imaging capabilities provided by the ergonomics and pneumatic stabilization of the portable OBC system, enable viewing interesting phenomena such as leukocyte adhesion, which is highlighted with a time series in Figure 4-8. This time series progresses left-to-right, top-to-bottom with Δt = 8ms intervals between each panel. Note that the leukocyte (WBC, white arrow) remains stationary, affixed to the vessel wall as red blood cells deform and course around it.

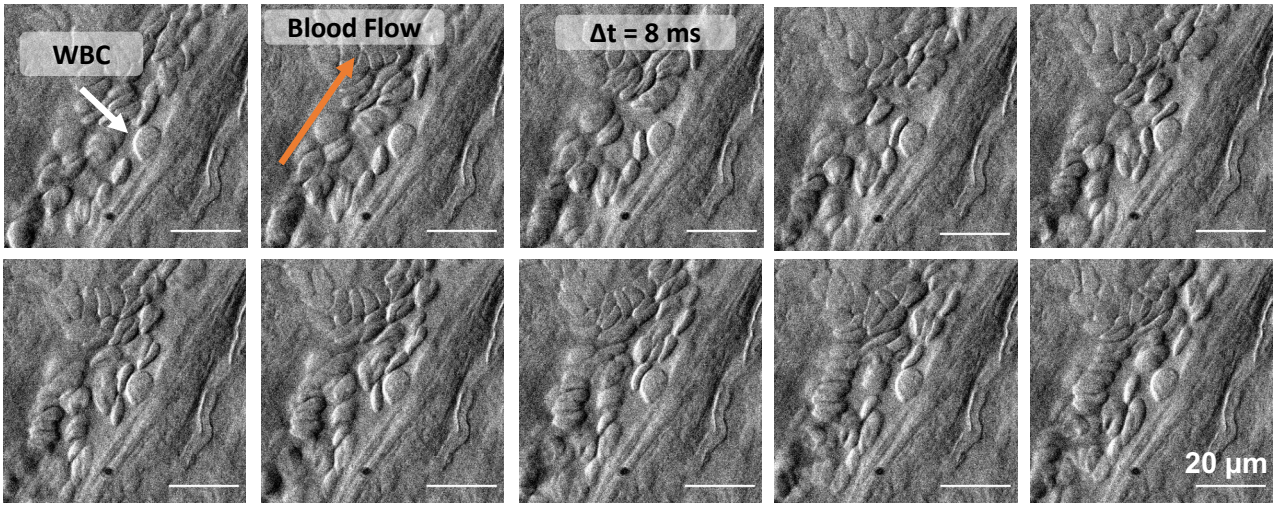

Figure 4-8. Time series showing WBC adhesion during blood flow in a relatively large vessel in the ventral tongue. Note that the WBC highlighted in the top left panel (white arrow) remains relatively stationary on the endothelial cell lining while red blood cells flow around it. Time series progresses left-to-right, top-to-bottom with Δt = 8ms intervals between panels.

Leukocyte adhesion is also visible with green illumination, shown in a different capillary in Figure 4-9. Again, a time series highlights an adhered white blood cell remaining relatively stationary with respect to the red blood cells flowing around it. The white blood cells remains bound to the endothelium for about 500 ms before releasing and flowing out of the field of view. The same phenomena can be observed in even larger vessels, highlighted with the time series of Figure 4-10. Here a leukocyte slows and adheres to the top of a blood vessel approximately 50 μm in diameter. Note that this data was taken with a 590 nm amber light source, and thus the RBC absorption contrast is weaker than the normal 530nm green

illumination. Here the white blood cell binds to the endothelium for approximately 300 ms before releasing and continuing down the vessel.

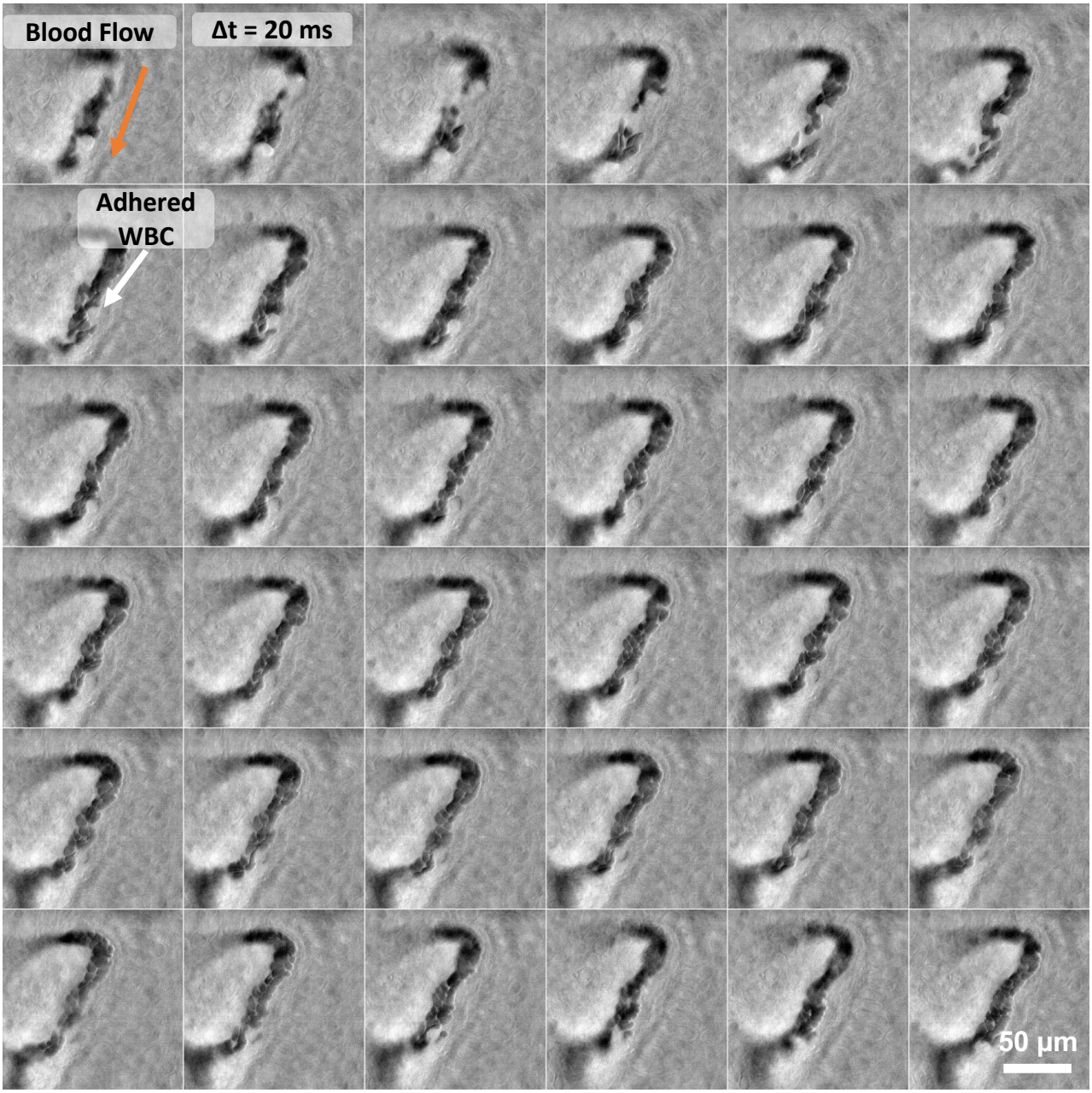

Figure 4-9. Time series showing WBC adhesion with green illumination during blood flow in a relatively small vessel in the ventral tongue. Note that the WBC highlighted in the second row (white arrow) remains relatively stationary on the endothelial cell lining while red blood cells (dark shadows) flow around it. Time series progresses left-to-right, top-to-bottom with $\Delta t = 20$ ms intervals between panels. The white blood cell remains stationary for approximately 500 ms.

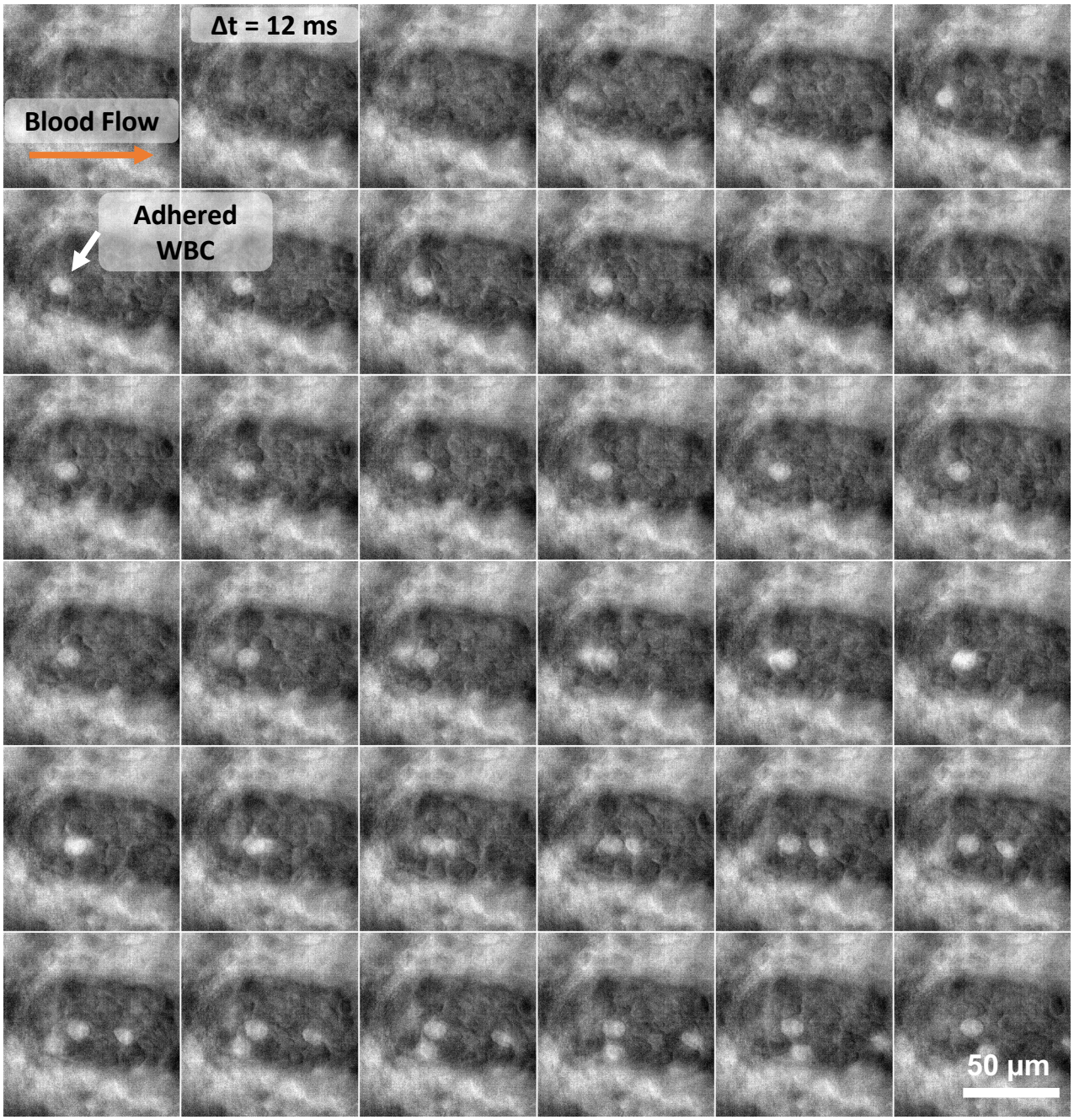

Figure 4-10. Time series showing WBC adhesion with 590 nm illumination during blood flow in a larger vessel in the ventral tongue. Note that the WBC highlighted in the second row (white arrow) remains relatively stationary on the endothelial cell lining while red blood cells (dark shadows) and another leukocyte flow around it. Time series progresses left-to-right, top-to-bottom with Δt = 12 ms intervals between panels. The white blood cell remains stationary for approximately 300 ms.

Importantly, the resolution of optical absorption gaps is clearly accomplished by the phase contrast of OBC *in vivo*. For example, Figure 4-11 highlights a time series of the same capillary showing a resolved white blood cell (top row), and optical absorption gap caused by blood plasma (bottom row). In contrast, in a different capillary loop, a granulated white blood cell creates a preceding plasma optical absorption gap (Figure 4-12). These results highlight the importance of the phase contrast provided by the oblique back-illumination as compared to conventional, absorption-only widefield capillaroscopy in the nailfold, (Figures 1-14 and 1-15). OBC can answer whether or not an optical absorption gap contains a white blood cell, and potentially even what type of white blood cell, while a blood cell counting approach based on conventional capillaroscopy likely would count some absorption gaps as white blood cells when they are simply caused by blood plasma.

Other interesting phenomena of leukocytes was also observed *in vivo*. Despite their relative rarity as compared to red blood cells, it was not uncommon to observe leukocytes traveling in pairs (Figure 4-13). Whether this is just due to stochasticity or due to biochemical adhesion between the leukocytes is unknown. Importantly, despite the difference in magnification and NA between the single-source OBC objective (40X 1.15 NA) and the dual-source OBC objective (20X 0.75 NA), sub-cellular granules in leukocytes are still visible (Figure 4-14). Thus, white blood cell sub-classification may still be possible with the wider field of view, dual-source system despite its reduction in resolution as compared to the single-source OBC system.

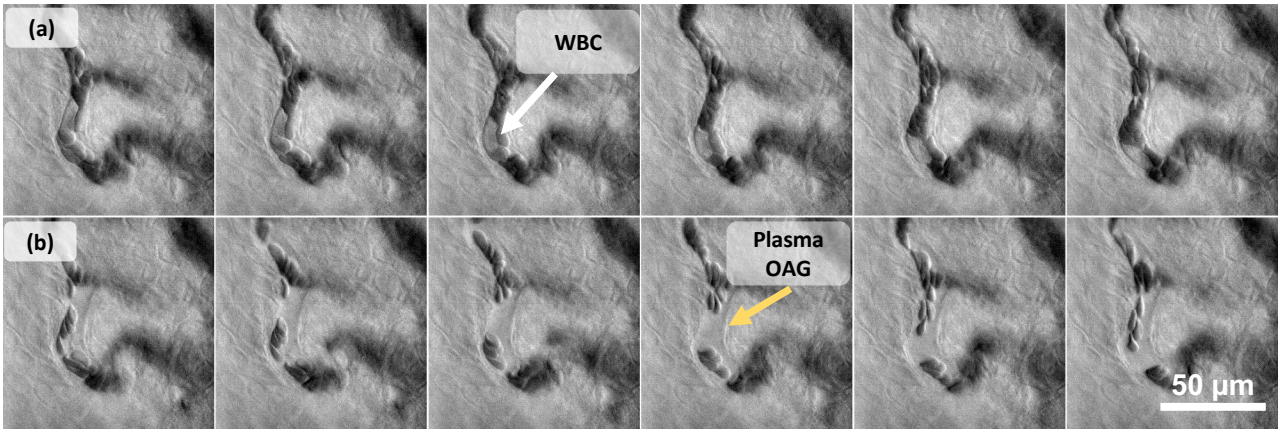

Figure 4-11. Time series showing the ability of OBC to resolve the etiology of optical absorption gaps. The top row shows a granulated white blood cell passing through the capillary loop (top row). Later, in the same capillary, an optical absorption gap comprised of only blood plasma also occurs (bottom row).

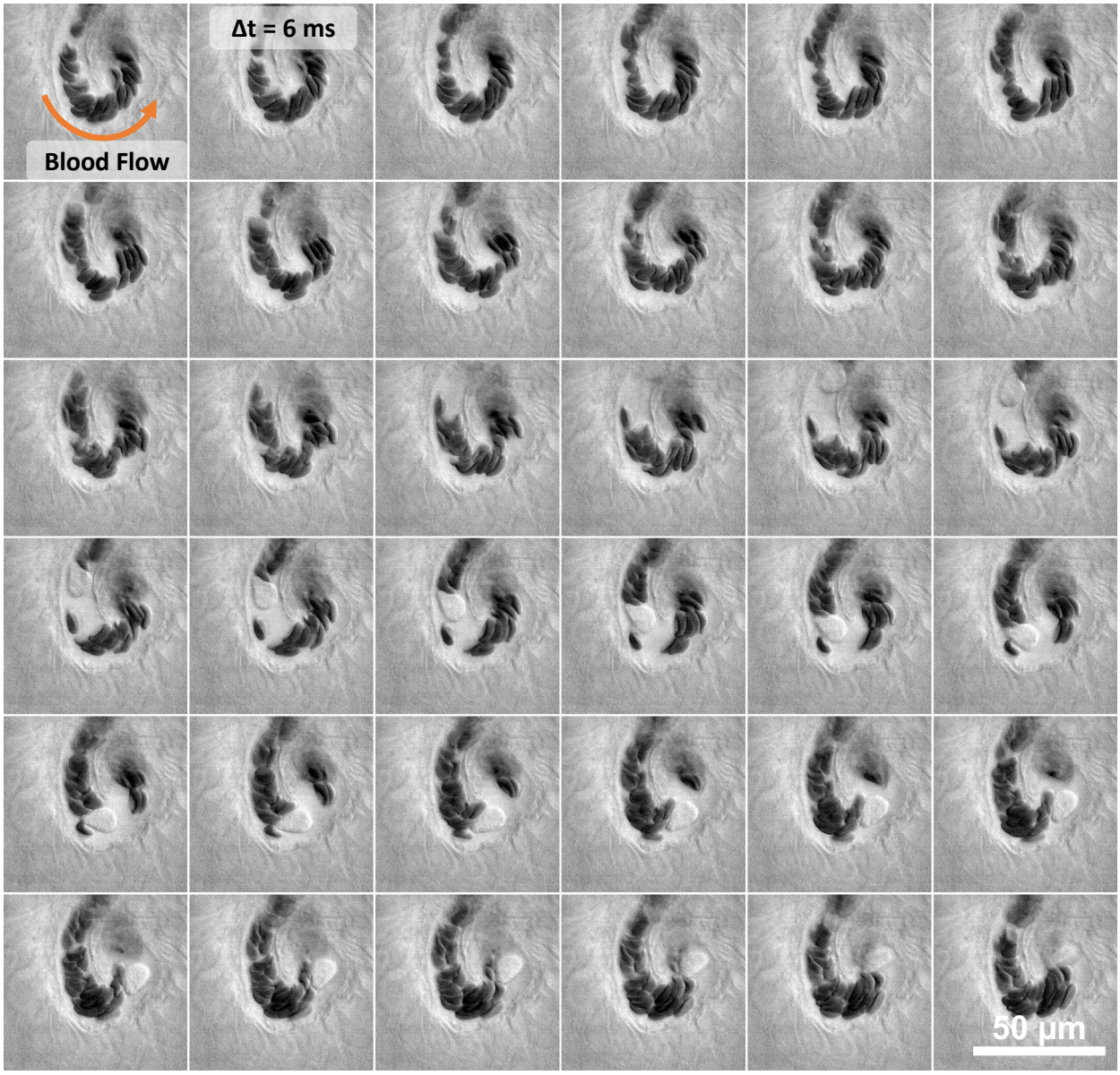

Figure 4-12. Time series showing a granulocyte passing through a capillary loop with a preceding plasma optical absorption gap. Time series progresses left-to-right, top-to-bottom with $\Delta t = 6$ ms intervals between panels.

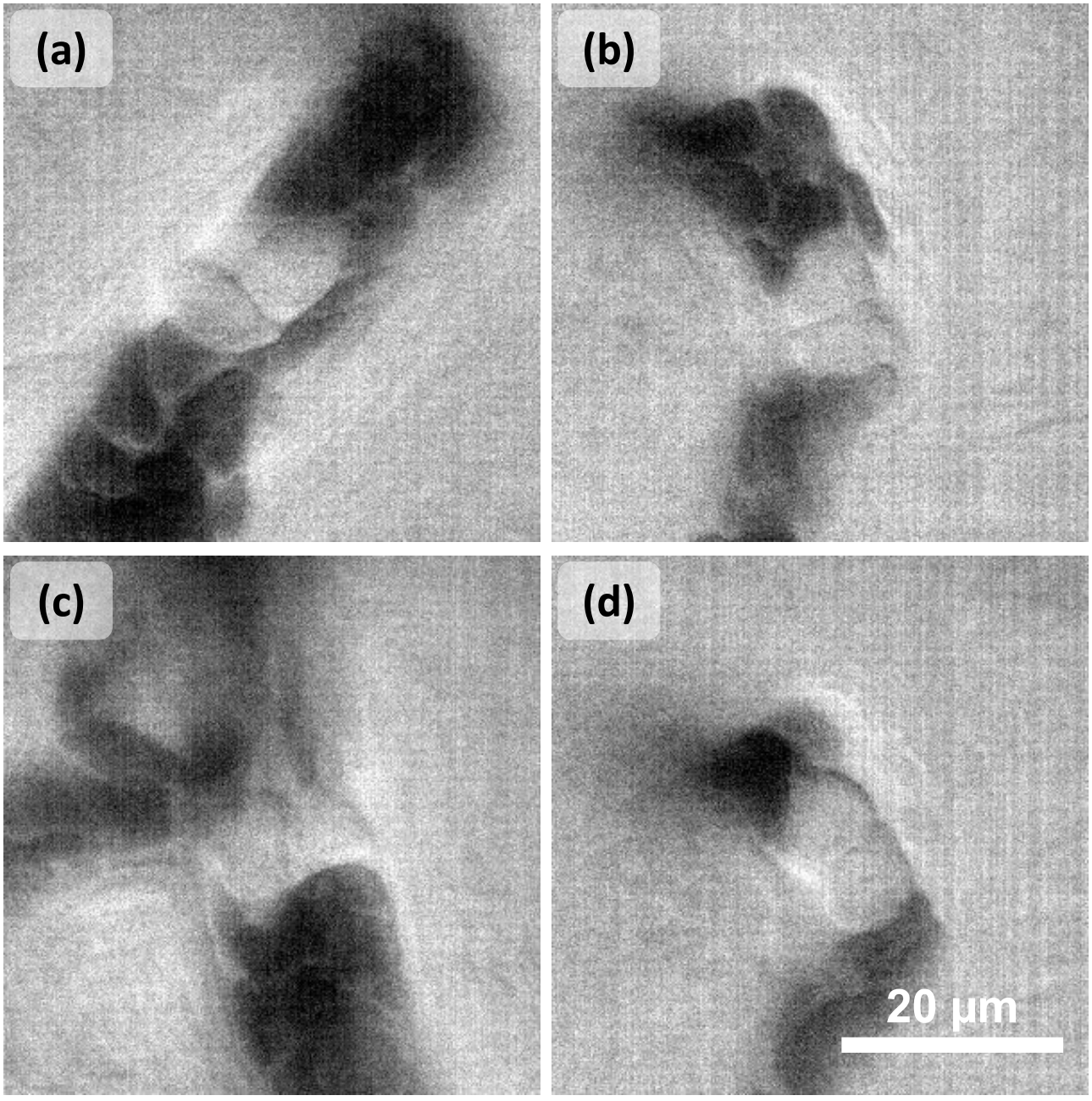

Figure 4-13. Leukocytes pairs were often observed *in vivo*. The significance of this phenomenon is unknown.

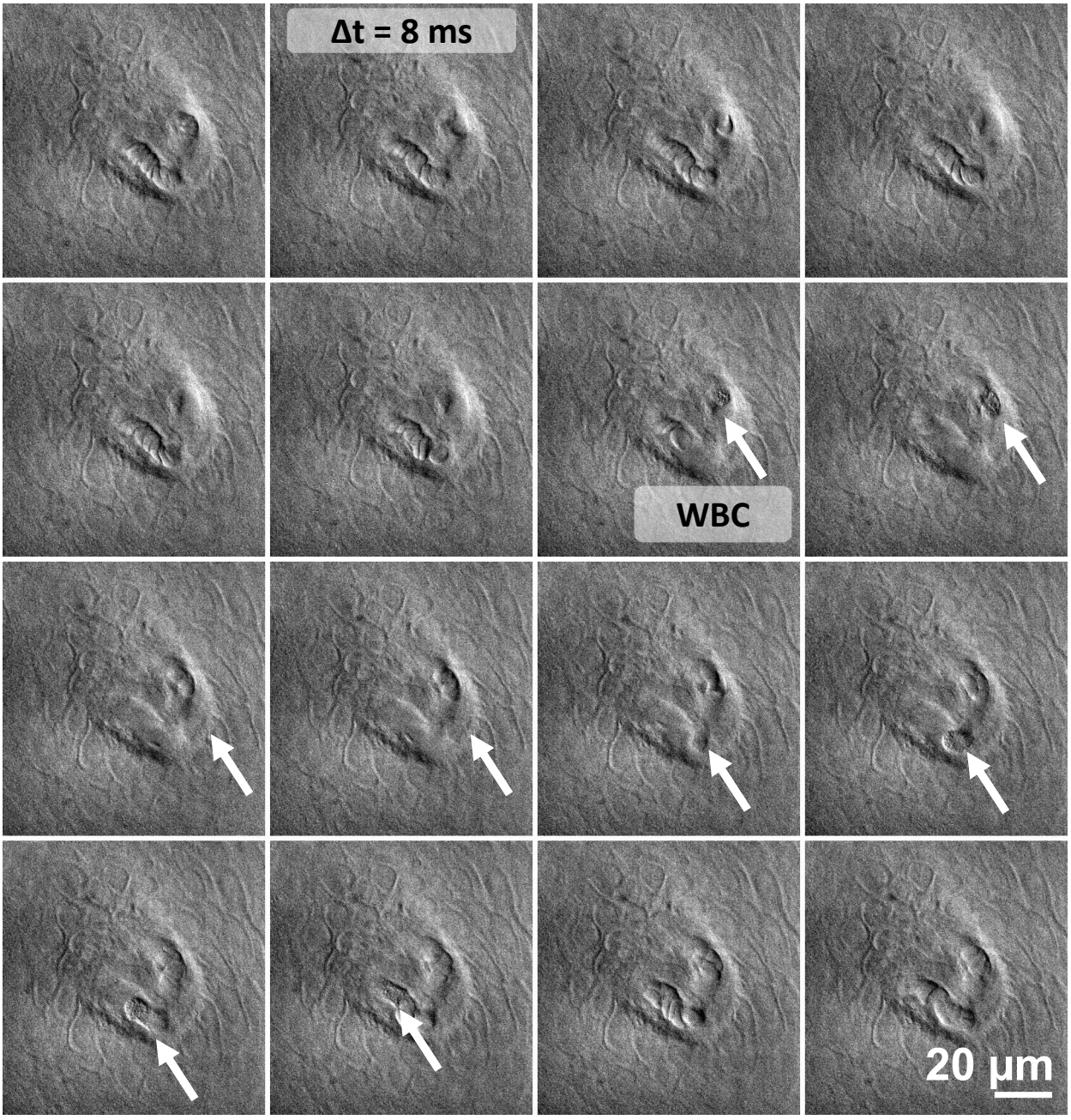

Figure 4-14. Time series showing a granulocyte passing through a capillary loop with dual-source OBC system and 640nm illumination. Note the high visibility of granules despite using the 20X 0.75 NA objective. Time series progresses left-to-right, top-to-bottom with Δt = 8 ms intervals between panels.

Observations of platelets

Despite difficulty observing platelets with the *in vitro* microfluidic model in Chapter 3, platelets were readily visible between red blood cells even without anemia with the single-source OBC system (Figure 4-4(b)-(c)). Platelets are also visible with the dual-source OBC system, examples of which are shown in Figure 4-15 in different vessels from the red channel. This is further evidence that the 20X 0.75 NA objective in the dual-source OBC system is sufficient for resolving the most important cellular features of blood *in vivo*. While issues of red blood cells crowding and obscuring platelets are inevitable regardless of the OBC system used, the additional benefit of wider field of view provided by the dual source-system likely outweighs the cost of losing some resolution.

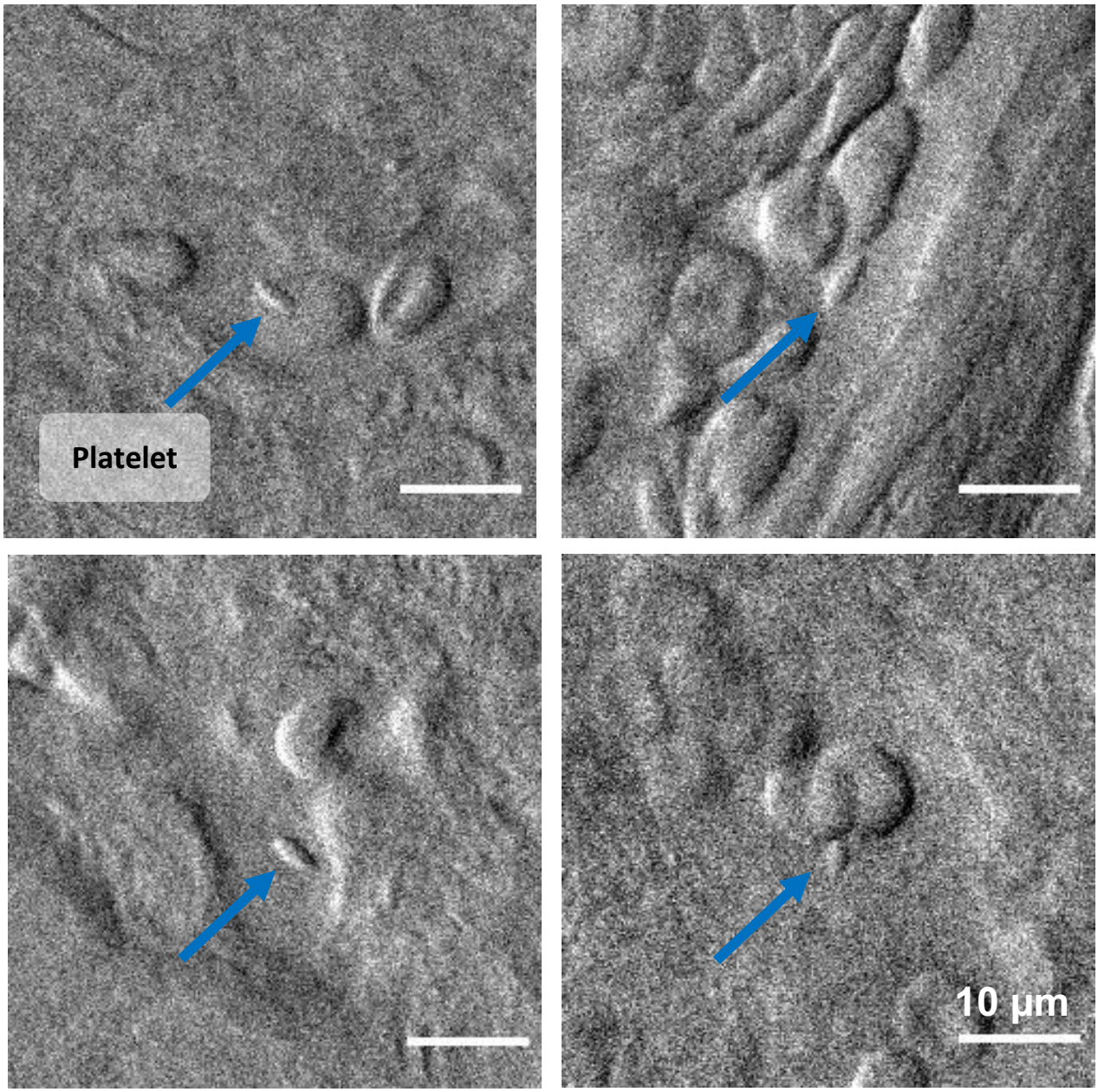

Figure 4-15. Example frames showing platelets passing through capillary loops and blood vessels with dual-source OBC system and 640nm illumination. Note the visibility of these small particles despite using the 20X 0.75 NA objective.

Observations of red blood cells

Red blood cells are enticing to study with OBC due to their abundance compared to other blood cell types. It would easy to image hundreds to thousands of red blood cells in mere seconds with OBC. In Chapter 3, red blood cell absorption, density, size, and shape were shown in microfluidic models as promising avenues for further study *in vivo* of hematologic disease. While thus far only presumably healthy individuals with normal blood cell parameters have been imaged *in vivo*, the longitudinal imaging capability of OBC still shows interesting phenomena of red blood cells. For example, red blood cell adhesion to endothelial cells was observed, highlighted in Figure 4-16 (red arrows). The remarkable capability of a red blood cell to undergo drastic and rapid morphological changes as it flows through a capillary is highlighted in Figure 4-17. Here the same RBC is highlighted in the center of the field of view progressing through a small capillary every $\Delta t = 16$ ms. The RBC changes from a biconcave disk in the first few frames to an elongated ellipsoid by the middle row, and finally returns to the biconcave disk all in about 400 ms. Whether or not these parameters are visibly altered in states of disease *in vivo* are so far unknown. However, RBC adhesion and deformability are important in diseases such as sickle cell, and knowing that the OBC system can resolve them in healthy individuals makes it a promising avenue for future study.

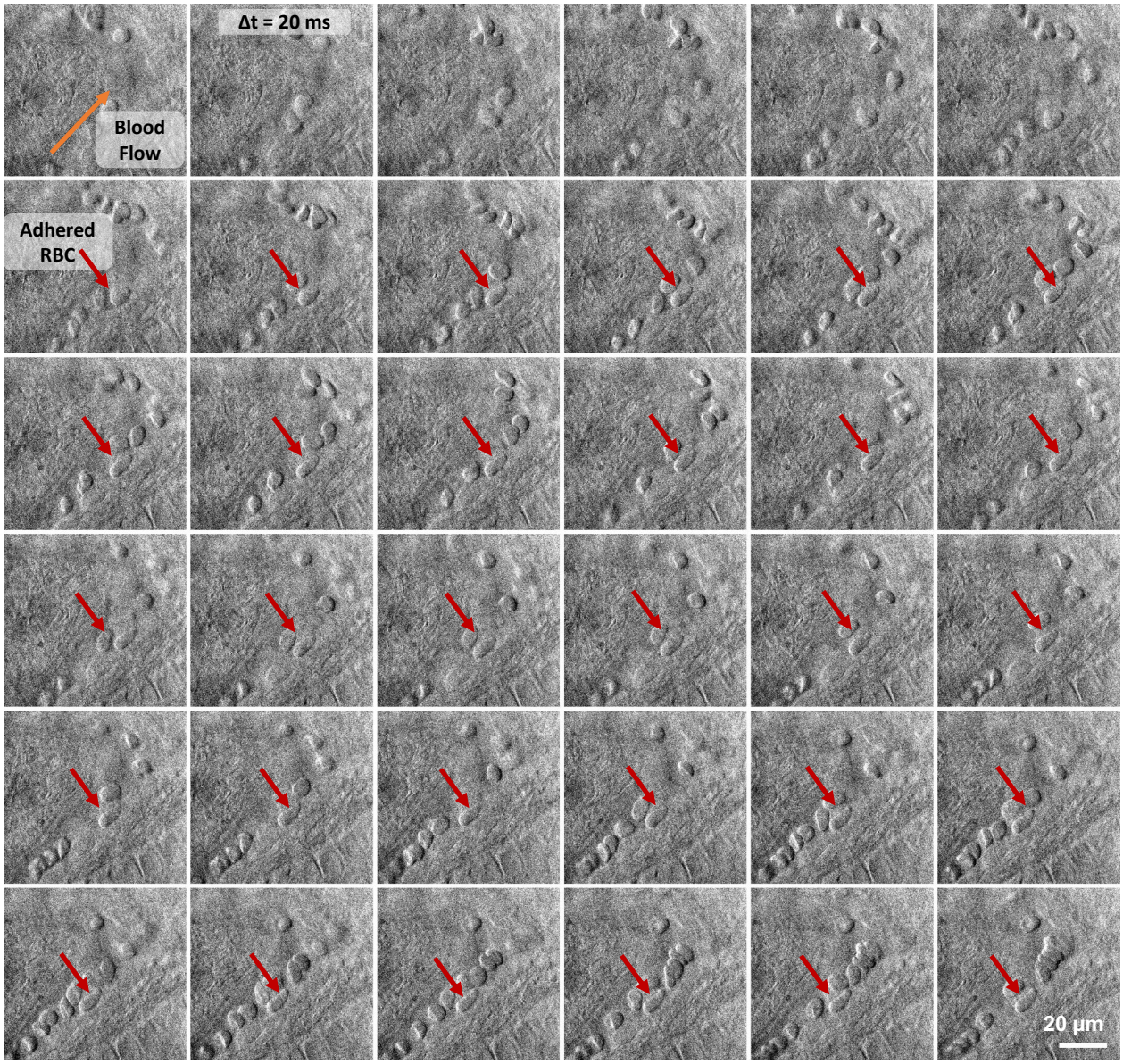

Figure 4-16. Time series showing RBC adhesion with 640 nm illumination during blood flow in a relatively small vessel in the ventral tongue. Note that the RBC highlighted by the red arrow remains relatively stationary on the endothelial cell lining while other red blood cells flow around it. Time series progresses left-to-right, top-to-bottom with $\Delta t = 20$ ms intervals between panels.

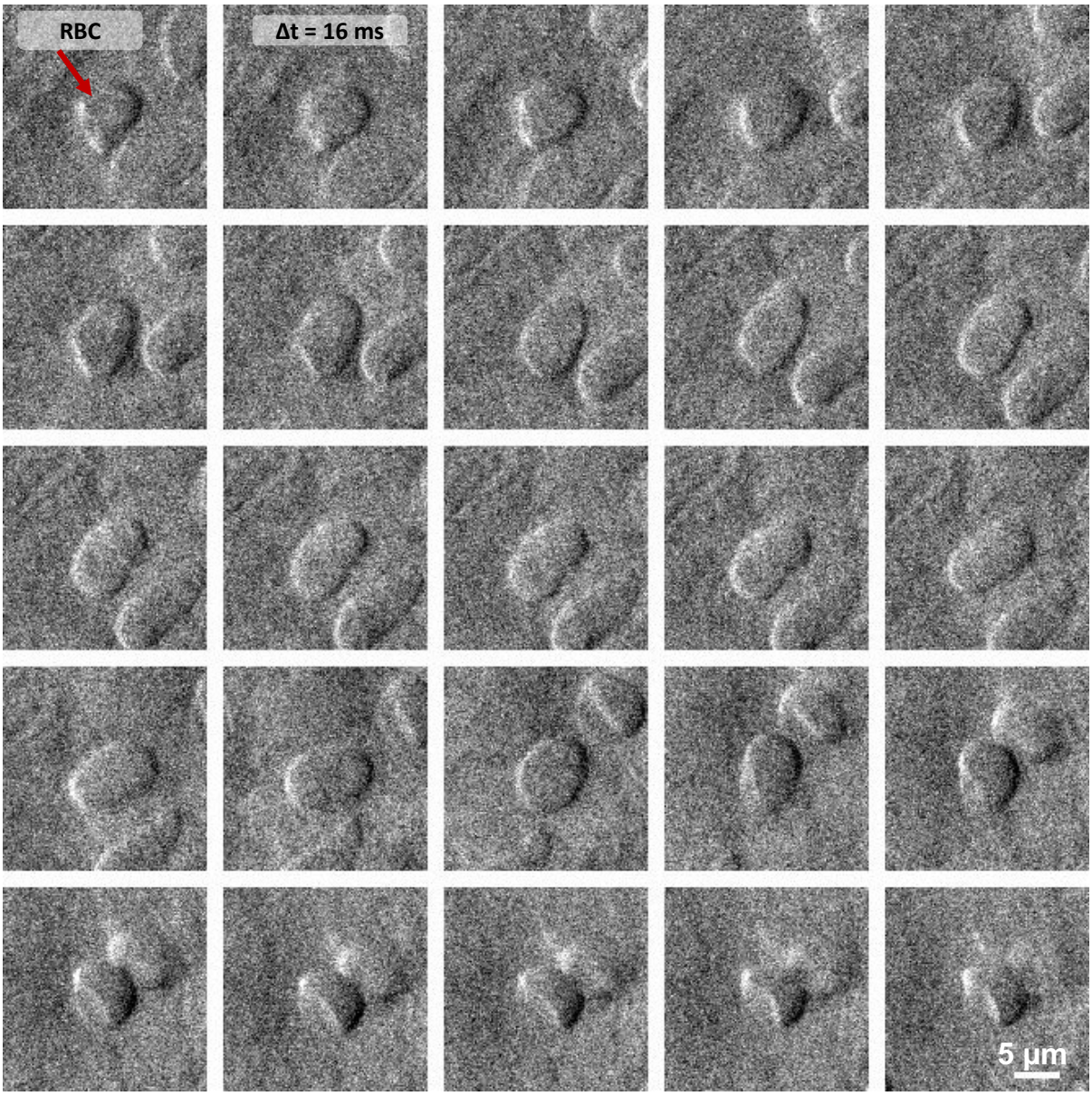

Figure 4-17. Time series showing RBC morphological dynamics with 640 nm illumination during blood flow in a relatively small vessel in the ventral tongue. Note that the RBC highlighted by the red arrow changes shape dramatically in time. Time series progresses left-to-right, top-to-bottom with $\Delta t = 16$ ms intervals between panels.

Other phenomena observed *in vivo*

Other interesting structures are visible with phase contrast provided by OBC in the surrounding skin tissue. For example, extra-capillary granules surrounding blood vessels (Figure 4-18) are often visible. The exact composition and function of these structures is unknown, however it appears they may be present within dendritic cells, as particularly visible in Figure 4-18(b). Additionally, details of surrounding epithelial cells are resolved, shown in Figure 4-19. Using image averaging of a stationary portion of tissue, features of the stratum spinosum are resolved with remarkable detail (Figure 4-19(b)). The intercellular junctions are highlighted, along with nuclei and nucleoli, and their correspondence to a conventional H&E stained slide (Figure 4-19(a)) are unmistakable.

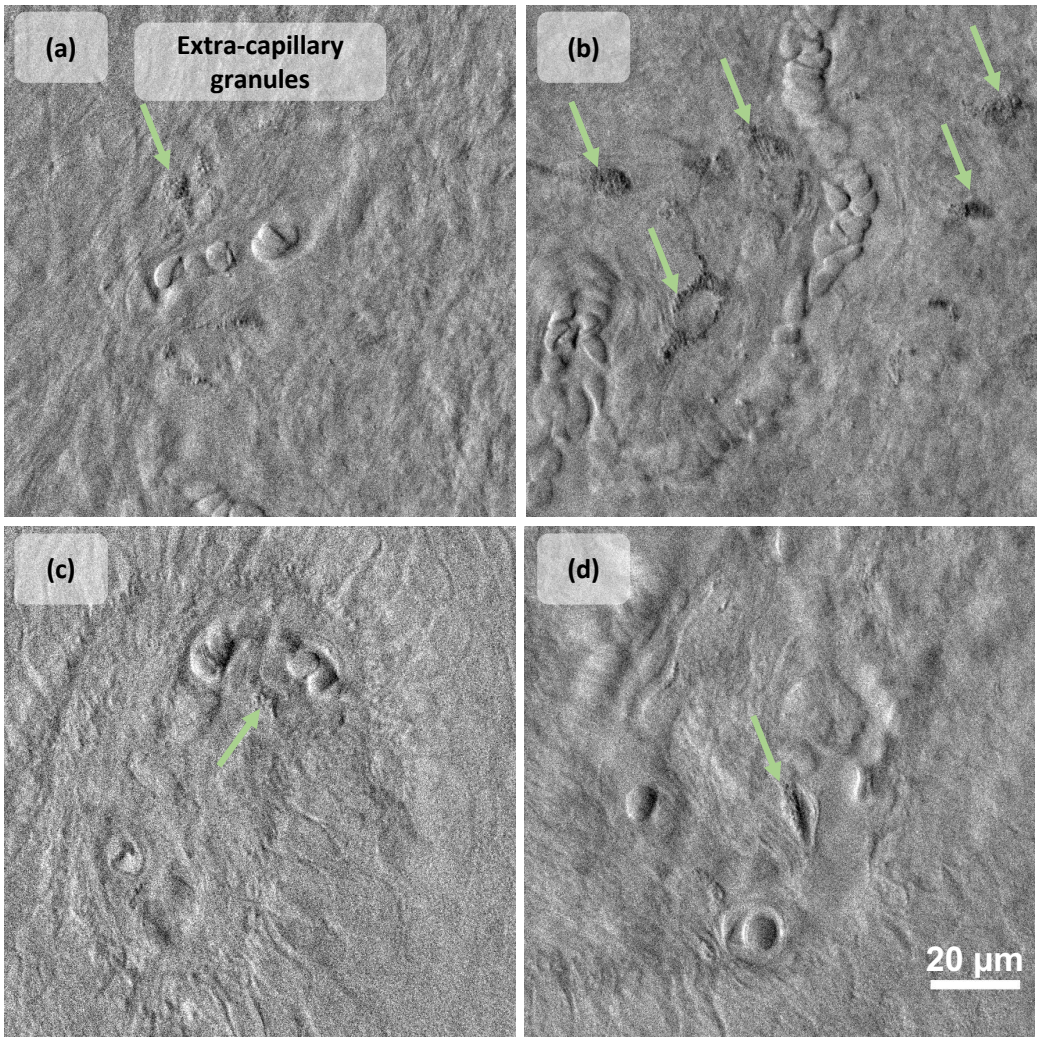

Figure 4-18. Unknown extra-capillary granules (green arrows).

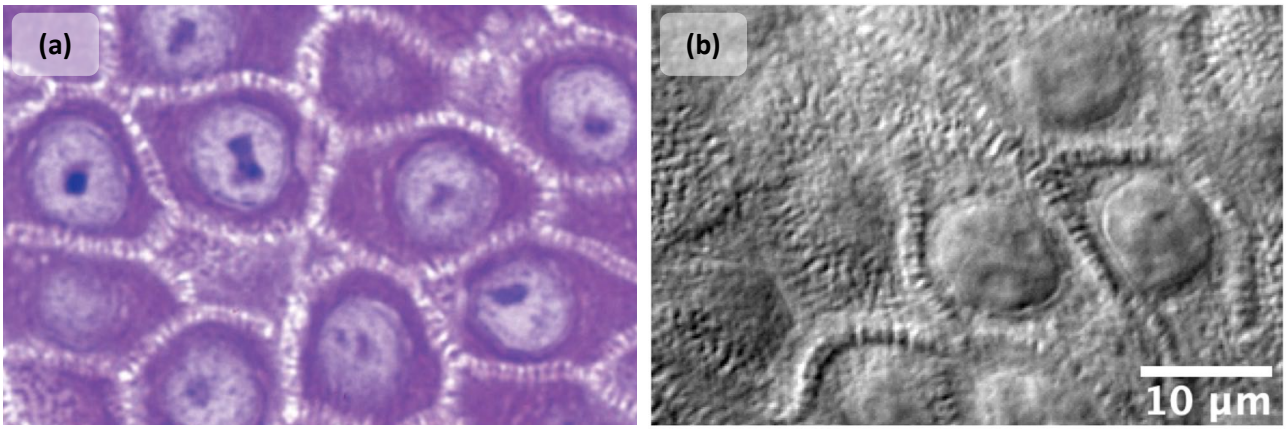

Figure 4-19. (a) Hematoxylin and Eosin stained slide imaging with conventional microscopy shows keratinocytes of the stratum spinosum with characteristic intercellular junctions [59]. (b) Similar features are observed in a label-free manner in live human tissue using OBC with image averaging. Note how the nuclei are readily visible and even nucleoli are resolved.

Finally, longitudinal imaging provided by the OBC system enables the study of vascular flow. For example, by measuring the mean intensity of the field of view when a large vessel is present, an oscillatory pattern emerges at the predicted frequency of a human heart beat (Figure 4-20). Thus OBC could provide a window into studying vital signs and blood flow simultaneously, and may also open the door to the discovery of new biomarkers and vital signs based on blood viscosity and rheology.

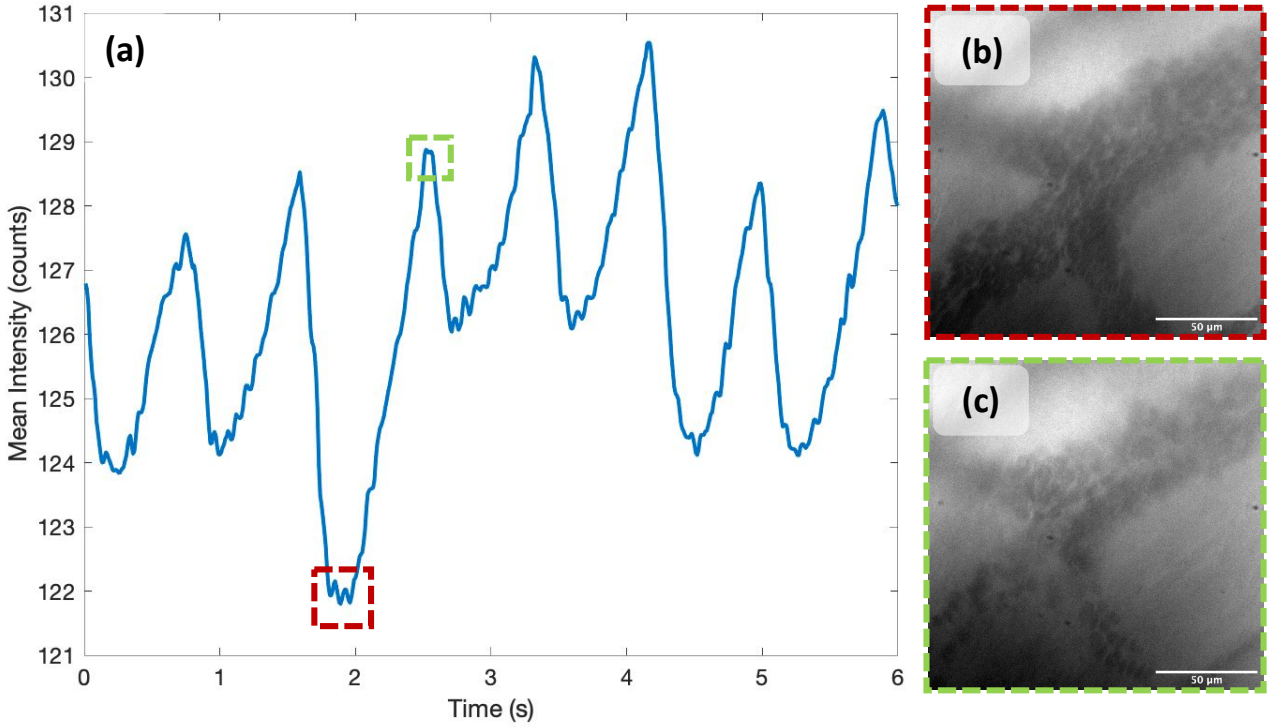

Figure 4-20. (a) Mean intensity vs. time in the green channel as a large vessel is held stationary within the field of view using pneumatic stabilization. A rhythmic pattern is observed likely due to heart rate. (b) Representative image with low mean intensity (high RBC content) likely occurring just after systole, and (c) representative image with high mean intensity (low RBC count) likely occurring during diastole.

Discussion

In Figure 4-3, phase contrast was shown to be optimized by looking at contrast between adjacent red blood cells in the same capillary as the source-detector separation was altered. These data show a very similar trend to that observed in the *in vitro* models, both with the

lipid particle experiment (Figure 2-5), and with the *in vitro* microfluidic experiment (Figure 3-4 and Figure 3-5). These data suggest that the previous *in vitro* experiments provided good models of scattering phenomena and phase contrast produced via oblique back-illumination observed *in vivo*. They also provide further evidence that there exists a source-detector separation of approximately 200-250 μm that optimizes the oblique back-illumination that is relatively invariant. Importantly, this close source detector separation is approximately 1/2 the width of the image of the LED source in object space, and the degradation of phase contrast with even smaller source detector separations may occur as the source crosses over the optic axis and part of the source contributes obliquity in the opposite direction.

In vivo imaging with OBC demonstrates spatial and temporal resolution of human blood cells in a label-free manner with unprecedented clarity. Figure 4-4 captures this, demonstrating that OBC with the single-source system enables imaging many different size vessels in the ventral tongue without significant motion blur and with high spatial detail. Red blood cells are clearly visible as biconcave discs passing through capillary-sized vessels in Figure 4-4(a)-(b), with interspersed platelets also clearly resolved Figure 4-4(b)-(c). Even smaller particles, approximately 600 nm in diameter are visible in Figure 4-4(d), which is likely a chylomicron, given its size. Figure 4-4(e)-(l) highlight that OBC is also able to resolve white blood cells with remarkable detail. Small, relatively uniform white blood cells, likely lymphocytes, are shown in Figure 4-4(e) and (k), while larger, granulated white blood cells are also clearly visible (Figure 4-4(f), (i), (j), (l)). These results show promise for OBC as a technique for non-invasive blood cell counting as red blood cells, white blood cells, and platelets are directly visible. Using characteristics of size and granularity, it may also be possible to separate white blood cells further into sub-classes, however the accuracy of any such approach has yet to be tested. However, OBC does not appear to highlight nuclei, which are normally a critical element for identifying the class of white blood cell in blood counting and peripheral blood smears. It is likely that any such approach to sub-classify white blood cells *in vivo* would greatly benefit from further development of OBC to reveal

nuclear structure.

One of the major drawbacks of nailfold capillaroscopy for non-invasive neutropenia screening (Figure 1-16) is that it fails in individuals with darker skin tones (Fitzpatrick skin phototype > 4). This is due to melanin, which is concentrated superficial to peripheral capillaries, and has a similar absorption of blue-green light as hemoglobin. Thus, despite the promise shown by non-invasive nailfold neutropenia screening, there appears a fundamental obstacle to using it in an equitable way. In contrast to this, the oral mucosa has very little melanin regardless of peripheral skin tone. Further, capillaries are known to be significantly more superficial than in the nailfold, which enables the use of phase contrast produced by oblique back-illumination. In Figure 4-5, OBC was applied to imaging the ventral tongue capillaries of three individuals spanning the Fitzpatrick skin phototype spectrum. Similarly shaped capillaries were selected and the intensity profile across pairs of red blood cells was measured, showing similar contrast. Thus, ventral tongue imaging with OBC not only enables the resolution of phase-only, otherwise transparent particles such as white blood cells and platelets, but it also enables imaging blood cells *in vivo* regardless of skin phototype.

In Figure 4-6, data from the dual-source OBC system is shown. These two panels, with the 640nm red source (Figure 4-6(a)) and the 530nm green source (Figure 4-6(b)) show the impressive wide field of view of the dual-source system. A larger, 20 μm diameter vessel can be observed across a few hundred microns in length longitudinally. Other examples are shown in Figure 4-7, where the large variety of vasculature visible with the dual-source OBC system is apparent in the 640nm channel. In some portions of the ventral tongue, vessels 25-50 μm are readily observable (Figure 4-7(a)-(b)), while in others, small capillary-sized vessels are directly visible (Figure 4-7(c)-(d)). The ability to flexibly resolve a wide range of vessel sizes is important for the throughput of a non-invasive blood counting technique. In a conventional complete blood count, millions of cells must be counted in a few μL of blood in order to achieve an accurate estimate. While this does not seem like a large volume of blood, at the capillary level *in vivo*, it is tremendous. For example, a single capillary 10

μm in diameter has a cross-sectional area of 78.5 μm^2. At a blood velocity of 500 μm/s, approximately 39,250 μm^3/s pass through the capillary, or 39.25 picoliters per second. In order to achieve the same amount of cells counted in only 1 μL of a conventional blood count, it would require approximately 7 hours of recording and counting a single capillary with OBC. Recall that basophils, typically the rarest of white blood cells, are often at a concentration of only 50/μL. Thus, even to observe a single basophil, would require approximately 21 minutes of recording a single capillary. In contrast to this, a larger vessel, such as the 25 μm diameter one shown in Figure 4-7(a), has a 490.625 μm^2 cross-sectional area and could provide higher throughput for counting. Additionally, blood in larger vessels tends to travel faster. Counting cells in this vessel at a blood velocity of 3 mm/s would enable 1,471,875 μm^3/s or 1.471875 nanoliters/s, and imaging 1 μL would take 11.3 minutes. A basophil could be expected to pass through this size vessel approximately every 34 seconds. However, larger vessels will inevitably provide a more challenging environment for counting cells due to tightly packed cells yielding overlapping boundaries and partially occluded features. Though lower in throughput, capillaries provide the opportunity to image and count cells in a single file nature. This may yield higher counting accuracy and morphological assessment of the more common cell types such as red blood cells and platelets.

The ergonomics and pneumatic stabilization techniques highlighted in Figure 4-1 and Figure 4-2 provide the ability to longitudinally image the same blood vessel as thousands of cells pass through. These techniques so far enabled longitudinal imaging of the same vessel $>$ 10 minutes in duration. Several time series highlight interesting and important phenomena observed with this technique. For example, Figure 4-8 demonstrates a white blood cell adhered to the endothelial cell lining of a blood vessel approximately 20 μm in diameter. In a period of about 70-80 ms, three red blood cells approach and deform around the stationary leukocyte. This phenomena is also observed with combined phase and absorption contrast with 530nm illumination in the time series shown in Figure 4-9 and in a larger vessel Figure 4-10. These results show that OBC is a useful candidate to study

WBC-endothelial cell interactions in their native environment, which could have tremendous clinical utility. Leukocyte adhesion is an important physiological part of the immune response, and elevated adherence and rolling of leukocytes has been shown directly predictive of survival outcomes in hematopoietic cell transplantation patients [238]. Further, in sepsis, leukocyte activation and adhesion are regarded as essential components leading to organ dysfunction, and disruption of leukocyte-endothelial cell interactions have been shown protective [239]. On the other hand, Leukocyte Adhesion Deficiencies are a group of genetic diseases that cause immunodeficiency and an inability to mount an effective counteroffensive to invading microbes [240]. OBC applied to studying leukocyte-endothelial cell interactions *in vivo* in humans could provide a new set of biomarkers related to inflammation, and a method of studying efficacy of pharmacologic disruption *in vivo*.

Another exciting result shown by OBC is the clear ability to resolve the composition of optical absorption gaps (Figure 4-11). As discussed previously, non-invasive neutropenia screening with nailfold capillaroscopy relies on counting optical absorption gaps between red blood cell shadows (Figure 1-14 and Figure 1-15). However, the exact etiology of the OAGs is not discernable with conventional nailfold capillaroscopy due to a lack of phase contrast. In OBC however, white blood cells can clearly be resolved and distinguished from background blood plasma. In Figure 4-11(a), the top row highlights a time series where a leukocyte passes through a capillary loop, densely packed with adjacent red blood cells. Seconds later, a larger plasma gap passes through the vessel without a white blood cell (Figure 4-11(b), bottom row). While these two events are distinguished using OBC, they would be indistinguishable in conventional nailfold capillaroscopy. Further, nailfold capillaroscopy often relies on quantifying only uncompressible "major event" OAGs to increase the likelihood that the identified OAG contains of a white blood cell. However, the data in Figure 4-11 tells a different story, where a plasma-only gap (Figure 4-11(b)) demonstrates consistent spacing (incompressibility) throughout time, while the OAG with the white blood cell (Figure 4-11(a)) appears much smaller and closely packed to red blood cells. In Figure 4-12, an optical

absorption gap is shown passing through a different capillary loop, with a small plasma gap followed by a granulated white blood cell. Further, OBC reveals that leukocytes often travel in pairs in blood vessels (Figure 4-13), which would be indistinguishable from a single white blood cell or plasma gap in conventional nailfold capillaroscopy. Thus, OBC shows that some, but not all optical absorption gaps contain white blood cells, and others contain pairs of white blood cells. It is clear that a non-invasive white blood cell count is likely to be more accurate with the incorporation of phase contrast.

Importantly, despite moving from the higher resolution 40X 1.15 NA used in the single-source OBC system to the 20X 0.75 NA objective used in the dual source OBC system, small particles such as the granules within white blood cells (Figure 4-14) and platelets (Figure 4-15) are still visible. However, no evidence of lipid particles was observed with the dual-source system as was observed in (Figure 4-4(d)) with the single-source OBC system. Thus, while the resolution is slightly worse for the dual-source OBC system, it is still able to resolve the most important small details necessary for blood cell analysis, and its added benefit of increased field of view is likely worth the tradeoff in resolution.

The use of OBC to study red blood cell morphology is compelling for its ability to clearly resolve their characteristic bi-concave shape (Figure 4-4(a)-(b)). Other interesting red blood cell phenomena were observed too, including erythrocyte adhesion to endothelial cells, shown in the time series of Figure 4-16. These data are reminiscent of the observation of sickled erythrocytes *in vivo* shown in Figure 3-10(b). However, in these data, surrounding red blood cells are blurred due to low temporal resolution, while the current OBC system provides clear temporal and spatial resolution not only of the adhered red blood cell, but also of the red blood cells flowing rapidly by it. Red blood cell deformability is also clearly observed at the capillary level, highlighted in Figure 4-17. Here a single red blood cell is tracked manually at the center of the region of interest with time. Over the course of approximately 400 ms, the same red blood cell begins as a concave disk, elongates into an ellipsoid, and returns to a concave disk as it winds through a small capillary. While this represents data in a healthy

individual, it is clear that red blood cell deformability and morphology can be observed using OBC, a technique that could be applied to study sickle cell disease and other thalassemia *in vivo*.

Other extra-capillary phenomena were observed, including granules highlighted in Figure 4-18 (green arrows) of unknown etiology. These could be contained within dendritic cells, an example of which is shown in the top right panel with processes extending upward away from the main soma. However, more research must be done to determine the composition and significance of these granules as no description in the literature was yet found. Keratinocytes of the surrounding epithelium are also readily visible, highlighted in Figure 4-19 where averaged images produce a clear view of the stratum spinosum acquired with OBC (Figure 4-19(b)) as compared to a conventional slide with hematoxylin and eosin staining (Figure 4-19(a)). The desmosomal intercellular junctions are clearly visible, along with the profile of the nucleus and even nucleoli within.

Lastly, longitudinal imaging of the same vessel also offers the ability to study flow dynamics of blood cells *in vivo*. While this field will be greatly expanded upon once automated computer vision algorithms are developed to facilitate video analysis, preliminary evidence shows that even simple calculation of mean intensity across the entire field of view vs. time (Figure 4-20) can provide interesting insight. Here a pulsatile, saw-tooth like pattern is observed, where lower intensity (red box, panel (b)) occurs with the vessels filling with absorptive red blood cells (likely through systole), and higher intensity occurs as the vessels are relatively void of RBCs (likely during diastole). The observed pattern has a mean frequency around 1.1 Hz, which is well within the realm of normal physiological heart beat. OBC imaging may not only provide a window into current vital signs such as heart rate and blood pressure at the level of the vasculature, it may also provide access to new biomarkers based on rheology and blood flow turbulence.

Chapter 5

Conclusions and general discussion

Over hundreds of years, the initial discovery and recognition of the importance of blood cells in health and disease has motivated the development of automated hematologic analyzers and microscopic analysis of peripheral blood smears. Many of the most important discoveries about blood cells paralleled the development of new microscopy techniques, as visualization of the minute details of blood cells revealed their remarkable diversity and complexity. Imaging-based technologies gave way to flow cytometric techniques, where blood cells pass single-file through sensitive probes that measure impedance, fluorescence, and scattering in a high-throughput manner. This approach has enabled the complete blood count, which provides clinicians a broad range of information about hematologic health, including a critical assessment of the capacity to deliver oxygen, inflammation, immunosuppression, and auto-immunity. When a more thorough investigation of blood cell morphology is needed, microscopic evaluation of a peripheral blood smear is still routine. These two technologies have been refined into complex and precise clinical and research tools that are mainstays of modern health care.

Despite the incredible technological advancements that have enabled the CBC and its ubiquitous adoption in clinical practice, the fundamental invasivity of the technique has never changed. Phlebotomy, whereby a needle is inserted typically into a vein and blood is drawn, is still the standard method of acquiring the blood sample. Transportation to a core laboratory follows, where relatively bulky and expensive equipment accomplish the

blood analysis *ex vivo*. While this workflow has been successful in modern hospitals for most patients, non-invasive blood cell counting and analysis is a relatively unexplored field that could offer tremendous new insight and improvement in patient care.

The development of non-invasive blood cell counting would be impactful in many different arenas of healthcare. First, in the immunocompromised, invasive blood draw can lead to iatrogenic infection. This poses an especially acute problem for cancer patients receiving chemotherapy who, despite their immunodeficient state, must travel to a healthcare setting frequently to monitor their white blood cell counts. Second, in low-birthweight neonates, blood loss through phlebotomy is a major contributor to iatrogenic anemia and subsequent transfusions. The ability to study blood cells *in vivo* in this population is even more promising than in adults given the relative superficiality of their capillaries and translucency of their skin. And third, in remote and low-resource setting, trained medical personnel are required to conduct phlebotomy, proper personal protective equipment is required for handling potentially infectious human blood, and complex and expensive laboratory equipment is prohibitive in the point-of-care setting. Each of these clinical cases represents vulnerable patient populations whose care would be directly improved if non-invasive blood cell counting were possible. However, as with many advancements in science, often once a tool becomes available, new discoveries and unpredicted applications become apparent. Thus these are just some hypothetical cases where non-invasive blood cell counting and analysis would be beneficial, but should not be considered even close to an exhaustive list.

Non-invasive blood cell counting and analysis is likely to yield access to new biomarkers and vital signs that are currently missed by the conventional invasive workflow. For example, quantification of leukocyte rolling and adhesion on endothelial cell walls could be a predictor of transplant outcome, auto-immune conditions, inflammation, and an early predictor of sepsis. Further, the quantification of blood viscosity and rheology are likely tremendously important and virtually ignored by current *ex vivo* blood analysis. Shock, transfusion, sickle cell, thalassemia, anemia, leukemia, stroke, thrombosis, hemolysis, thrombocytosis, and

thrombocytopenia are each likely to demonstrate some form of alteration in these unexplored biomarkers. In fact, nearly all of the vital signs currently used in clinical care including respiratory rate, heart rate, blood pressure, and temperature are mediated by vasculature and blood flow. However, while conventional vital signs are measured at the macroscopic level, it could be just as insightful and clinically relevant to measure the same and new parameters at the microvascular level.

The concept of non-invasive blood cell and microvascular imaging is not novel, and has been studied using optical imaging modalities such as capillaroscopy, confocal microscopy, and optical coherence tomography for decades. However, the technique of oblique back-illumination capillaroscopy applied to imaging capillaries in the oral mucosa demonstrated here represents a tremendous step forward in the practical implementation of non-invasive blood cell imaging and analysis. OBC, with its combined phase and absorption contrast, optimized source detector axis separation, and access to the forward-scattered field despite epi-mode illumination enables the highest spatial resolution images of human blood cells *in vivo* to date. A brief visual comparison to other state-of-the-art *in vivo* blood cell imaging techniques is shown in Figure 5-1. As compared to confocal techniques such as reflectance confocal microscopy (Figure 5-1(b) [60]) and spectrally encoded flow cytometry (Figure 5-1(c) [61]), OBC provides both higher frame rates, as well as resolution of low-spatial frequency structures such as the general outline of the cell. Note that in Figure 5-1(b), only stationary adhered leukocytes are resolved due to motion blur, and the plasma membrane of cells is poorly defined in both confocal techniques. Additionally, compared to OBM, OBC provides higher resolution and higher frame rate imaging due to simultaneous acquisition of data without any sequential illumination and the optimized source-detector separation with a high NA objective (Figure 5-1(e) [46]). While OBC does not currently enable quantitative phase imaging like qOBM (Figure 5-1(f) [47]), it enables 10X higher frame rate imaging, which is required for imaging blood cells under flow. Note the blood cells in qOBM Figure 5-1(f) are stationary *ex vivo*. Using OBC, red blood cells, white blood cells, and platelets can be

distinguished based upon absorption contrast provided by hemoglobin and size observed using phase contrast. Further, the resolution of cellular features such as white blood cell granularity shows promise for sub-classification of white blood cell type. Importantly, OBC is remarkably simple given the quality of data it affords. It operates without any moving parts, requires no scanning, and its speed is limited only by the sensor used. Thus OBC is readily able to image and temporally resolve flowing blood cells *in vivo* in their native environment. OBC is inexpensive compared to many microscopy systems and hematologic analyzers, and its simplicity makes it miniaturizable and adaptable to portable systems such as a mobile phone platform. Finally, its application in the oral mucosa provides a window to superficial capillaries and promises a device that works equally across all skin tones.

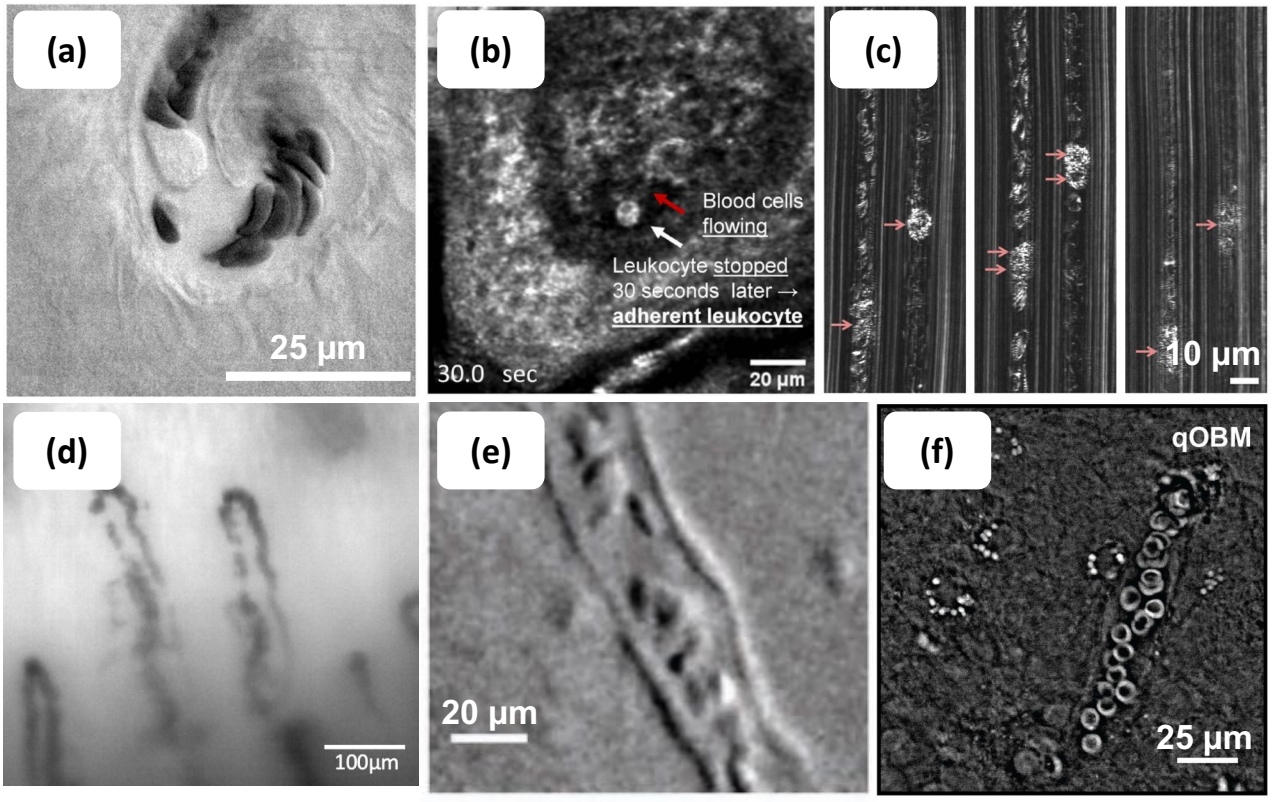

Figure 5-1. Comparison of state-of-the art *in vivo* blood cell imaging modalities with (a) Oblique-back-illumination capillaroscopy. (b) Reflectance confocal microscopy [60], (c) spectrally encoded flow cytometry [61], (d) conventional widefield capillaroscopy, (e) oblique back-illumination microscopy [46], (f) quantitative oblique back-illumination capillaroscopy [47]. Note these images are all taken from different capillaries, however in the case of qOBM, the images were taken *ex vivo* while blood cells were stationary.

The many attributes of OBC make it promising as a foundation for non-invasive blood cell counting and analysis. However, much like the early days of blood cell counting, it is still very much in its nascent phase, and significant work remains to realize its full potential. For example, the development and training of deep-learning based algorithms for cell instance segmentation, classification, counting, and morphological analysis will be critical for the success of any imaging modality aiming to provide non-invasive blood analysis in a high-throughput manner.

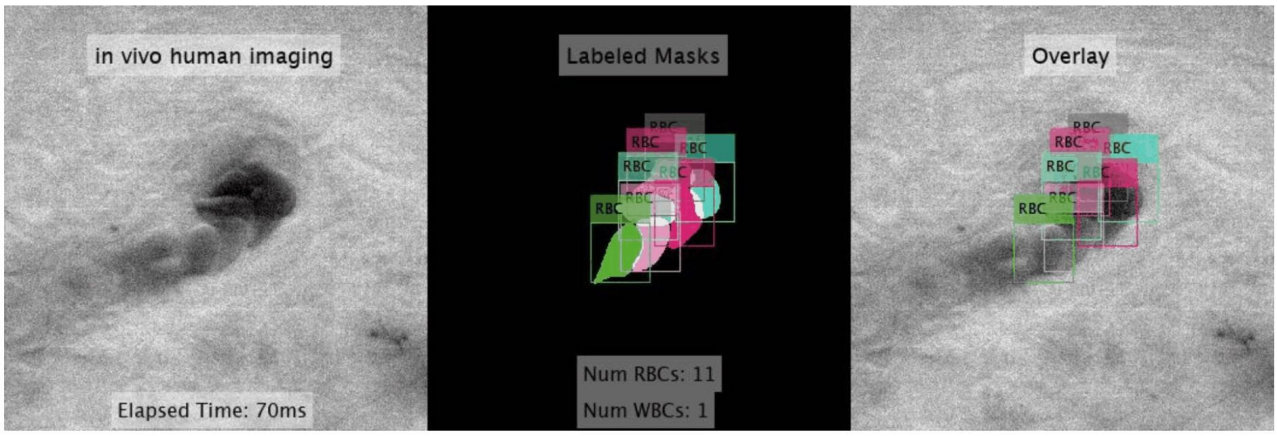

Figure 5-2. Automated OBC imaging data analysis will yield practical adoption of the technology. Video instance segmentation such as that provided by MaskTrack R-CNN or similar state-of-the-art algorithms are likely to be successful with adequate labeled data [62].

Fortunately, the development of OBC is occurring at a time where off-the-shelf deep learning algorithms will likely be able to accomplish these tasks, provided enough training data can be generated and labeled. The microfluidic devices presented here will be a crucial tool to developing these labeled training databases. Finally, while OBC shows tremendous promise for non-invasive blood cell imaging in humans, other techniques may outperform it for specific applications. Special attention should be paid to the rise of lens-free imaging modalities such as holography, diffuser, and phase mask based imaging as these techniques can provide 3D imaging with a remarkably small form factor. While they currently lag OBC in terms of spatial and temporal resolution, it is possible they will eventually work well enough to enable sampling full 3D volumes of blood in large vessels with a compact,

stand-alone device able to slide directly under the tongue, into the inner lip, or other areas of the body. Thus, the field of blood cell counting and analysis may well be at a crossroads, where novel forms of non-invasive imaging and computer vision algorithms stand to take its place after decades of further development.

References

[1] A. V. Leeuwenhoek, "Arcana Natura Detecta," *Delphis, Batav*, 1695.

[2] W. Addison, "Experimental and practical researches on the nature and origin of tubercles in the lungs," *Provincial Medical and Surgical Journal*, pp. 1–76, 1842.

[3] R. S. Riley, J. M. Ben-Ezra, D. Massey, and J. Cousar, "The virtual blood film," *Clinics in Laboratory Medicine*, vol. 22, no. 1, pp. 317–345, 2002.

[4] S. J. Morrison and D. T. Scadden, "The bone marrow niche for haematopoietic stem cells," *Nature*, vol. 505, no. 7483, pp. 327–334, 2014.

[5] U. Blank, G. Karlsson, and S. Karlsson, "Signaling pathways governing stem-cell fate," *Blood*, vol. 111, no. 2, pp. 492–503, 2008. [Online]. Available: http://dx.doi.org/10.1182/blood-2007-07-075168

[6] M. A. Balanant, "Preparation of human Red Blood Cells for Scanning Electron Microscopy imaging," *PLoS ONE*, 2019.

[7] A. Tombak, "Red Blood Cells and Relation to Thrombosis," *Transfusion Medicine and Scientific Developments*, 2017.

[8] J. Tame and B. Vallone, "1A3N DEOXY HUMAN HEMOGLOBIN," 1998. [Online]. Available: https://www.rcsb.org/structure/1a3n

[9] S. Prahl, "Optical Absorption of Hemoglobin," *OMLC*, p. 1999. [Online]. Available: https://omlc.org/spectra/hemoglobin/

[10] E. Maurer-Spurej, K. Brown, A. Labrie, A. Marziali, and O. Glatter, "Portable dynamic light scattering instrument and method for the measurement of blood platelet suspensions," *Physics in Medicine and Biology*, vol. 51, no. 15, pp. 3747–3758, 2006.

[11] K. Takahashi, C. Liang, T. Oda, and N. Ohkohchi, "Platelet and liver regeneration after liver surgery," *Tissue Regeneration – From Basic Biology to Clinical Application*, vol. 50, no. 9, pp. 974–983, 2012.

[12] B. Korkmaz, M. S. Horwitz, D. E. Jenne, and F. Gauthier, "Neutrophil elastase, proteinase 3, and cathepsin G as therapeutic targets in human diseases," *Pharmacological Reviews*, vol. 62, no. 4, pp. 726–759, 2010.

[13] A. Sheshachalam, N. Srivastava, T. Mitchell, P. Lacy, and G. Eitzen, "Granule protein processing and regulated secretion in neutrophils," *Frontiers in Immunology*, vol. 5, no. SEP, pp. 1–11, 2014.

[14] B. Y. A. Polliack, M. A. N. Fu, S. D. Douglas, Z. Bentwich, N. Lampen, and E. D. E. Harven, "SCANNING ELECTRON MICROSCOPY OF HUMAN LYMPHOCYTE-SHEEP ERYTHROCYTE ROSETTES," *The Journal of Experimental Medicine*, vol. 140, pp. 146–158,

1974.

[15] C. Dalton, S. Adamia, L. M. Pilarski, and K. V. Kaler, "Investigation of human malignant cells by electrorotation," *Annual Report - Conference on Electrical Insulation and Dielectric Phenomena, CEIDP*, no. Figure 1, pp. 485–488, 2004.

[16] K. Oshimi, "Clinical features, pathogenesis, and treatment of large granular lymphocyte leukemias," *Internal Medicine*, vol. 56, no. 14, pp. 1759–1769, 2017.

[17] A. Polliack, "The contribution of scanning electron microscopy in haematology: its role in defining leucocyte and erythrocyte disorders," *Journal of Microscopy*, vol. 123, no. 2, pp. 177–187, 1981.

[18] I. A. Andrianova, A. A. Ponomareva, and R. I. Litvinov, "Structural Alterations of Monocytes in Systemic Lupus Erythematosus," *BioNanoScience*, vol. 7, no. 4, pp. 636–639, 2017.

[19] A. Polliack and S. D. Douglas, "Surface Features of Human Eosinophils: a Scanning and Transmission Electron Microscopic Study of a Case of Eosinophilia," *British Journal of Haematology*, vol. 30, no. 3, pp. 303–306, 1975.

[20] M. A. Giembycz and M. A. Lindsay, "Pharmacology of the eosinophil," *Pharmacol Rev*, vol. 51, no. 2, pp. 213–340, 1999.

[21] Y. Takagi, M. Kono, S. Yamamoto, A. Wada, and T. Morikawa, "Comparison of optical data from flow cytometry and microscopy of leukocytes after exposure to specific reagents," *Microscopy*, vol. 64, no. 5, pp. 305–310, 2015.

[22] P. Anderson, "ELECTRON MICROSCOPY: HEMATOLOGIC: BLOOD: Basophil (basophilic leukocyte)." *PEIR Digital Library*, 2013.

[23] L. Theory, "Hematology Analyzer," 2017. [Online]. Available: https://theory.labster.com/hematology-analyzer/

[24] Semrock, "Filters for Flow Cytometry," 2022. [Online]. Available: https://www.semrock.com/flow-cytometry.aspx

[25] T. Rowley, "Flow Cytometry - A Survey and the Basics," 2022. [Online]. Available: https://www.labome.com/method/Flow-Cytometry-A-Survey-and-the-Basics.html

[26] T. W. Campbell, "Evaluation of the Blood Film," *Clinics in Laboratory Medicine*, vol. 18, no. 1, pp. 703–721, 2015. [Online]. Available: http://dx.doi.org/10.1016/j.cll.2015.05.016

[27] M. Peckham, A. Knibbs, and S. Paxton, "The Histology Guide - Faculty," 2003. [Online]. Available: https://www.histology.leeds.ac.uk/

[28] Gadelius, "Optilia Video Capillaroscope," 2022. [Online]. Available: https://www.gadeliusmedical.com/en/products/Plastic/optipix.html

[29] G. E. Brown, "The Skin Capillaries in Raynaud's Disease," *JAMA Archives of Internal Medicine*, vol. 35, no. 1, pp. 56–73, 1925.

[30] M. Cutolo and V. Smith, "State of the art on nailfold capillaroscopy: A reliable diagnostic tool and putative biomarker in rheumatology?" *Rheumatology (United Kingdom)*, vol. 52, no. 11, pp. 1933–1940, 2013.

[31] A. Bourquard, A. Pablo Trinidad, I. Butterworth, Á. Sánchez Ferro, C. Cerrato, K. Humala, M. F. Urdiola, C. D. Rio, B. Valles, J. M. Tucker Schwartz, E. S. Lee, B. J. Vakoc, T. P. Padera, M. J. Ledesma Carbayo, Y.-B. Chen, E. P. Hochberg, M. L. Gray, and C. Castro González, "Non-invasive detection of severe neutropenia in chemotherapy patients by optical

imaging of nailfold microcirculation," *Scientific Reports*, vol. 8:5301, no. November 2017, pp. 1–12, 2018.

[32] A. Pablo-Trinidad, I. Butterworth, M. J. Ledesma-Carbayo, T. Vettenburg, A. Sanchez-Ferro, L. Soenksen, N. J. Durr, A. Munoz-Barrutia, C. Cerrato, K. Humala, M. F. Urdiol, C. Del Rio, B. Valles, Y.-B. Chen, E. P. Hochberg, C. Castro-González, and A. Bourquard, "Automated detection of neutropenia using noninvasive video microscopy of superficial capillaries," *American Journal of Hematology*, vol. 94, no. 8, pp. E219–E222, 2019.

[33] C. Castro-González, I. Butterworth, A. Bourquard, and A. Sanchez-Ferro, "Systems, Apparatus, and Methods for Analyzing Blood Cell Dynamics (US 9,984,277 B2)," *United States Patent*, 2018.

[34] U. Baran, L. Shi, and R. K. Wang, "Capillary blood flow imaging within human finger cuticle using optical microangiography," *Journal of Biophotonics*, vol. 8, no. 0, pp. 46–51, 2015.

[35] I. M. Braverman and A. Yen, "Ultrastructure of the human dermal microcirculation: II. The capillary loops of the dermal papillae," *Journal of Investigative Dermatology*, vol. 68, no. 1, pp. 44–52, 1977.

[36] A. J. Deegan and R. K. Wang, "Microvascular imaging of the skin," *Physics in Medicine and Biology*, vol. 64, no. 7, 2019.

[37] L. Feller, A. Masilana, R. A. G. Khammissa, M. Altini, Y. Jadwat, and J. Lemmer, "Melanin: the biophysiology of oral melanocytes and physiological oral pigmentation," *Head & Face Medicine*, vol. 10, no. 1, pp. 1–7, 2014. [Online]. Available: Head{&}FaceMedicine

[38] R. Patnayak, A. Jena, M. Inamdar, G. S. Reddy, S. Appasani, and V. Bodagala, "Adenoid cystic carcinoma of mobile tongue," *International Journal of Oral Health Sciences*, vol. 6, no. 2, p. 92, 2016.

[39] Q. Zhang, L. Zhong, P. Tang, Y. Yuan, S. Liu, J. Tian, and X. Lu, "Quantitative refractive index distribution of single cell by combining phase-shifting interferometry and AFM imaging," *Scientific Reports*, vol. 7, no. 1, pp. 1–10, 2017.

[40] R. Márquez-Islas, A. Pérez-Pacheco, R. Quispe-Siccha, L. B. Salazar-Nieva, and A. García-Valenzuela, "Visual Assessment of Blood Plasma versus Optical Transmittance and Refractive Index Measurements for Quantifying Lipemia," *Diagnostics*, vol. 12, no. 2, p. 510, 2022.

[41] S. Y. Kim, J. H. Lee, Y. Shin, T. K. Kim, J. won Lee, M. J. Pyo, A. R. Lee, C. G. Pack, and Y. S. Cho, "Label-free imaging and evaluation of characteristic properties of asthma-derived eosinophils using optical diffraction tomography," *Biochemical and Biophysical Research Communications*, vol. 587, pp. 42–48, 2022. [Online]. Available: https://doi.org/10.1016/j.bbrc.2021.11.084

[42] L. Tian and L. Waller, "Quantitative differential phase contrast imaging in an LED array microscope," *Optics Express*, vol. 23, no. 9, p. 11394, 2015.

[43] D. B. Murphy, J. Hinsch, E. D. Salmon, M. Abramowitz, and M. W. Davidson, "Differential Interference Contrast," 2015.

[44] D. Murphy, R. Oldfield, S. Schwartz, and M. W. Davidson, "Introduction to Phase Contrast Microscopy," 2022.

[45] D. K. Hamilton and C. J. Sheppard, "Differential phase contrast in scanning optical microscopy," *Journal of Microscopy*, vol. 133, no. 1, pp. 27–39, 1984.

[46] T. N. Ford, K. K. Chu, and J. Mertz, "Phase-gradient microscopy in thick tissue with oblique

back-illumination," *Nature Methods*, vol. 9, no. 12, pp. 1195–1197, 2012.

[47] P. Ledwig and F. E. Robles, "Epi-mode tomographic quantitative phase imaging in thick scattering samples," *Biomedical Optics Express*, vol. 10, no. 7, pp. 3605–3621, 2019.

[48] T. N. Ford, K. K. Chu, and J. Mertz, "Phase-gradient microscopy in thick tissue with oblique back-illumination," *Nature Methods*, vol. 9, no. 12, pp. 1195–1197, 2012.

[49] T. N. Ford and J. B. U. Mertz, "Video-rate imaging of microcirculation with single-exposure oblique back-illumination microscopy," *Journal of Biomedical Optics*, vol. 18, no. 6, p. 066007, 2013.

[50] T. S. Tkaczyk, *Field Guide to Microscopy*.

[51] G. N. McKay, N. Mohan, and N. J. Durr, "Imaging human blood cells in vivo with oblique back-illumination capillaroscopy," *Biomedical Optics Express*, vol. 11, no. 5, pp. 2373–2382, 2020.

[52] F. Ayers, A. Grant, D. Kuo, D. J. Cuccia, and A. J. Durkin, "Fabrication and characterization of silicone-based tissue phantoms with tunable optical properties in the visible and near infrared domain," *Design and Performance Validation of Phantoms Used in Conjunction with Optical Measurements of Tissue*, vol. 6870, no. February 2008, p. 687007, 2008.

[53] G. Liu, K. Huang, Q. Jia, S. Liu, S. Shen, J. Li, E. Dong, P. Lemaillet, D. W. Allen, and R. X. Xu, "Fabrication of a multilayer tissue-mimicking phantom with tunable optical properties to simulate vascular oxygenation and perfusion for optical imaging technology," *Applied Optics*, vol. 57, no. 23, p. 6772, 2018.

[54] G. N. McKay, T. L. Bobrow, S. Kalyan, S. C. Hur, and N. J. Durr, "Optimizing white blood cell contrast in graded-field capillaroscopy using capillary tissue phantoms," no. February 2020, p. 27, 2020.

[55] G. N. McKay, L. Huang, T. L. Bobrow, S. Kalyan, S. C. Hur, S. Lanzkron, L. H. Pecker, A. R. Moliterno, and N. J. Durr, "A model for generating paired complete blood count and oblique back-illumination capillaroscopy data in tissue-realistic microfluidic chambers," *SPIE BiOS, 2022*, no. March, p. 30, 2022.

[56] O. Alvarez, N. S. Montague, M. Marin, R. O'Brien, and M. M. Rodriguez, "Quantification of sickle cells in the peripheral smear as a marker of disease severity," *Fetal and Pediatric Pathology*, vol. 34, no. 3, pp. 149–154, 2015.

[57] D. K. Kaul and M. E. Fabry, "In vivo studies of sickle red blood cells," *Microcirculation*, vol. 11, no. 2, pp. 153–165, 2004.

[58] M. Sapozhnikov, M. Rehman, C. Johnson, J. Daich, L. Salciccioli, P. Gillette, and J. M. Lazar, "Characterization of microvascular disease in patients with sickle cell disease using nailfold capillaroscopy," *Microvascular Research*, vol. 125, pp. 1–5, 2019.

[59] M. AL, *Junqueira's Basic Histology: Text and Atlas*, 12th ed. The McGraw-Hill Companies Inc., 2009.

[60] I. Saknite, Z. Zhao, J. R. Patrinely, M. Byrne, M. Jagasia, and E. R. Tkaczyk, "Individual Cell Motion in Healthy Human Skin Microvasculature by Reflectance Confocal Video Microscopy," *Microcircualtion*, vol. 27, no. 6, pp. 1–22, 2020.

[61] M. M. Winer, A. Zeidan, D. Yeheskely-hayon, L. Golan, L. Minai, E. J. Dann, and D. Yelin, "In vivo noninvasive microscopy of human leucocytes," *Scientific Reports*, vol. 7, no. 13031, pp. 1–8, 2017. [Online]. Available: http://dx.doi.org/10.1038/s41598-017-13555-1

[62] L. Yang, Y. Fan, and N. Xu, "Video instance segmentation," *Proceedings of the IEEE International Conference on Computer Vision*, vol. 2019-Octob, pp. 5187–5196, 2019.

[63] L. Dean, "Blood Groups and Red Cell Antigens," *National Center for Biotechnology Information (US),*, 2005. [Online]. Available: http://www.ncbi.nlm.nih.gov/books/NBK2267

[64] R. M. Leach and D. F. Treacher, "Oxygen transport - 2. Tissue hypoxia," *Bmj*, vol. 317, no. 7169, p. 1370, 1998.

[65] P.N. Sperryn, "For the Coach - Blood," vol. 23, no. 2, pp. 129–132, 1989.

[66] S. I. Hajdu, "A note from history: The discovery of blood cells." *Annals of clinical and laboratory science*, vol. 33, no. 2, pp. 237–238, 2003.

[67] G. Andral, "Essai d'Hématologie Pathologique," *Fortin, Masson & Cie*, 1843.

[68] P. A. Wark, S. L. Johnston, I. Moric, J. L. Simpson, M. J. Hensley, and P. G. Gibson, "Neutrophil degranulation and cell lysis is associated with clinical severity in virus-induced asthma," *European Respiratory Journal*, vol. 19, no. 1, pp. 68–75, 2002.

[69] M. Schultze, "Ein heizbarer Objecttisch und seine Verwendung bei Untersuchungen des Blutes," *Archiv f. mikros. Anatomie*, vol. 1, pp. 1–42, 1865.

[70] P. Ehrlich, "Beitrage zur Kenntnis der granulirten Bindegewebszellen und der eosinophilen Leukocyten," *Archiv fur Anatomie und Physiologie: Physiologische Abteilung*, pp. 166–169, 1879.

[71] ——, "Ueber die specifischen Granulationen des Blutes," *Verhandlungen der Berliner Physiologischen Gesellschaft: Archiv fur Anatomie und Physiologie: Physiologische Abteilung*, pp. 517–579, 1879.

[72] ——, "Demonstration eines leukamischen Blutpraparates," *Deutsche Medizinische Wochenschrift*, vol. 46, pp. 670–671, 1883.

[73] G. Hayem, "Researches sur l'evolution des hematies dans le sang de l'homme, et des vertebres." *Arch Physiol (deuxieme series)*, vol. 5, pp. 692–734, 1878.

[74] G. Bizzozero, "Su di un nuovo elemento morfologico del sangue dei mammiferi e della sua importanza nella trombosi e nella coagulazione," *Osserv Gazz Clin*, vol. 17, pp. 785–7, 1881.

[75] ——, "Ueber einen neunen Forrnbestandteil des Blutes und dessen Rolle bei der Thrombose und Blut gerinnung," *Virchows Arch Pathol Anat Physiol Klin Med*, vol. 90, no. 261–33, 1882.

[76] ——, "Sur les petites plaques du sang des mammif eres, desuxieme note," *Arch Ital Biol*, vol. 1, pp. 1–4, 1882.

[77] C. L. Balduini and F. Melazzini, "Research at the heart of hematology: Thrombocytopenias and platelet function disorders," *Haematologica*, vol. 102, no. 2, pp. 203–205, 2017.

[78] J.-M. Cavaillon, "The historical milestones in the understanding of leukocyte biology initiated by Elie Metchnikoff," *Journal of Leukocyte Biology*, vol. 90, pp. 413–424, 2011.

[79] A. Maximow, "Experimentelle untersuchungen ber die entzundliche Neubildung von Bindegewebe." *In Beitrage zur Pathologischen Anatomie und zur Allgemeinen Pathologie*, 1902.

[80] ——, "Der Lymphozyt als gemeinsame Stammzelle der verschiedenen Blutelemente in der embryonalen Entwicklung und im postfetalen Leben der Saugetiere." *Folia Haematol*, no. 8, pp. 125–134, 1909.

[81] P. Langerhans, "Ueber die Nerven der menschlichen Haut," *Archiv für Pathologische Anatomie*

und Physiologie und für Klinische Medicin, vol. 44, no. 2-3, pp. 325–337, 1868.

[82] E. R. Clark and E. L. Clark, "Relation of monocytes of the blood to the tissue macrophages," *American Journal of Anatomy*, vol. 46, no. 1, pp. 149–185, 1930.

[83] F. Ginhoux and M. Merad, "Ontogeny and homeostasis of Langerhans cells," *Immunology and Cell Biology*, vol. 88, no. 4, pp. 387–392, 2010.

[84] E. Metchnikoff, "L'immunité dans les maladies infectieuses / par Élie Metchnikoff. Contributors," vol. 44, no. 0, pp. 1845–1916, 1916.

[85] A. M. Silverstein, "The dynamics of conceptual change in twentieth century immunology," *Cellular Immunology*, vol. 132, no. 2, pp. 515–531, 1991.

[86] M. Guilliams, F. Ginhoux, C. Jakubzick, S. H. Naik, N. Onai, B. U. Schraml, E. Segura, R. Tussiwand, and S. Yona, "Dendritic cells, monocytes and macrophages: A unified nomenclature based on ontogeny," *Nature Reviews Immunology*, vol. 14, no. 8, pp. 571–578, 2014.

[87] R. van Furth, Z. A. Cohn, J. G. Hirsch, J. H. Humphrey, W. G. Spector, and H. L. Langevoort, "The mononuclear phagocyte system: a new classification of macrophages, monocytes, and their precursor cells." *Bulletin of the World Health Organization*, vol. 46, no. 6, pp. 845–852, 1972.

[88] A. H. Coons, H. J. Creech, and N. R. Jones, "Immunological Properties of an Antibody Containing a Fluorescent Group," *Proc. Soc. Exp. Biol. Med.*, vol. 47, pp. 200–202, 1941.

[89] T. N. Harris, E. Grimm, E. Mertens, and W. E. Ehrich, "The role of the lymphocyte in antibody formation," *Journal of Experimental Medicine*, vol. 81, no. 1, pp. 73–83, 1945.

[90] A. Fagraeus, "Plasma Cellular Reaction and its Relation to the Formation of Antibodies in vitro," *Nature*, no. 4041, p. 499, 1947.

[91] ——, "Plasma cellular reaction and its relation to the formation of antibodies in vitro," *Nature*, vol. 159, no. 4041, p. 499, 1947.

[92] A. Wilson and A. Trumpp, "Bone-marrow haematopoietic-stem-cell niches," *Nature Reviews Immunology*, vol. 6, no. 2, pp. 93–106, 2006.

[93] T. W. Lebien and T. F. Tedder, "B lymphocytes: How they develop and function," *Blood*, vol. 112, no. 5, pp. 1570–1580, 2008. [Online]. Available: http://dx.doi.org/10.1182/blood-2008-02-078071

[94] J. M. Higgins, "Red Blood Cell Population Dynamics," *Clinics in Laboratory Medicine*, vol. 35, no. 1, pp. 43–57, 2015.

[95] T. J. McMahon, "Red Blood Cell Deformability, Vasoactive Mediators, and Adhesion," *Frontiers in Physiology*, vol. 10, no. November, pp. 1–10, 2019.

[96] Z. W. Zhang, J. Cheng, F. Xu, Y. E. Chen, J. B. Du, M. Yuan, F. Zhu, X. C. Xu, and S. Yuan, "Red blood cell extrudes nucleus and mitochondria against oxidative stress," *IUBMB Life*, vol. 63, no. 7, pp. 560–565, 2011.

[97] B. Angelov and I. M. Mladenov, "On The Geometry of Red Blood Cell," *Proceedings of the First International Conference on Geometry, Integrability and Quantization*, pp. 27–46, 2000. [Online]. Available: http://www.emis.de/proceedings/Varna/vol1content.htm

[98] J. V. D. Bossche, K. Devreese, M. V. D. Vyvere, A. Wauters, H. Neels, P. D. Schouwer, C. Gen-s, S. Se, A. Cell, and B. Advia, "Reference Intervals for a Complete Blood Count Determined on different Automated Haematology Analysers : Abx Pentra 120 Retic , Coulter

Gen-S , Sysmex SE 9500 , Abbott Cell Dyn 4000 and Bayer Advia 120 new-generation haematology analysers : Abx Pentra," *Clinical Chemistry and Laboratory Medicine*, vol. 40, no. 1, pp. 69–73, 2002.

[99] J. N. Thon and J. E. Italiano, "Platelet Formation," *Seminars in Hematology*, vol. 47, no. 3, pp. 220–226, 2010. [Online]. Available: http://dx.doi.org/10.1053/j.seminhematol.2010.03.005

[100] S. De Botton, S. Sabri, E. Daugas, Y. Zermati, J. E. Guidotti, O. Hermine, G. Kroemer, W. Vainchenker, and N. Debili, "Platelet formation is the consequence of caspase activation within megakaryocytes," *Blood*, vol. 100, no. 4, pp. 1310–1317, 2002. [Online]. Available: http://dx.doi.org/10.1182/blood-2002-03-0686

[101] D. M. Monroe, M. Hoffman, and H. R. Roberts, "Platelets and thrombin generation," *Arteriosclerosis, Thrombosis, and Vascular Biology*, vol. 22, no. 9, pp. 1381–1389, 2002.

[102] K. G. Mann, K. Brummel-Ziedins, T. Orfeo, and S. Butenas, "Models of blood coagulation," *Blood Cells, Molecules, and Diseases*, vol. 36, no. 2, pp. 108–117, 2006.

[103] D. A. Lane, H. Philippou, and J. A. Huntington, "Directing thrombin," *Blood*, vol. 106, no. 8, pp. 2605–2612, 2005. [Online]. Available: http://dx.doi.org/10.1182/blood-2005-04-1710

[104] S. P. Jackson, "The growing complexity of platelet aggregation," *Blood*, vol. 109, no. 12, pp. 5087–5095, 2007. [Online]. Available: http://dx.doi.org/10.1182/blood-2006-12-027698

[105] E. K. Shin, H. Park, J. Y. Noh, K. M. Lim, and J. H. Chung, "Platelet shape changes and cytoskeleton dynamics as novel therapeutic targets for anti-thrombotic drugs," *Biomolecules and Therapeutics*, vol. 25, no. 3, pp. 223–230, 2017.

[106] S. H. Yun, E. H. Sim, R. Y. Goh, J. I. Park, and J. Y. Han, "Platelet activation: The mechanisms and potential biomarkers," *BioMed Research International*, vol. 2016, pp. 10–14, 2016.

[107] P. Blair and R. Flaumenhaft, "Platelet α–granules_ Basic biology and clinical correlates. 2009.pdf," *Blood*, vol. 23, no. 4, pp. 177–189, 2009.

[108] A. Dupuis, J. C. Bordet, A. Eckly, and C. Gachet, "Platelet δ-storage pool disease: An update," *Journal of Clinical Medicine*, vol. 9, no. 8, pp. 1–23, 2020.

[109] S. M. Lawrence, R. Corriden, and V. Nizet, "How Neutrophils Meet Their End," *Trends in Immunology*, vol. 41, no. 6, pp. 531–544, 2020. [Online]. Available: https://doi.org/10.1016/j.it.2020.03.008

[110] E. Kolaczkowska and P. Kubes, "Neutrophil recruitment and function in health and inflammation," *Nature Reviews Immunology*, vol. 13, no. 3, pp. 159–175, 2013.

[111] J. Prinyakupt and C. Pluempitiwiriyawej, "Segmentation of white blood cells and comparison of cell morphology by linear and naïve Bayes classifiers," *BioMedical Engineering Online*, vol. 14, no. 1, pp. 1–19, 2015.

[112] K. Rodgers, *Neutrophil*, 2016.

[113] J. Lomas, G. Anderson, K. Domnick-Pierre, E. Vayda, and M. W. Enkin, "An Anomaly of Neutrophil Morphology with Impaired Function," *N Engl J Med*, vol. 321, no. 19, pp. 1306–1311, 1989.

[114] P. Brederoo, J. van der Meulen, and A. M. Mommaas-Kienhuis, "Development of the granule population in neutrophil granulocytes from human bone marrow," *Cell and Tissue Research*, vol. 234, no. 3, pp. 469–496, 1983.

[115] F. Mollinedo, B. Martín-Martín, J. Calafat, S. M. Nabokina, and P. A. Lazo, " Role of Vesicle-Associated Membrane Protein-2, Through Q-Soluble N -Ethylmaleimide-Sensitive Factor Attachment Protein Receptor/R-Soluble N -Ethylmaleimide-Sensitive Factor Attachment Protein Receptor Interaction, in the Exocytosis of Specific and Tertia," *The Journal of Immunology*, vol. 170, no. 2, pp. 1034–1042, 2003.

[116] D. E. Lewis and S. E. Blutt, "Organization of the Immune System," *Clinical Immunology*, 2019.

[117] M. Nagasawa, H. Spits, and X. R. Ros, "Innate lymphoid cells (ILCs): Cytokine hubs regulating immunity and tissue homeostasis," *Cold Spring Harbor Perspectives in Biology*, vol. 10, no. 12, pp. 1–15, 2018.

[118] C.-C. Liu and J. D.-E. Young, "Large Granular Lymphocytes," *Encyclopedia of Immunology*, 1998.

[119] B. Fattizzo, V. Bellani, R. Pasquale, J. A. Giannotta, and W. Barcellini, "Large Granular Lymphocyte Expansion in Myeloid Diseases and Bone Marrow Failure Syndromes: Whoever Seeks Finds," *Frontiers in Oncology*, vol. 11, no. October, pp. 1–10, 2021.

[120] K. S. Blum and R. Pabst, "Lymphocyte numbers and subsets in the human blood. Do they mirror the situation in all organs?" *Immunology Letters*, vol. 108, no. 1, pp. 45–51, 2007.

[121] B. V. Kumar, T. Connors, and D. L. Farber, "Human T cell development, localization, and function throughout life," *Immunity.*, vol. 48, no. 2, pp. 202–213, 2018.

[122] S. Canè, S. Ugel, R. Trovato, I. Marigo, F. De Sanctis, S. Sartoris, and V. Bronte, "The endless saga of monocyte diversity," *Frontiers in Immunology*, vol. 10, no. August, pp. 1–18, 2019.

[123] C. E. Olingy, H. Q. Dinh, and C. C. Hedrick, "Monocyte heterogeneity and functions in cancer," *Journal of Leukocyte Biology*, vol. 106, no. 2, pp. 309–322, 2019.

[124] A. Coillard and E. Segura, "In vivo differentiation of human monocytes," *Frontiers in Immunology*, vol. 10, no. AUG, pp. 1–7, 2019.

[125] K. A. Ravin and M. Loy, "The eosinophil in infection," *Clinical Reviews in Allergy and Immunology*, vol. 50, no. 2, pp. 214–227, 2015.

[126] G. Van Hulst, H. M. Batugedara, J. Jorssen, R. Louis, F. Bureau, and C. J. Desmet, "Eosinophil diversity in asthma," *Biochemical Pharmacology*, vol. 179, no. April, p. 113963, 2020. [Online]. Available: https://doi.org/10.1016/j.bcp.2020.113963

[127] J. A. O'Sullivan and B. S. Bochner, "Eosinophils and eosinophil-associated diseases: An update," *Journal of Allergy and Clinical Immunology*, vol. 141, no. 2, pp. 505–517, 2018. [Online]. Available: http://dx.doi.org/10.1016/j.jaci.2017.09.022

[128] G. J. Gleich and D. A. Loegering, "Immunobiology of eosinophils." *Annual review of immunology*, vol. 2, no. 3, pp. 429–459, 1984.

[129] P. Valent and P. Battelheim, "The human basophil," *Critical Reviews in Oncology and Hematology*, vol. 10, no. 4, pp. 327–352, 1990.

[130] A. M. Dvorak, "A role for vesicles in human basophil secretion," *Cell and Tissue Research*, vol. 293, no. 1, pp. 1–22, 1998.

[131] C. N. Cruickshank and K. R. Haye, "The responses of the basophil leucocyte." *The Journal of investigative dermatology*, vol. 51, no. 5, pp. 324–329, 1968.

[132] J. W. Harvey, "Evaluation of Leukocytic Disorders," *Hematology, Veterinary*, 2012.

[133] J. T. Schroeder and D. W. MacGlashan, "New concepts: The basophil," *The Journal of Allergy and Clinical Immunology*, vol. 99, no. 4, pp. 429–433.

[134] M. Kubo, "Mast cells and basophils in allergic inflammation," *Current Opinion in Immunology*, vol. 54, pp. 74–79, 2018. [Online]. Available: https://doi.org/10.1016/j.coi.2018.06.006

[135] H. A. KREBS, "Chemical composition of blood plasma and serum." *Annual review of biochemistry*, vol. 19, no. 12, pp. 409–430, 1950.

[136] S. Varchanis, Y. Dimakopoulos, C. Wagner, and J. Tsamopoulos, "How viscoelastic is human blood plasma?" *Soft Matter*, vol. 14, no. 21, pp. 4238–4251, 2018.

[137] J. B. Germana, J. T. Smilowitza, and A. M. Zivkovica, "Lipoproteins: When size really matters," *Curr Opin Colloid Interface*, vol. 11, no. 2, pp. 1–22, 2006. [Online]. Available: https://www.ncbi.nlm.nih.gov/pmc/articles/PMC3624763/pdf/nihms412728.pdf

[138] British Thoracic Society, "Guidelines for the measurement of respiratory function," *Respiratory Medicine*, vol. 88, no. 3, pp. 165–194, 1994.

[139] NIH, "Comprehensive Metabolic Panel (CMP)," 2021. [Online]. Available: https://medlineplus.gov/lab-tests/comprehensive-metabolic-panel-cmp/

[140] B. DM, H. JE, W. FB, D. LK, B. JS, and A. MN, "Standardizing the prothrombin time. Calibrating coagulation instruments as well as thromboplastin." *Arch Pathol Lab Med*, vol. 117, no. (6), p. 602, 1993.

[141] S. AH, "Contact activation: a revision." *Thromb Haemost*, vol. 78, no. 1, p. 101, 1997.

[142] P. JJ, D. M, and H. A, "One-stage vs. chromogenic assays in haemophilia A." *Eur J Haematol.*, vol. 94, no. 77, pp. 38–44, 2015.

[143] W. JI, F. JC, and E. JW, "A Test in Context: D-Dimer." *J Am Coll Cardiol.*, vol. 70, no. 19, p. 2411, 2017.

[144] A. T. Turer, T. A. Addo, J. L. Martin, M. S. Sabatine, G. D. Lewis, R. E. Gerszten, E. C. Keeley, J. E. Cigarroa, R. A. Lange, L. D. Hillis, and J. A. De Lemos, "Myocardial ischemia induced by rapid atrial pacing causes troponin T release detectable by a highly sensitive assay: Insights from a coronary sinus sampling study," *Journal of the American College of Cardiology*, vol. 57, no. 24, pp. 2398–2405, 2011. [Online]. Available: http://dx.doi.org/10.1016/j.jacc.2010.11.066

[145] C. P. Hornik, D. K. Benjamin, K. C. Becker, D. K. J. Benjamin, J. Li, R. H. Clark, M. Cohen-Wolkowiez, and B. P. Smith, "Use of the Complete Blood Cell Count in Early-Onset Neonatal Sepsis," *Pediatric Infectious Disease*, vol. 31, no. 8, pp. 799–802, 2012.

[146] T. L. Milcic and P. Nash, "The complete blood count in neonates," *Academy of Neonatal Nursing*, p. 111, 2009. [Online]. Available: http://www.academyofneonatalnursing.org/NNT/Hematology{_}CBC.pdf

[147] C. I. Wilson, P. L. Hopkins, B. Cabello-Inchausti, S. J. Melnick, and M. J. Robinson, "The Peripheral Blood Smear in Patients With Sickle Cell Trait: A Morphologic Observation," *Laboratory Medicine*, vol. 31, no. 8, pp. 445–447, 2000.

[148] E. C. Lynch, "Peripheral Blood Smear," pp. 732–734, 1990.

[149] R. Green and S. Wachsmann-Hogiu, "Development, History, and Future of Automated Cell Counters," *Clinics in Laboratory Medicine*, vol. 35, no. 1, pp. 1–10, 2015.

[150] M. R. Melamed, "A brief history of flow cytometry and sorting," *Methods in Cell Biology*, vol. 63, no. 63, pp. 3–17, 2001.

[151] J. Picot, C. L. Guerin, C. Le Van Kim, and C. M. Boulanger, "Flow cytometry: Retrospective, fundamentals and recent instrumentation," *Cytotechnology*, vol. 64, no. 2, pp. 109–130, 2012.

[152] G. Ord, "Photo-Electric Technique for the Counting of Microscopical Cells Author (s): Andrew Moldavan Published by : American Association for the Advancement of Science Stable URL : http://www.jstor.com/stable/1658754," vol. 80, no. 2069, pp. 188–189, 1934.

[153] J. Y. Vis and A. Huisman, "Verification and quality control of routine hematology analyzers," *REVIEW ARTICLE INTERNATIONAL JOURNAL OF LABORATORY HEMATOLOGY*, vol. 38, pp. 100–109, 2016.

[154] W. H. Coulter, "Means for counting particles suspended in a fluid. US Patent, 2656508," *United States Patent Office. Patentiert am*, vol. 20, p. 1953, 1953. [Online]. Available: www.google.com/patents/US2656508

[155] M. I. Tribel'skiĭ, "Features of light scattering by particles with a high absorption coefficient," *Journal of Optical Technology*, vol. 84, no. 7, p. 431, 2017.

[156] G. Mie, "Beiträge zur Optik trüber Medien speziell kolloidaler Goldlösungen (Contributions to the optics of diffuse media, especially colloid metal solutions)," *Ann. Phys. (Leipzig)*, vol. 330, pp. 377–445, 1908.

[157] M. Kerker, *The Scattering of Light and Other Electromagnetic Radiation*. AP, New York, 1969.

[158] O. Magnin, "Blood cells characterization by light scattering," vol. 5461, pp. 57–62.

[159] V. Ost, J. Neukammer, and H. Rinneberg, "Flow Cytometric Differentiation of Erythrocytes and Leukocytes in Dilute Whole Blood by lLght Scattering," *Cytometry*, vol. 32, no. 3, pp. 191–197, 1998.

[160] G. Chhabra, "Automated hematology analyzers: Recent trends and applications," *Journal of Laboratory Physicians*, vol. 10, no. 01, pp. 015–016, 2018.

[161] D. Agrawal and R. Sarode, "Complete Blood Count or Complete Blood Count with Differential: What's the Difference?" *The American Journal of Medicine*, vol. 130, no. 8, pp. 915–916, 2014. [Online]. Available: http://dx.doi.org/10.1016/j.amjmed.2017.03.049

[162] H. Ceelie, R. B. Dinkelaar, and W. Van Gelder, "Examination of peripheral blood films using automated microscopy; evaluation of Diffmaster Octavia and Cellavision DM96," *Journal of Clinical Pathology*, vol. 60, no. 1, pp. 72–79, 2007.

[163] S. Seo, S. O. Isikman, I. Sencan, O. Mudanyali, T. W. Su, W. Bishara, A. Erlinger, and A. Ozcan, "High-throughput lens-free blood analysis on a chip," *Analytical Chemistry*, vol. 82, no. 11, pp. 4621–4627, 2010.

[164] S. B. Kim, H. Bae, K.-i. Koo, M. R. Dokmeci, A. Ozcan, and A. Khademhosseini, "Lens Free Imaging for Biological Applications," *Journal of Laboratory Automation*, vol. 17, no. 1, 201.

[165] S. O. Isikman, W. Bishara, S. Mavandadi, F. W. Yu, S. Feng, R. Lau, and A. Ozcan, "Lens-free optical tomographic microscope with a large imaging volume on a chip," *Proceedings of the National Academy of Sciences of the United States of America*, vol. 108, no. 18, pp. 7296–7301, 2011.

[166] V. V. Tuchin, A. Tárnok, and V. P. Zharov, "In vivo flow cytometry: A horizon of opportunities," *Cytometry Part A*, vol. 79 A, no. 10, pp. 737–745, 2011.

[167] R. Colombatti, L. Sainati, and D. Trevisanuto, "Anemia and transfusion in the neonate," *Seminars in Fetal and Neonatal Medicine*, vol. 21, no. 1, pp. 2–9, 2016. [Online]. Available: http://dx.doi.org/10.1016/j.siny.2015.12.001

[168] Q. H. Vu, H. T. Van, V. T. Tran, T. D. P. Huynh, V. C. Nguyen, and D. T. Le, "Development of a robust blood smear preparation procedure for external quality assessment," *Practical Laboratory Medicine*, vol. 27, no. June, p. e00253, 2021. [Online]. Available: https://doi.org/10.1016/j.plabm.2021.e00253

[169] G. Gulati, J. Song, A. D. Florea, and J. Gong, "Purpose and criteria for blood smear scan, blood smear examination, and blood smear review," *Annals of Laboratory Medicine*, vol. 33, no. 1, pp. 1–7, 2013.

[170] F. Merola, P. Memmolo, L. Miccio, R. Savoia, M. Mugnano, A. Fontana, G. D'Ippolito, A. Sardo, A. Iolascon, A. Gambale, and P. Ferraro, "Tomographic flow cytometry by digital holography," *Light: Science and Applications*, vol. 6, no. 4, pp. 1–7, 2017.

[171] M. Cutolo, *Capillaroscopy in rheumatic diseases. From the XVIII to the XXI century. In: Cutolo M, ed. Atlas of Capillaroscopy in Rheumatic Diseases.*, 1st ed. Milano: Elsevier Srl, 2010.

[172] M. M. Chojnowski, A. Felis-Giemza, and Olesińska, "Capillaroscopy - A role in modern rheumatology," *Reumatologia*, vol. 54, no. 2, pp. 67–72, 2016.

[173] P. Jung and F. Trautinger, "Capillaroscopy," *Journal of the German Society of Dermatology*, pp. 731–736, 2013.

[174] C. H. Chang, R. K. Tsai, W. C. Wu, S. L. Kuo, and H. S. Yu, "Use of Dynamic Capillaroscopy for Studying Cutaneous Microcirculation in Patients with Diabetes Mellitus," *Microvascular Research*, vol. 53, pp. 121–127, 1997.

[175] C. E. Curtis, W. G. Iacono, and M. Beiser, "Relationship between Nailfold Plexus Visibility and Clinical , Neuropsychological , and Brain Structural Measures in Schizophrenia," vol. 3223, no. 1969, 1999.

[176] I. Gurov, M. Volkov, N. Margaryants, A. Pimenov, and A. Potemkin, "High-speed video capillaroscopy method for imaging and evaluation of moving red blood cells," *Optics and Lasers in Engineering*, vol. 104, no. August 2017, pp. 244–251, 2018. [Online]. Available: https://doi.org/10.1016/j.optlaseng.2017.09.003

[177] J. B. U. Mertz, "Introduction to Optical Microscopy," 2010.

[178] P. Ledwig and F. E. Robles, "Quantitative 3D refractive index tomography of opaque samples in epi-mode," *Optica*, vol. 8, no. 1, p. 6, 2021.

[179] I. M. Braverman, "The cutaneous microcirculation: Ultrastructure and microanatomical organization," *Microcirculation*, vol. 4, no. 3, pp. 329–340, 1997.

[180] I. Bentov and M. J. Reed, "The Effect of Aging on the Cutaneous Microvasculature," *Microvascular Research*, vol. 100, pp. 25–31, 2015.

[181] G. Guven, M. P. Hilty, and C. Ince, "Microcirculation: Physiology, Pathophysiology, and Clinical Application," *Blood Purification*, vol. 49, no. 1-2, pp. 143–150, 2020.

[182] L. Segadal and K. Matre, "Blood velocity distribution in the human ascending aorta," *Diagnostic Methods Valvular Heart Disease*, vol. 76, no. 1, pp. 90–100, 1987.

[183] A. Bollinger, P. Butti, J. P. Barras, H. Trachsler, and W. Siegenthaler, "Red blood cell velocity in nailfold capillaries of man measured by a television microscopy technique," *Microvascular*

Research, vol. 7, no. 1, pp. 61–72, 1974.

[184] N. Mugii, M. Hasegawa, Y. Hamaguchi, C. Tanaka, K. Kaji, K. Komura, I. Ueda-Hayakawa, S. Horie, M. Ikuta, K. Tachino, F. Ogawa, S. Sato, M. Fujimoto, and K. Takehara, "Reduced red blood cell velocity in nail-fold capillaries as a sensitive and specific indicator of microcirculation injury in systemic sclerosis," *Rheumatology*, vol. 48, no. 6, pp. 696–703, 2009.

[185] C. C. Wu, G. Zhang, T. C. Huang, and K. P. Lin, "Red blood cell velocity measurements of complete capillary in finger nail-fold using optical flow estimation," *Microvascular Research*, vol. 78, no. 3, pp. 319–324, 2009. [Online]. Available: http://dx.doi.org/10.1016/j.mvr.2009.07.002

[186] N. C. Wetzel and Y. Zotterman, "On differences in the vascular colouration of various regions of the normal human skin," *Heart*, vol. 13, no. 357, 1927.

[187] R. Maiti, M. Duan, S. G. Danby, R. Lewis, S. J. Matcher, and M. J. Carré, "Morphological parametric mapping of 21 skin sites throughout the body using optical coherence tomography," *Journal of the Mechanical Behavior of Biomedical Materials*, vol. 102, no. October 2019, 2020.

[188] J. Sandby-Moller, T. Poulsen, and H. C. Wulf, "Epidermal Thickness at Different Body Sites: Relationship to Age, Gender, Pigmentation, Blood Content, Skin Type and Smoking Habits," *Acta Dermato-Venereologica*, vol. 83, no. 6, pp. 410–413, 2003.

[189] S. L. Jacques, "Optical properties of biological tissues: a review," *Physics in Medicine and Biology*, vol. 58, 2013.

[190] S. Grabtchak, L. G. Montgomery, W. M. Whelan, and S. L. Jacques, "Optical properties of biological tissues : a review Corrigendum : Optical properties of biological tissues :," 2013.

[191] J. L. Sandell and T. C. Zhu, "A review of in-vivo optical properties of human tissues and its impact on PDT," *Journal of Biophotonics*, vol. 4, no. 11-12, pp. 773–787, 2011.

[192] T. Lister, P. A. Wright, P. H. Chappell, T. Lister, P. A. Wright, and P. H. Chappell, "Optical properties of human skin," 2019.

[193] S. Groeger and J. Meyle, "Oral mucosal epithelial cells," *Frontiers in Immunology*, vol. 10, no. FEB, pp. 1–22, 2019.

[194] S. Prestin, S. Rothschild, C. S. Betz, and M. Kraft, "Measurement of epithelial thickness within the oral cavity using optical coherence tomography," *Head and Neck*, vol. 34, pp. 1777–1781, 2012.

[195] G. Peterson, D. K. Zanoni, M. Ardigo, J. C. Migliacci, S. G. Patel, and M. Rajadhyaksha, "Feasibility of a Video-Mosaicking Approach to Extend the Field-of-View For Reflectance Confocal Microscopy in the Oral Cavity In Vivo," *Lasers in Surgery and Medicine*, vol. 51, no. 5, pp. 439–451, 2019.

[196] F. Zernike, "Phase contrast, a new method for the microscopic observation of transparent objects," *Physica*, vol. 9, no. 7, pp. 686–698, 1942.

[197] ——, "How I discovered phase contrast," *Science*, vol. 121, no. 3141, pp. 345–349, 1955.

[198] S. B. Mehta and C. J. R. Sheppard, "Quantitative phase-gradient imaging at high resolution with asymmetric illumination-based differential phase contrast," *Optics Letters*, vol. 34, no. 13, p. 1924, 2009. [Online]. Available: https://www.osapublishing.org/abstract.cfm?URI=ol-34-13-1924

[199] R. K. Singh, A. M. Sharma, and B. Das, "Quantitative phase-contrast imaging through a scattering media," *Optics Letters*, vol. 39, no. 17, p. 5054, 2014. [Online]. Available:

https://www.osapublishing.org/abstract.cfm?URI=ol-39-17-5054

[200] Y. K. Park, C. Depeursinge, and G. Popescu, "Quantitative phase imaging in biomedicine," *Nature Photonics*, vol. 12, no. 10, pp. 578–589, 2018. [Online]. Available: http://dx.doi.org/10.1038/s41566-018-0253-x

[201] S. Xiao, S. Zheng, and J. Mertz, "High-speed multifocus phase imaging in thick tissue," *Biomedical Optics Express*, vol. 12, no. 9, p. 5782, 2021.

[202] C. J. Sheppard and A. Choudhury, "Image formation in the scanning microscope," *Optica Acta*, vol. 24, no. 10, pp. 1051–1073, 1977.

[203] J. W. Goodman, *Introduction to Fourier Optics*. Roberts & Co., 2005.

[204] G. J. Tearney, R. H. Webb, and B. E. Bouma, "Spectrally encoded confocal microscopy," *Optics Letters*, vol. 23, no. 15, pp. 1152–1154, 1998.

[205] I. Saknite, Z. Zhao, J. R. Patrinely, M. Byrne, M. Jagasia, and E. R. Tkaczyk, "Individual cell motion in healthy human skin microvasculature by reflectance confocal video microscopy," *Microcirculation*, vol. 27, no. 6, pp. 1–11, 2020.

[206] B. Larson, S. Abeytunge, and M. Rajadhyaksha, "Performance of full-pupil line-scanning reflectance confocal microscopy in human skin and oral mucosa in vivo," *Biomedical Optics Express*, vol. 2, no. 7, p. 2055, 2011. [Online]. Available: https://www.osapublishing.org/abstract.cfm?URI=boe-2-7-2055

[207] A. Zeidan and D. Yelin, "Reflectance confocal microscopy of red blood cells : simulation and experiment," vol. 6, no. 11, pp. 946–952, 2015.

[208] M. A. Altintas, M. Meyer-Marcotty, A. A. Altintas, M. Guggenheim, A. Gohritz, M. C. Aust, and P. M. Vogt, "In vivo reflectance-mode confocal microscopy provides insights in human skin microcirculation and histomorphology," *Computerized Medical Imaging and Graphics*, vol. 33, no. 7, pp. 532–536, 2009.

[209] L. Huang, G. N. McKay, and N. J. Durr, "A Deep Learning Bidirectional Temporal Tracking Algorithm for Automated Blood Cell Counting from Non-invasive Capillaroscopy Videos," *Medical Image Computing and Computer Assisted Intervention – MICCAI 2021*, pp. 415–424, 2021.

[210] F. Mahmood, R. Chen, and N. J. Durr, "Unsupervised Reverse Domain Adaptation for Synthetic Medical Images via Adversarial Training," *IEEE Transactions on Medical Imaging*, vol. 37, no. 12, pp. 2572–2581, 2018.

[211] H. C. Shin, H. R. Roth, M. Gao, L. Lu, Z. Xu, I. Nogues, J. Yao, D. Mollura, and R. M. Summers, "Deep Convolutional Neural Networks for Computer-Aided Detection: CNN Architectures, Dataset Characteristics and Transfer Learning," *IEEE Transactions on Medical Imaging*, vol. 35, no. 5, pp. 1285–1298, 2016.

[212] J. Steinman, M. M. Koletar, B. Stefanovic, and J. G. Sled, "3D morphological analysis of the mouse cerebral vasculature: Comparison of in vivo and ex vivo methods," *PLoS ONE*, vol. 12, no. 10, pp. 1–17, 2017.

[213] T. Fukuda, E. Asou, K. Nogi, and K. Goto, "Evaluation of mouse red blood cell and platelet counting with an automated hematology analyzer," *Journal of Veterinary Medical Science*, vol. 79, no. 10, pp. 1707–1711, 2017.

[214] J. Mestas and C. C. W. Hughes, "Of Mice and Not Men: Differences between Mouse and Human Immunology," *The Journal of Immunology*, vol. 172, no. 5, pp. 2731–2738, 2004.

[215] G. C. Beck, N. Akgün, A. Rück, and R. Steiner, "Design and characterisation of a tissue phantom system for optical diagnostics," *Lasers in Medical Science*, vol. 13, no. 3, pp. 160–171, 1998.

[216] R. Bays, G. Wagnières, D. Robert, J. F. Theumann, A. Vitkin, J. F. Savary, P. Monnier, and H. Van Den Bergh, "Three-dimensional optical phantom and its application in photodynamic therapy," *Lasers in Surgery and Medicine*, vol. 21, no. 3, pp. 227–234, 1997.

[217] B. W. Pogue and M. S. Patterson, "Review of tissue simulating phantoms for optical spectroscopy, imaging and dosimetry," *Journal of Biomedical Optics*, vol. 11, no. 4, p. 041102, 2006.

[218] G. J. Greening, R. Istfan, L. M. Higgins, K. Balachandran, D. Roblyer, M. C. Pierce, and T. J. Muldoon, "Characterization of thin poly(dimethylsiloxane)-based tissue-simulating phantoms with tunable reduced scattering and absorption coefficients at visible and near-infrared wavelengths," *Journal of Biomedical Optics*, vol. 19, no. 11, p. 115002, 2014.

[219] S. S. Klykov, I. V. Fedosov, and V. V. Tuchin, "Cell trapping in a blood capillary phantom using laser tweezers," *Saratov Fall Meeting 2014: Optical Technologies in Biophysics and Medicine XVI; Laser Physics and Photonics XVI; and Computational Biophysics*, vol. 9448, no. March 2015, p. 94480A, 2015.

[220] H. J. Jawad, M. Sarimollaoglu, A. S. Biris, and V. P. Zharov, "Dynamic blood flow phantom with negative and positive photoacoustic contrasts," *Biomedical Optics Express*, vol. 9, no. 10, p. 4702, 2018.

[221] C. Chen, F. Klämpfl, C. Knipfer, M. Riemann, R. Kanawade, F. Stelzle, and M. Schmidt, "Preparation of a skin equivalent phantom with interior micron-scale vessel structures for optical imaging experiments," *Biomedical Optics Express*, vol. 5, no. 9, p. 3140, 2014.

[222] A. B. Parthasarathy, W. G. Shin, X. J. Zhang, and A. K. Dunn, "Laser speckle contrast imaging of flow in a microfluidic device," *Biomedical Applications of Light Scattering*, vol. 6446, no. February 2007, p. 644604, 2007.

[223] H.-J. Lee, N. M. Samiudin, T. G. Lee, I. Doh, and S.-W. Lee, "Retina phantom for the evaluation of optical coherence tomography angiography based on microfluidic channels," *Biomedical Optics Express*, vol. 10, no. 11, p. 5535, 2019.

[224] G. N. McKay, N. Mohan, and N. J. Durr, "Imaging human blood cells in vivo with oblique back-illumination capillaroscopy," *Biomedical Optics Express*, vol. 11, no. 5, pp. 2373–2382, 2020. [Online]. Available: http://arxiv.org/abs/2001.06284

[225] Microchem, "SU-8 3000 Permanent Epoxy Negative Photoresist," Tech. Rep., 2000.

[226] K. V. Patel, "Epidemiology of Anemia in Older Adults," *Seminars in Hematology*, vol. 45, no. 4, pp. 210–217, 2008.

[227] E. Beutler and J. Waalen, "The definition of anemia: What is the lower limit of normal of the blood hemoglobin concentration?" *Blood*, vol. 107, no. 5, pp. 1747–1750, 2006.

[228] J. McMurdy, G. Jay, S. Suner, and G. Crawford, "Photonics-based In Vivo total hemoglobin monitoring and clinical relevance," *Journal of Biophotonics*, vol. 2, no. 5, pp. 277–287, 2009.

[229] R. G. Mannino, D. R. Myers, E. A. Tyburski, C. Caruso, J. Boudreaux, T. Leong, G. D. Clifford, and W. A. Lam, "Smartphone app for non-invasive detection of anemia using only patient-sourced photos," *Nature Communications*, vol. 9, no. 4924, pp. 1–10, 2018. [Online]. Available: http://dx.doi.org/10.1038/s41467-018-07262-2

[230] D. C. Rees, T. N. Williams, and M. T. Gladwin, "Sickle-cell disease," *The Lancet*, vol. 376, no. 9757, pp. 2018–2031, 2010. [Online]. Available: http://dx.doi.org/10.1016/S0140-6736(10)61029-X

[231] X. Li, M. Dao, G. Lykotrafitis, and G. E. Karniadakis, "Biomechanics and biorheology of red blood cells in sickle cell anemia," *Journal of Biomechanics*, vol. 50, pp. 34–41, 2017.

[232] I. Odame, "Developing a Global Agenda for Sickle Cell Disease. Report of an International Symposium and Workshop in Cotonou, Republic of Benin," *American Journal of Preventive Medicine*, vol. 38, no. 4 SUPPL., pp. S571–S575, 2010. [Online]. Available: http://dx.doi.org/10.1016/j.amepre.2009.12.021

[233] A. Y. Segbena, A. Guindo, R. Buono, I. Kueviakoe, D. A. Diallo, G. Guernec, M. Yerima, P. Guindo, E. Lauressergues, A. Mondeilh, V. Picot, and V. Leroy, "Diagnostic accuracy in field conditions of the sickle SCAN® rapid test for sickle cell disease among children and adults in two West African settings: The DREPATEST study," *BMC Hematology*, vol. 18, no. 1, pp. 1–10, 2018.

[234] N. Lurie, J. Slater, P. McGovern, J. Ekstrum, L. Quam, and K. Margolis, "Mortality in Sickle Cell Disease," *New England Journal of Medicine*, vol. 329, no. 7, pp. 478–482, 1993. [Online]. Available: http://www.nejm.org/doi/abs/10.1056/NEJM199308123290707

[235] H. H. Lipowsky, N. U. Sheikh, and D. M. Katz, "Intravital Microscopy of Capillary Hemodynamics in Sickle Cell Disease," vol. 80, no. July, pp. 117–127, 1987.

[236] J. A. Baeker Bispo, P. S. Pinheiro, and E. K. Kobetz, "Epidemiology and etiology of leukemia and lymphoma," *Cold Spring Harbor Perspectives in Medicine*, vol. 10, no. 6, 2020.

[237] P. Porcu, L. D. Cripe, E. W. Ng, S. Bhatia, C. M. Danielson, A. Orazi, and L. J. McCarthy, "Hyperleukocytic leukemias and leukostasis: A review of pathophysiology, clinical presentation and management," *Leukemia and Lymphoma*, vol. 39, no. 1-2, pp. 1–18, 2000.

[238] I. Saknite, J. R. Patrinely, Z. Zhao, H. Chen, A. Beeghly-fadiel, T. K. Kim, M. Jagasia, M. Byrne, and E. R. Tkaczyk, "Association of Leukocyte Adhesion and Rolling in Skin With Patient Outcomes After Hematopoietic Cell Transplantation Using Noninvasive Reflectance Confocal Videomicroscopy," vol. 37204, pp. 1–9, 2022.

[239] A. Ploppa, V. Schmidt, A. Hientz, J. Reutershan, H. A. Haeberle, and B. Nohé, "Mechanisms of leukocyte distribution during sepsis: An experimental study on the interdependence of cell activation, shear stress and endothelial injury," *Critical Care*, vol. 14, no. 6, p. R201, 2010. [Online]. Available: http://ccforum.com/content/14/6/R201

[240] A. A. Justiz Vaillant and A. Faran, *Leukocyte Adhesion Deficiency*. Treasure Island, FL: StatPearls Publishing, 2022.

Curriculum Vitae # GREGORY N. MCKAY **APRIL, 2022**

104 S Washington St.
Baltimore, Maryland 21231 USA
(+1) 617.894.0059
gmckay1@jhu.edu

EDUCATION AND DEGREES

2017–Present Graduate student, Department of Biomedical Engineering
Johns Hopkins University

2015–Present Medical student, School of Medicine
Johns Hopkins University

2009–2014 Undergraduate student, Institude of Optics and Department of Chemistry University of Rochester

RESEARCH EXPERIENCE

Johns Hopkins University, Baltimore, MD
Department of Biomedical Engineering *(July 2017-Present)*
Graduate Student in the laboratory of Nicholas J. Durr

- Invented and developed oblique back-illumination capillaroscopy for *in vivo* human blood cell imaging. This novel microcsopy method enabled the clearest images blood cells in humans in their native environment to date. This work yielded two patents.
- Created tissue-realistic microfluidic phantoms for using photolithography techniques and optical property matching to human tissue. This new protocol yielded a tissue-realistic model of blood flow for establishing ground truth information to train deep learning-based algorithms for instance segmentation, classification, and tracking.
- Developed scattering oblique plane microscopy for *in vivo* human blood cell analysis. This microscope provided a novel, label-free method of distinguishing between white blood cells and blood plasma *in vivo* that can be used for improving non-invasive neutropenia screening with conventional capillaroscopy.
- Applied reverse-lens mobile phone capillaroscopy to enable nailfold blood cell imaging. This compact, low-cost, and portable microscope can be readily adapted to any mobile phone to enable the viewing of red blood cells and optical absorption gaps passing through human capillaries *in vivo*.
- Investigated holographic lens-free imaging system for urinalysis and urinary tract infection screening. Developed a new system of bedside urine screening that makes use of holography and flow cells to enable direct, in-line screening of human urine in an indwelling catheter. This technology enables real-time screening for urinary tract infection and other genitourinary pathology.
- Developed large dynamic range diffuser wavefront sensing and lens-free fundoscopy to enable low cost ophthalmic screening.
- Constructed a microscopy with ultraviolet surface excitation system for slide-free histology applied to Mohs surgery margin evaluation.

University of Rochester Medical Center, Rochester, MY *(May 2013 - July 2015)*
Post-baccalaureate Researcher in the laboratory of Harris A. Gelbard

- Developed a custom super-resolution (fPALM, STORM) microscope system for investigating HIV-associated neurocognitive disorder.

Massachusetts Institute of Technology Lincoln Laboratory *(May 2013 - September 2013)*
Engineering internship under the supervision of Gilberto Gonzalez

- Built and calibrated an optical test bed for free-space laser communication.

University of Rochester, Rochester, NY *(May 2012 - May 2013)*
Undergraduate researcher in the laboratory of Lewis Rothberg

- Developed Brewster angle straddle interferometry for high throughput molecular screening.

University of Rochester, Rochester, NY *(May 2011 - May 2012)*
Undergraduate researcher in the laboratory of Julie Bentley

- Developed novel gradient index glass types and tested using various interferometric techniques.

Rochester Precision Optics, Rochester, NY *(May 2010 - September 2010)*
Engineering internship under the supervision of Brian Bundschuh

- Worked in precision glass molding and metrology departments for fabrication and testing of small diameter aspheres.

TECHNIQUES AND SKILLS

Optical Instrumentation and Alignment

- Proficiency in custom microscope development
- Adept at optical system alignment
- Experience with holography and digital reconstruction

Computing and Software

- MATLAB programming for hardware control, image registration, and data analysis
- Python programming for computer vision and data analysis
- Experience with mathematical models of diffraction and digital holographic reconstruction
- Proficiency with CAD (Solidworks) and 3D printing software
- Proficiency with custom circuit development, hardware control, and microcontrollers
- Basic lens design and optimization (Zemax OpticStudio)
- Experience with Pytorch and deep learning models for computer vision applications

Molecular Techniques

Blood cell isolation; DNA/RNA/Protein extraction and purification; PCR; Western Blot; Centrifugation; Agarose Gel Electrophoresis/Imaging; Fluorescence Microscopy; Immunofluorescence Microscopy; Cell/tissue Culture; Cell Transfection; Antiseptic Technique

Other Skills

- Proficiency with 3D printing, laser cutting, and rapid prototyping
- Experience with photolithography and microfabrication techniques
- Experience with development of macro- and micro-fluidic models
- Human subjects research (author and investigator of 5 IRB-approved studies)
- Ethical use of vertebrate animals in research training

TEACHING EXPERIENCE

Johns Hopkins University, Center for Bioengineering Innovation & Design *(September 2020-December 2020)*
Teaching Assistant

- Graduate Student Instructor for an undergradute team investigating tissue flattening approaches for efficient slide scanning in microscopy with ultraviolet surface excitation system.

Johns Hopkins University, *(July 2018-Present)*
Undergraduate Student Mentor

- Throughout my Ph.D. I have provided one-on-one mentoring of four undergraduate students working in our lab on various projects.

Johns Hopkins University, Center for Talented Youth *(September 2019-January 2020)*
High School Student Mentor

- Provided mentorship to three high school students.

University of Rochester *(2010-2014)*
Teaching Assistant

- Teaching assistant for undergraduate courses CHM132, CHM173, CHM210, MTH281.

PUBLICATIONS

Scattering oblique plane microscopy for in- vivo blood cell imaging. **G. N. McKay**, R. C. Niemeier, C. Castro-González, N. J. Durr. *Biomed. Opt. Express* **12(5)**. 2575-2585 (2021).

A Deep Learning Bidirectional Temporal Tracking Algorithm for Automated Blood Cell Counting from Non-invasive Capillaroscopy Videos. L. Huang, **G. N. McKay**, and N. J. Durr, *MICCAI*. 415-424 (2021).

Imaging human blood cells in vivo with oblique back-illumination capillaroscopy. **G. N. McKay**, N. Mohan, and N. J. Durr, *Biomed. Opt. Express* **11(5)**. 2373-2382 (2020).

Visualization of blood cell contrast in nailfold capillaries with high-speed reverse lens mobile phone microscopy. **G. N. McKay**, N. Mohan, I. Butterworth, A. Bourquard, Sánchez-Ferro Á, C. Castro- González, N. J. Durr., *Biomed. Opt. Express* **30(11)**. 2268-2276 (2020).

Deep Adversarial Training for Multi-Organ Nuclei Segmentation in Histopathology Images. F. Mahmood, D. Borders, R. J. Chen, **G. N. McKay**, K. J. Salimian, A. Baras, N. J. Durr., *IEEE Trans Med Imaging.* **39(11)**. 3257-3267 (2020).

Diffuser-based computational imaging funduscope. Y. Li, **G. N. McKay**, L. Tian, and N. J. Durr, *Optics Express* **28(13)**. 19641-19654 (2020).

Large dynamic range autorefraction with a low-cost diffuser wavefront sensor. **G. N. McKay**, F. Mahmood, and N. J. Durr. *Biomed. Opt. Express* **10(4)**. 1718-1735 (2019).

A low-cost quantitative continuous measurement of movements in extremities of people with Parkinson's disease. **G. N. McKay**, T. P. Harrigan, J. R. Brasic. *MethodsX* **6**. 169-189 (2019).

CONFERENCE PRESENTATIONS

A model for generating paired complete blood count and oblique back-illumination capillaroscopy data in tissue-realistic microfluidic chambers. **G. N. McKay**, L. Huang, T. L. Bobrow, S. Kalyan, S. C. Hur, S. Lanzkron, L. H. Pecker, A. R. Moliterno, N. J. Durr. *SPIE Photonics West* (2022).

A portable, dual-channel oblique back-illumination capillaroscope for in vivo human blood cell imaging in hematology clinics. **G. N. McKay**, L. H. Pecker, A. R. Moliterno, S. Lanzkron, N. J. Durr. *SPIE Photonics West* (2022).

Towards real-time urinalysis with holographic lens free imaging. **G. N. McKay**, A. Oommen, C. Pacheco, S. C. Ray, R. Vidal, B. D. Haeffele, N. J. Durr. *SPIE Photonics West* (2022).

A high-resolution reverse lens design for cell-phone capillaroscopy blood analysis. M. M. Morakis, **G. N. McKay**, N. J. Durr. *SPIE Photonics West* (2022).

Imaging phase-function contrast with masked aperture scattering oblique plane microscopy. R. C. Niemeier, **G. N. McKay**, N. J. Durr. *SPIE Photonics West* (2022).

Sequential staining technique for acquiring paired images with H&E and microscopy with ultraviolet surface excitation (MUSE). R. C. Niemeier, **G. N. McKay**, M. T. Chen, N. Shankar, A. S. Baras, E. Ng, N. J. Durr. *SPIE Photonics West* (2022).

Optimizing white blood cell contrast in graded-field capillaroscopy using capillary tissue phantoms. **G. N. McKay**, T. L. Bobrow, S. Kalyan, S. C. Hur, N. J. Durr. *SPIE Photonics West* (2021).

Registering large caustic distortions for high dynamic range diffuser wavefront sensing. **G. N. McKay**, F. Mahmood, N. J. Durr. *SPIE Photonics West* (2019).

High-speed imaging of scattering particles flowing through turbid media with confocally aligned oblique plane illumination. **G. N. McKay**, A. Trick. N. J. Durr. *SPIE Photonics West* (2019).

Detection and segmentation of colorectal polyps with fully convolutional neural networks. **G. N. McKay**, T. Chen, F. Mahmood, N. J. Durr. *IEEE International Symposium on Biomedical Imaging* (2018).

Adversarial U-net with spectral normalization for histopathology image segmentation using synthetic data. F. Mahmood, R. Chen, D. Borders, **G. N. McKay**, K. Salimian, A. Baras, N. J. Durr. *SPIE Medical Imaging* (2019).

PATENTS AND INTELLECTUAL PROPERTY

- C17196: Lens free urine analysis system
- C16645: Compact capillaroscope for non-invasive blood analysis.
- C15858: Cell Counting Capillaroscope - in vivo blood cell imaging for non-invasive complete blood count.
- C15238: Computational Lightfield Ophthalmoscope.
- C14288: Correlation of Quantitative Measurement of Movements and Positron Emission Tomography.
- C15004: A Low-cost Quantitative Continuous Measurement of Movements in the Extremities of People with Parkinsons Disease.

Biographical sketch

Gregory N. McKay was born in Newton, Massachusetts. After completing his schoolwork at Medway High School in 2009, he attended the University of Rochester in Rochester, NY. Here he received a Bachelor of Science in Optics and a Bachelor of Arts in Chemistry in 2013 and 2014, respectively. During the following year he worked at the University of Rochester Medical Center developing super-resolution microscopy techniques and appling them to HIV-associated neurocognitive disorder. He entered the Medical Scientist Training Program at Johns Hopkins University in 2015, completing two years of medical school education before starting his PhD studies in the department of Biomedical Engineering. He has continued his study of optics and its application to medicine, working on numerous translational, computational biophotonic technologies including capillaroscopy applied to blood cell imaging, holography applied to urinalysis, wavefront sensing applied to ocular aberrometry, and microscopy with ultraviolet surface excitation applied to dermatopathology.